Distribution Agreement

In presenting this thesis or dissertation as a partial fulfillment of the requirements for an advanced degree from Emory University, I hereby grant to Emory University and its agents the non-exclusive license to archive, make accessible, and display my thesis or dissertation in whole or in part in all forms of media, now or hereafter known, including display on the world wide web. I understand that I may select some access restrictions as part of the online submission of this thesis or dissertation. I retain all ownership rights to the copyright of the thesis or dissertation. I also retain the right to use in future works (such as articles or books) all or part of this thesis or dissertation.

Signature:

Stefan Falkner	Date

Quantum Walks and the Renormalization Group

By

Stefan Falkner
Doctor of Philosophy

Physics

Stefan Boettcher
Advisor

Fereydoon Family
Committee Member

Michelangelo Grigni
Committee Member

H. George E. Hentschel
Committee Member

Eric Weeks
Committee Member

Accepted:

Lisa A. Tedesco, Ph.D.
Dean of the James T. Laney School of Graduate Studies

Date

Quantum Walks and the Renormalization Group

By

Stefan Falkner

Diplom-Physiker

Advisor: Stefan Boettcher, Ph.D.

An abstract of

a dissertation submitted to the Faculty of the

James T. Laney School of Graduate Studies of Emory University

in partial fulfillment of the requirements for the degree of

Doctor of Philosophy

in Physics

2014

Abstract

Like random walks, quantum walks are taking on a central role in both describing physical transport phenomena, and establishing a framework for quantum search algorithms. Unlike their classical counterpart, quantum walks present a model for universal quantum computation and can be used to simulate potentially any quantum system. Despite recent theoretical and experimental advancements, our understanding of quantum walks still lacks far behind that of random walks as they exhibit a much broader spectrum of behaviors awaiting categorization and context, even on simple lattices. Using analytic and numerical methods, we explore dynamical properties of quantum walks on self-similar networks. In particular, we study the longtime asymptotic spreading on networks without translational invariance. For one commonly studied quantum walk, we find a simple relationship between quantum and classical dynamics suggesting a deeper connection, yet to be understood. Furthermore, we show that the parameters of quantum walks affect its dynamical properties on these networks significantly. We also encounter a phenomenon called localization where parts of the dynamics never move far from the initial site. We contrast this behavior on regular lattices and a fractal.

Quantum Walks and the Renormalization Group

By

Stefan Falkner

Diplom-Physiker

Advisor: Stefan Boettcher, Ph.D.

A dissertation submitted to the Faculty of the

James T. Laney School of Graduate Studies of Emory University

in partial fulfillment of the requirements for the degree of

Doctor of Philosophy

in Physics

2014

Contents

List of Figures

List of Tables

1 Introduction

> Everything starts somewhere, although many physicists disagree.
>
> Terry Prachett, *Hogfather*

Quantum mechanics is arguably one of the most important and revolutionary theories developed in the twentieth century. Despite its unintuitive predictions, it has succeeded in describing phenomena that seemed classically paradox, impossible, or at best surprising. Today, quantum mechanics founds the basis for our understanding of many branches in science [28].

To study the behavior of quantum systems, it seems only natural to use a controllable quantum system to simulate it. Based on this idea, Manin in 1980 [47] and independently Feynman two years later [27] suggested the use of what we now consider quantum computers: devices that use the laws of quantum mechanics to carry out their operations. In contrast to classical computers where information is stored in sequences of zeros and ones, quantum mechanics allows for superpositions of states and simultaneous manipulations of them. This, together with quantum interference and entanglement, offers potential advantages over classical computers [42]

Among the first algorithms for a quantum computer were the Deutsch algorithm [20], and its generalization the Deutsch-Jozsa algorithm [21]. They provided an example for a problem a quantum computer can solve more efficiently than a classical computer. It also inspired the later proposed algorithms by Shor [65] and Grover [30] which started research in the area of quantum information and quantum computation. This interdisciplinary

topic resides on the intersection of quantum physics, computer science, mathematics and engineering. Studying these systems yielded new insights into the analysis of quantum algorithms and problems they are suitable to solve efficiently [3].

Quantum walk in their modern representation can be seen as generalization of their classical counterpart, random walks. While the dynamics are stochastic in the latter case, quantum walks obey unitarity, and exhibit exclusively quantum properties like interference, and entanglement. For example, quantum walks can exhibit localization, meaning that there is a finite probability to find the quantum walker close to the starting site at all times. This can only be seen in disordered random walks where the dynamics depend on the specific location the walker finds itself [33]. In quantum walks this can even occur in translation invariant scenarios [36, 37, 7, 72, 25].

As for random walks, there are two different formulations: discrete-time [3, 50, 2, 6] and continuous-time [26] quantum walks. Both have been studied extensively over the past decade [70], but the relationship between them is far less understood [16, 66, 15] compared to the situation for random walks [34]. In this thesis, we focus exclusively on discrete-time quantum walks.

Random walks are routinely used in many different fields. From modeling transport phenomena or foraging animals, to descriptions for the stock market, they are also at the core of randomized algorithms, e.g., Markov-Chain-Monte-Carlo methods [43] and stochastic local search algorithms like simulated annealing [40] or WalkSAT [63]. For quantum walks, the situation is similar. While the first publications were concerned with quantum transport [3] and quantum lattice gases [50], the range of application has expanded over time. With the proof that quantum walks can perform universal quantum computations [14, 46], and the recent interest in quantum simulations [8, 62], quantum walks have evolved beyond the framework of quantum (search) algorithms. Nonetheless, quantum search algorithms in the spirit of Grover's algorithm still remain one of the major application driving current research [17, 58, 1, 68].

But quantum walks are not only a theoretical tool to model systems and study their

properties. Several experimental realizations have successfully implemented quantum walks in various systems: waveguides [56, 48], photonics [61, 18], optical lattices [74], and trapped ions [49].

Despite the broad range of applications in various fields, the general understanding of the dynamics of quantum walks still lacks far behind that of random walks, as they exhibit a broader spectrum of behavior. Aside from analytic results on regular lattices [9, 29, 36, 25], the hypercube [51], and certain types of disorder in one dimension [41, 5, 4, 71], very little is known about general properties and their circumstances. Some exploration has been done numerically [1, 55, 44], but we have not understood the interplay of quantum interference and geometry to describe, let alone predict, quantum walks in general ways.

In this thesis, we address discrete time quantum walks on self-similar networks and explore their long-time properties starting from localized initial conditions. This approach, while being in the spirit of quantum transport phenomena, is likely to also shed light on algorithmic applications for quantum search algorithms. Our methods include direct numerical simulations, analytics and numerics using renormalization group methods, as well as some analytic calculations.

The thesis is structured as follows. In chapter 2, we introduce discrete time quantum walks. We show similarities and highlight key differences to random walks by studying both on the one dimensional line. After discussing the renormalization group for both, we study the asymptotic behavior on different networks in chapter 3 exploring some of parameters intrinsic to quantum walks. In the last part, chapter 4, we present an intuitive explanation for localization on translational invariant lattices and compare it to self-similar networks. In the conclusions, chapter 5, we summarize our finding again, and discuss possible future directions.

2 Discrete Time Walks and the Renormalization Group

> I think I can safely say that nobody understands quantum mechanics.
>
> Richard Feynman, *The Character of Physical Law*

Before we formally define discrete-time quantum walks, we will revisit the well-known discrete time random walk in section 2.1 to highlight the differences later in section 2.2. To gain familiarity with the methods of the renormalization group, we introduce the techniques used for random walks in section 2.3 on the one dimensional line. The last part of this chapter explores why these methods only partially transfer from the stochastic random walk to the unitary quantum walk, and offers a possible alternative trying to overcome the found hurdles.

2.1 Random Walks

Classical random walks represent important stochastic processes that have found many applications in various fields, most notably, as a model for transportation and as key concept for randomized algorithms. With the discrete time quantum walk in mind, we shall also focus on the discrete time random walk here. The differences between continuous and discrete time in the classical framework are well understood, and in most cases in the

long time limit irrelevant [60].

2.1.1 Time evolution

The random walk constitutes a *stochastic* motion of a walker hopping from one node of a given graph to a neighboring one. This means the paths individual walkers take from a given initial condition are random and not precisely predictable. Commonly, the process is described in terms of the probability $p_{m,t}$ of finding the walker at a site m after t time steps from known initial conditions, say the walker starts at m_0. The master equation [69] captures the evolution of these probabilities. In the most compact form it can be written

$$|p_{t+1}\rangle = \mathbf{W} \cdot |p_t\rangle \tag{2.1}$$

where $|p_t\rangle$ is the staggered vector with $p_{m,t}$ as its m^{th} component. The elements $W_{m,n}$ of the matrix $\mathbf{W}$ are the transition probabilities for the walker at node n to move to node m. The matrix is *stochastic*, i.e. its columns sum up to one ensuring conservation of probability. For an unbiased random walk, all $W_{m,n} = 1/r$ where r is the degree of each node[1]. With this choice every *direction* is equally likely, and the walk is called biased, if this does not hold.

It is noteworthy that, while any particular realization of a random walk is stochastic and random, the master equation is a deterministic equation for the *probabilities* at each site. These do not vary between different observed walks if the initial conditions are identical, and can be reconstructed from multiple independent walks.

To illustrate what the master equation describes, and as a precursor to the quantum walk, let us look at the unbiased random walk on the one dimensional line as an example. Figure 2.1 shows how we break down each time step into two parts: First, the walker tosses a coin, deciding where to go next. This splits the total probability into two equal

[1] To keep the notation simple, we assume that the networks is regular. While not necessary for either the random, nor the quantum walk, a constant degree is often chosen to keep the notation as simple as possible.

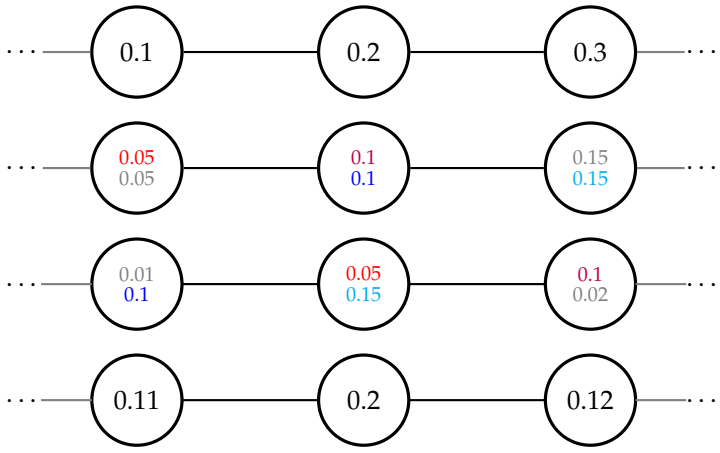

Figure 2.1: Three consecutive nodes of the one dimensional line. The top panel shows an example for the probabilities to find the walker at each node at a given time t. The coin toss of the walker can be seen as splitting these probabilities up into two equal parts, one for each direction (second panel). The hopping of the walker represented in the third panel corresponds to shifting the probabilities to the right (red) and left (blue). The gray entries originate from, or move to sites not shown. The sum of both components at every site equals the probability at time $t + 1$ (last panel).

components. In the second step, one component in shifted to the left, the other one to the right. The sum of the two components at each node yields the probability at the next time step. This may seem like a cumbersome description for the random walk, but it highlights the analogy to the quantum walk.

2.1.2 Asymptotic Properties

Random walks starting from a localized initial condition are known [34] to follow an asymptotic description of the probabilities for large time that reads

$$p_{m,t} \sim t^{-d_f/d_w} \cdot f\left(\frac{l_m}{t^{1/d_w}}\right) \tag{2.2}$$

where l_m equals the shortest distance between site m and m_0. The two parameters, d_f and d_w, are know as the fractal dimension of the underlying graph, and the walk dimension

characterizing the walk's dynamics. The static feature d_f provides information about the type of graph under consideration. To gain insights into the dynamical properties of the walk on that particular graph, usually d_w is the first starting point.

One common quantity often used to study the dynamics, in particular the spreading of the walk, is the mean-squared displacement

$$\sigma_t^2 = \sum_m p_{m,t} \cdot l_m^2 \,. \tag{2.3}$$

It is easy to show in the long time limit, when we can approximate $p_{m,t}$ by equation (2.2), what the scaling of σ_t^2 should be:

$$\begin{aligned}
\sigma_t^2 &\sim \sum_m l_m^2 t^{-d_f/d_w} \cdot f\left(\frac{l_m}{t^{1/d_w}}\right) \\
&\sim \sum_{l=0}^{\infty} l^{d_f-1} \cdot l^2 \cdot t^{-d_f/d_w} f\left(\frac{l}{t^{1/d_w}}\right) \\
&\approx t^{-d_f/d_w} \int_0^{\infty} l^{d_f+1} f\left(\frac{l}{t^{1/d_w}}\right) \mathrm{d}l \\
&\sim t^{2/d_w} \underbrace{\int_0^{\infty} x^{d_f+1} f(x)\, \mathrm{d}x}_{=\text{const.}}
\end{aligned} \tag{2.4}$$

Here we used the relation that the number of nodes a distance l away from any given site is proportional to l^{d_f-1} to convert the sum over all nodes into one over all possible distances. Please refer to [67] and the references with for a more detailed discussion of d_f. We then approximated the sum by an integral to find the third line. By a change of variables, we can isolate the explicit time dependence and rediscover this well-know scaling relation.

For unbiased random walks on hypercubic lattices, $d_w = 2$ regardless of the dimension d. This is called diffusive behavior, and any deviation from it is commonly referred to as anomalous diffusion. In this former case, the scaling function f in equation (2.2) can be found analytically: $f(x) = (4\pi)^{-d/2} \cdot \mathrm{e}^{x^2/4}$.

2.2 Quantum Walks

Discrete time quantum walks can be interpreted as a generalization of random walks. They follow a similar time evolution as described above, but the stochastic matrix $\mathbf{W}$ is replaced by the unitary time evolution operator $\mathbf{U}$ which now acts on the quantum state of the system. Probabilities have to be calculated from the state vector by computing appropriate inner products.

2.2.1 Time Evolution

To satisfy the unitarity requirement for quantum system the master equation (2.1) for the random walk is replaced by

$$|\psi_{t+1}\rangle = \mathbf{U} \cdot |\psi_t\rangle \,. \tag{2.5}$$

Here, $|\psi_t\rangle$ is the wave vector describing the quantum state of the whole system. It is again a staggered vector composed of the local wave vectors, $|\psi_{m,t}\rangle$, at each individual node. The probability of observing the walker at a particular site is defined by

$$p_{m,t} = \langle \psi_{m,t}| \, \psi_{m,t}\rangle \,. \tag{2.6}$$

This will prove to be a key difference when studying quantum walks on self-similar networks compared to random walks. For now, it only highlights the difference between the stochasticity of the random walk and unitarity here. The source of randomness in the former is the probabilistic coin toss itself, whereas in the quantum system, everything is deterministic until a measurement is performed.

The condition $\mathbf{U}^\dagger\mathbf{U} = \mathbb{1}$ is usually accompanied by the desire that $\mathbf{U}$ is local, meaning that each node's local state at time t only influences its neighbors states at $t+1$. This has immense implications on the structure of $\mathbf{U}$, and on the Hilbert space to which the local wave vectors belong. Following Meyer [50], let us investigate this in some detail on the one

dimensional line. For this case, equation (2.5) locally reads

$$|\psi_{m,t+1}\rangle = \mathbf{A} \cdot |\psi_{m-1,t}\rangle + \mathbf{B} \cdot |\psi_{m+1,t}\rangle \qquad \forall\ m \tag{2.7}$$

where $\mathbf{A}$ and $\mathbf{B}$ describe the transition $m \to m \pm 1$ for the local wave vectors $|\psi_{m,t}\rangle$. This system of equations only corresponds to a unitary time evolution, if

$$\mathbf{A}^\dagger\mathbf{A} + \mathbf{B}^\dagger\mathbf{B} = \mathbb{1} \qquad \text{and} \qquad \mathbf{A}^\dagger\mathbf{B} = \mathbf{B}^\dagger\mathbf{A} = 0\,. \tag{2.8}$$

These conditions can only be satisfied by scalars if one of them is zero, and the other one unimodular. While obeying all criteria, the time evolution in this case would be trivial: all $|\psi_{m,t}\rangle$ would be multiplied by a phase factor and then shifted to the left or right. There would be no *interaction* between wave functions on neighboring nodes.

There are two common ways to prevent this trivial behavior: First, introducing an internal degree of freedom at each site, often referred to as the coin state or chirality [58, 6]. This transforms $|\psi_{m,t}\rangle$ into a complex vector, and $\mathbf{A}$ and $\mathbf{B}$ into matrices which can satisfy condition (2.8) nontrivially. Generally, the minimum dimension of the internal degree of freedom has to match the degree of the node, but can be larger. The second option is to compose $\mathbf{U}$ out of (at least) two operators[2] acting on different local subsets of the networks sequentially. We will discuss the first method here in some detail, as we use it throughout the rest of the thesis. However, a discussion of the second approach and the relationship between both can be found in section 2.2.3.

The introduction of the coin space as an internal degree of freedom first appeared in the work of Aharonov *et al.* [2] and Ambainis *et al.* [6], and has been the canonical representation ever since [39, 70, 58]. The key concept is the parametrization of the time evolution operator in terms of a coin and a shift operator, called $\mathcal{C}$ and $\mathbf{S}$ respectively. Formally, the

[2]There is no reason to stop at two steps here.

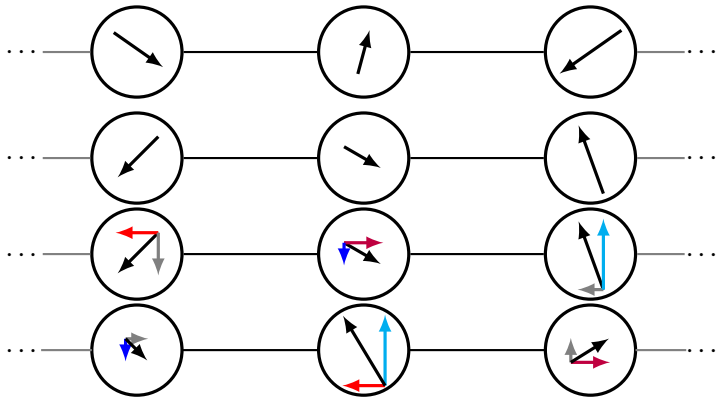

Figure 2.2: Three consecutive nodes of the one dimensional line. The top panel shows an example for the (here two dimensional) local wave vectors at each node at a given time t. The coin acts of them individually, illustrated by the same rotation (second panel). The shift operator translates different components of the vectors (decomposition illustrated in the third panel) to the neighboring sites (last panel). We obtain the wave vectors at time $t+1$ by simply combining all different components at each node. In the two last panels, the gray arrows highlight components that either go to, or originate from sites not shown in the image.

relationship is written as

$$\mathbf{U} = \mathbf{S} \cdot (\mathbb{1} \otimes \mathcal{C}) \ . \tag{2.9}$$

The coin acts on the coin state on each node in the same way. Subsequently, the shift operator exchanges components of all wave vectors between adjacent nodes. This mimics the random walk, where the walker tosses a *stochastic* coin and moves according to the outcome. Here the coin is unitary and the quantum walk evolves into a superposition of all possible directions.

In analogy to our discussion of one time step decomposed as a coin toss and a hop for the random walk, see figure 2.1, let us illustrate what this means for equation 2.5. In figure 2.2, we again present the one dimensional line as the simplest example, but the ideas generalize easily to more complicated networks.

The minimum dimension of any $|\psi_m, t\rangle$ equals the degree of node m. In our example, we represent the local wave vectors by black arrows. Note that we choose them to be

real for illustrative reasons, but in general they can be complex. To construct a unitary $\mathbf{U}$, the coin $\mathcal{C}$ has to be unitary as well. In figure 2.2, a rotation[3] of all arrows from the first to the second panel symbolizes that. Now the shift operator exchanges components between adjacent nodes in a consistent manner. In our example, the horizontal/vertical components are moved to the right/left. This has to be done consistently, usually realized by a permutation as the shift operator.

2.2.2 Asymptotic Properties

The long time behavior of quantum walks on regular lattices is well understood. Grimmett *et al.* [29] proved that almost every[4] coin leads to a scaling described by equation (2.2) with $d_w = 1$. In this context, the scaling function is called the weak limit, as there are rapid oscillations present in the true probability density function, whereas the limit is a smooth function. In some cases, the weak limit has been explicitly calculated [6, 35, 73, 25].

On networks without translational invariance, it is unknown whether the scaling relation (2.2) holds or not. Here, we postulate that it does. This assumption will be confirmed by our numerical simulations, but has no analytic underpinning at this point. A proof of this hypothesis requires a deeper understanding of the interplay between the network's geometry and the dynamics than we are able to achieve here.

2.2.3 Coinless Quantum Walks

The second approach to avoid a trivial evolution was first discussed implicitly by Meyer [50], more explicitly by Patel *et al.* [54], and later in more generality by Falk [24]. Di Franco *et al.* [22, 23] presented a hybrid approach where they reduce the internal dimension of the first approach by using ideas from the second one. In fact, both approaches can be unified into a very general framework discussed in section 2.2.3.

[3] A unitary matrix leaves the norm of a vector invariant. For real vectors rotations form one class of operations possessing this property. We use this as an example.

[4] They only make one assumption about the Fourier transformed time evolution operator (for details, see 4.16)): its eigenvalues cannot be equal. This case would correspond to a trivial motion of the wave vectors in one direction.

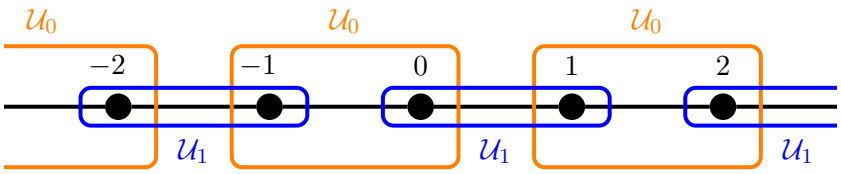

Figure 2.3: A possible realization for a coinless quantum walk on the one dimensional line. The blue and orange rectangles represent the two tessellations on which $\mathcal{U}_0$ and $\mathcal{U}_1$ are applied.

For these coinless quantum walks no internal degrees of freedom have to be introduces, i.e. the $|\psi_{m,t}\rangle$ are simply complex numbers. Similarly to the coined walk the time evolution operator is composed out of multiple local operators itself:

$$\mathcal{U} = \prod_i \mathcal{U}_i \,. \tag{2.10}$$

In the references [54, 22, 24], only two factors are considered, but in principle there is no limit to this number.

The idea is that each $\mathcal{U}_i$ acts on local sets of nodes, called patches or tessellation:

$$\mathcal{U}_i = \mathbf{P}_i^{-1} \cdot (\mathbb{1} \otimes \mathcal{C}_i) \cdot \mathbf{P}_i \tag{2.11}$$

We assume for simplicity that all patches contain the same number of nodes defining the dimension of $\mathcal{C}_i$. The dimension of the identity here corresponds to the number of patches. The permutation matrix P_i sorts the components of $|\psi_t\rangle$, such that the nodes of each patch are consecutive components of the vector $\mathbf{P}_i|\psi_t\rangle$. In other words, the P_i represent the tessellation. This formulation means that the same unitary operator $\mathcal{C}_i$ is applied on each patch independently. If these patches for different i overlap, there is the possibility for the wave function to spread across the whole system.

To illustrate this idea, consider the one dimensional line. Figure 2.3 shows the two possibilities how the one dimensional line can be split up in pairs of nodes. Now we just define two 2×2 matrices, $\mathcal{C}_0$ and $\mathcal{C}_1$, and we have constructed a coinless quantum walk that

only has a complex number associated to each node. This can, of course, be generalized to higher dimensional lattices, and essentially every graph.

But how does this relate to the alternative of introducing an internal degree of freedom and using a shift operator? Our naming already suggest that the local operator on the patches will correspond to the coin. If we reinterpret two nodes, say every even node together with the following odd one, as one node with two internal degrees of freedom, the operator $\mathcal{C}_1$ immediately corresponds to the coin. The special choice

$$\mathcal{C}_0 = \begin{bmatrix} 0 & 1 \\ 1 & 0 \end{bmatrix} \tag{2.12}$$

would facilitate the same effect the shift operator has. This means, if we combine the nodes of the blue patches and regard them as one node, we rediscover the formulation using a coin acting on an internal degree of freedom followed by a shift operator.

We have described this framework in all generality. Patel *et al.* [54] consider the special choice

$$\mathcal{C}_0 = \mathcal{C}_1 = \frac{1}{\sqrt{2}} \begin{bmatrix} 1 & \mathrm{i} \\ \mathrm{i} & 1 \end{bmatrix} \tag{2.13}$$

and show how this can reproduce the coined walk arguing similarly to the above explanation. Falk [24] on the other hand considers the two dimensional grid with patches of size 2×2 and chooses

$$\mathcal{C}_0 = \mathcal{C}_1 = \frac{1}{2} \begin{bmatrix} -1 & 1 & 1 & 1 \\ 1 & -1 & 1 & 1 \\ 1 & 1 & -1 & 1 \\ 1 & 1 & 1 & -1 \end{bmatrix}. \tag{2.14}$$

Our discussion for one dimension can be generalized to any graph, and whatever model is studied can be seen a special choice of the operators $\mathcal{U}_i$. For higher dimensional lattices or graphs with certain symmetries, it could be advantageous to compose the time evolution

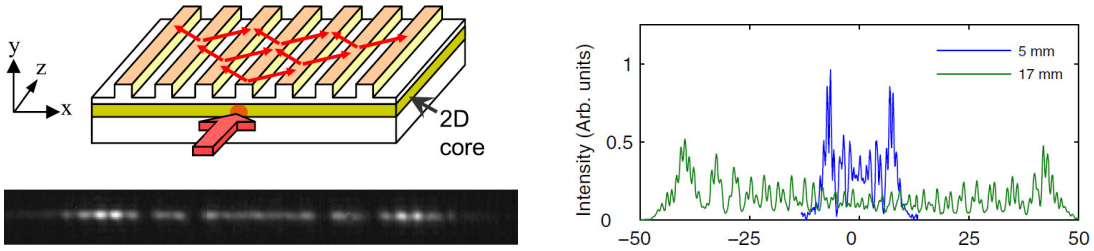

Figure 2.4: A schematic of the quantum walk implementation of a quantum walk using photons in waveguide lattices (top of left panel). Photons are injected into the thin layer where perform a quantum walk along the x direction with the z direction representing time. The intensity in each wave guide (bottom left panel) is proportional to the probablity distribution. The right panel shows a probability distribution reconstructed from such a measurement. Image taken from [56].

operator out of more than two $\mathcal{U}_i$. For the rest of the thesis, we will restrict ourselves to the coined model, as it naturally compares to the random walk with several parameters that affect the phenomenology qualitatively, as we will discover in chapter 3. Additionally, the choices of different tessellations adds more ambiguity[5] and complexity to the description.

2.2.4 Physical Implementations

The model of quantum walks described here might have merits on its own in the context of quantum algorithms and quantum information, but to be useful for quantum simulators, experimental setups implementing their time evolution are indispensable. In this section we mention two important advancements in this regard.

The first system (see figure 2.4) we want to acknowledge was implemented by Perets *et al.* [56] using a waveguide lattice. They created a waveguide structure that is periodic in x direction (representing the one dimensional lattice) and homogeneous in z direction taking on the role of time as the injected photons move along it. The structure allows the photons to tunnel between adjacent waveguides realizing the hopping in the lattice.

The right panel of figure 2.4 shows a measurement of the probability density at a given

[5]The number of possible tessellations quickly grows with the number of nodes in each patch, and so does the number of parameters of the most general unitary matrix. In turn, this also holds opportunities to find new behaviors for the very same reasons.

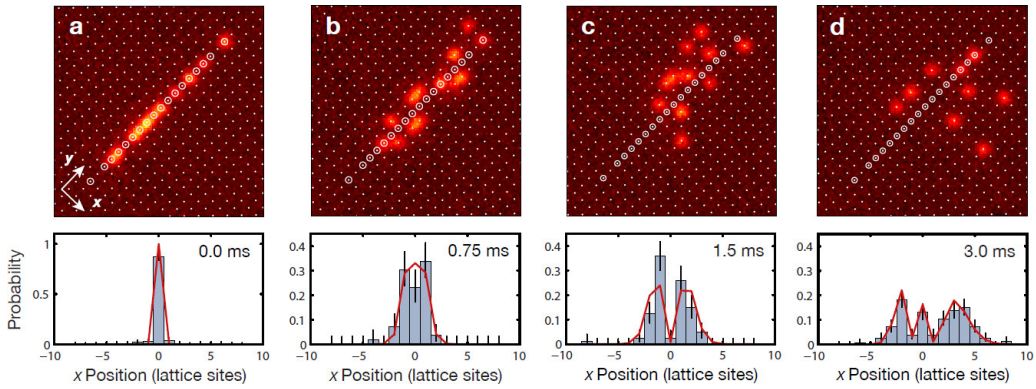

Figure 2.5: An illustration of the quantum walk implementation using ultra cold atoms in an optical lattice.(top row). The bright spots correspond to the actual position of the walker. The left image (a) shows the initial state where the spins of most of atoms along one line have been set up. The evolution in time can be seen in the panels (b) through (d). The bottom row depicts the probabilities for each displacement. Image taken from [74].

value for z. It clearly shows the different shape, with two peaks far out and strong oscillations, compared to the classical random walk, that would be a bell-shaped curve. Although this system corresponds to a continuous time quantum walk, the phenomenology on one dimensional line are equal to the discrete time version we study here. We mention this implementation as it was one of the first to implement a system with a significant number of sites ($\sim$ 100) simulating with almost no decoherence for long enough times to clearly see the ballistic spreading.

The second system, see figure 2.5, implements the quantum walk using ultra cold atoms in an optical lattice. Here, one spin degree of each atom acts as the coin state and can be individually addressed in the experiment. The interaction between neighboring lattice sites can be directly controlled enabling Weitenberg *et al.* to start and stop the walk at any given time. We can immediately see that the simulated system is much smaller than in the first implementation. This is due to the decoherence in the system and other experimental factors that render this approach more difficult than the waveguides. Nonetheless, the probability densities in the lower panels clearly deviates from those of a random walk.

From these two realizations, we can see the potential for future applications when the

experimental achievable system sizes and time intervals become large enough. Once truly quantum systems implementing quantum walks can be build, they can be used to experimentally investigate quantum systems in ways unimaginable with numerical simulations on classical computers.

2.2.5 Quantum Walks and Quantum Search Algorithms

The quantum walk we described is not a quantum search algorithm as we treat every node[6] the same. To turn it into a procedure that can be used to search, we only need to make a small modification [64]: The coin applied to the marked vertex, say $\mathcal{C}_1$, has to be different from the one applied to every other node, say $\mathcal{C}_0$ following the notation in [64]. A common choice is $\mathcal{C}_1 = -\mathbb{1}$, implementing a phase shift at the marked site rather than a mixing of the components. The application of a coin depending on certain properties of the item can be implemented without the exact knowledge of which item has this property. This is often called the oracle [58] and essential for this algorithm to work.

By marking a node with a special coin, the unitarity of the time evolution is preserved. As a consequence, the search algorithm does not converge to the solution for long times, but instead concentrates *close to* the special item periodically. To perform a successful measurement, one needs to wait a specific number of steps that depends on the system size. If this yields the correct node with a probability that does not tend to zero for larger and larger system sizes, this procedure successfully returns the right item eventually even for large databases.

Grovers original algorithm [30] requires a non-local time evolution, meaning that every node is connected to every other node. This assumption can be weakened, and quantum search algorithms on hypercubic-lattices are known to show the same speed up compared to their classical counterpart [64, 68, 58]. This is very important as the non-locality strongly limits the database size as decoherence tends to be stronger in physical realizations with

[6] In quantum search algorithms, every item is represented by a node in the graph. Finding an item means performing a measurement and observing the walker on a specified node.

many interactions.

2.3 The Renormalization Group for Random Walks

While there are several ways to approach the question of the long time asymptotic of the one dimensional line [34, 60], we revisit a recursive method know as the renormalization group [57]. By its nature, it lends itself to graphs/networks that can be defined recursively like fractals or other self-similar networks. Before we explore those in chapter 3, we first hone our skills by studying the one dimensional line, where the amount of algebra does not obscure the concepts of the method. We will extract the long time behavior of the random walk by studying the time evolution given by the master equation (2.1) under a rescaling of the typical length scale of the system. In other words; how much longer do I have to wait for a certain event, if the system is, say, twice as big?

In order to apply a decimation scheme, we first introduce the discrete Laplace transform[7] [38, 60, 69]

$$\tilde{p}_m(z) = \sum_{t=0}^{\infty} p_{m,t} z^t \qquad \text{and} \qquad p_{m,t} = \frac{1}{2\pi \mathrm{i}} \oint_{|z|=1} \tilde{p}_m(z) z^{-t-1} \, \mathrm{d}z \,. \tag{2.15}$$

The transformation is very similar to the Fourier transform in equation (4.2), but trades the discrete time for a complex parameter rather than space. While the Fourier transform greatly reduces the dimensionality of the master equation for translational invariant lattices, the Laplace transform turns equation (2.1) into an algebraic equation with explicit

[7] This concept is known under different names in different fields. Other names include the generating function, and the z-transform.

z dependence. To see that, multiply equation (2.1) by z^t and sum over all times

$$\begin{aligned}
\sum_{t=0}^{\infty} z^t \cdot |p_{t+1}\rangle &= \sum_{t=0}^{\infty} z^t \left(\mathbf{W} \cdot |p_t\rangle\right) \\
z^{-1} \sum_{t=1}^{\infty} z^t \cdot |p_t\rangle &= \mathbf{W} \cdot \left(\sum_{t=0}^{\infty} z^t \cdot |p_t\rangle\right) \\
|\tilde{p}(z)\rangle - |p_0\rangle &= z \cdot \mathbf{W} \cdot |\tilde{p}(z)\rangle \\
|\tilde{p}(z)\rangle &= z \cdot \mathbf{W} \cdot |\tilde{p}(z)\rangle + |p_0\rangle
\end{aligned} \tag{2.16}$$

This linear system still has the same dimensionality, but is no longer a difference equation in t. While the z dependence contains the complete information, one can use local knowledge around special points in the complex z plane to draw conclusion about the time dependence. For example, the point $z = 0$ contains the initial conditions, while the surroundings of $z = 1$ entail information about the limit $t \to \infty$ [38].

Let us consider the random walk on the one dimensional line starting at the origin at time $t = 0$. The master equation for every node m and its Laplace transform read

$$p_{m,t+1} = A \cdot p_{m-1,t} + B \cdot p_{m+1,t} + M \cdot p_{m,t} \tag{2.17}$$

$$\tilde{p}_m(z) = z \cdot A \cdot \tilde{p}_{m-1}(z) + z \cdot B \cdot \tilde{p}_{m+1}(z) + z \cdot M \cdot \tilde{p}_m(z) + \delta_{m,0} \tag{2.18}$$

where $A = B = 1/2$ and $M = 0$ represent the unbiased random walk. We can use the linear system for the sites surrounding site m, which we assume to be even:

$$\begin{aligned}
\tilde{p}_{m-1}(z) &= z \cdot A \cdot \tilde{p}_{m-2}(z) + z \cdot B \cdot \tilde{p}_m(z) + z \cdot M \cdot \tilde{p}_{m-1}(z) \\
\tilde{p}_{m+1}(z) &= z \cdot A \cdot \tilde{p}_m(z) + z \cdot B \cdot \tilde{p}_{m+2}(z) + z \cdot M \cdot \tilde{p}_{m+1}(z)
\end{aligned} \tag{2.19}$$

to find a solution for $\tilde{p}_{m\pm1}$ in terms of $\tilde{p}_m$ and $\tilde{p}_{m\pm2}$:

$$\begin{aligned}
\tilde{p}_{m-1}(z) &= (1 - z \cdot M)^{-1} \cdot (z \cdot A \cdot \tilde{p}_{m-2}(z) + z \cdot B \cdot \tilde{p}_m(z)) \\
\tilde{p}_{m+1}(z) &= (1 - z \cdot M)^{-1} \left(z \cdot A \cdot \tilde{p}_m(z) + z \cdot B \cdot \tilde{p}_{m+2}(z)\right)
\end{aligned} \tag{2.20}$$

Plugging this into equation (2.18) we find the equation

$$\tilde{p}_m(z) = A' \cdot \tilde{p}_{m-2}(z) + B' \cdot \tilde{p}_{m+2}(z) + M' \cdot \tilde{p}_m(z) + \delta_{m,0} \tag{2.21}$$

where the new, renormalized hopping parameters A', B' and M' are solely functions of the original parameters[8]:

$$\begin{aligned} A' &= A\,(1-M)^{-1}\,A & B' &= B\,(1-M)^{-1}\,B \\ M' &= M + A\,(1-M)^{-1}\,B + B\,(1-M)^{-1}\,A \end{aligned} \tag{2.22}$$

These equations are often referred to as the renormalization group flow, as they describe the evolution of the hopping parameters when coarse graining the system [57, 60]. In our case, we eliminated every odd node, cutting the system size in half. This can be repeated multiple times, leading to a description of bigger and bigger systems contained in the hopping parameters of a much smaller system.

As we are only interested in the unbiased case ($A = B = 1/2$ and $M = 0$ initially), we can parametrize the recursion equations with just two parameters: $A = B = a$ and $M = m$. We add a subscript k to emphasize the number of iterations already performed. For these two parameters, the recursions take the form

$$a_{k+1} = \frac{a_k^2}{1-m_k} \qquad \text{and} \qquad m_{k+1} = m_k + \frac{2a^2}{1-m_k} \tag{2.23}$$

with the initial conditions $a_0 = z/2$ and $m_0 = 0$.

The key concept now is that larger and larger systems are described by a_k and m_k for increasing k. A network with the hopping parameters parametrized by a_k and m_k actually contains the information of a system with 2^k as many nodes. If we interpret equation (2.23) as a dynamical system, this means that its fixed points describe the infinite system. For these equations, the only fixed point is $a_k = 0$ which describes the system without any

[8] Note that we absorbed the factors of z into the parameters A, B, and M compared to the ones in equation (2.18). We will have to take that into account by setting $A = B = z/2$ as the initial values.

hopping. But this does not mean the random walk is trapped. It is merely a consequence of the number of sites eliminated during the recursion step and the dynamics of the random walk. We have to study the system very close to this point. We do this by making the following ansatz[9]:

$$a_k = c_1^k \cdot \alpha_k \qquad \text{and} \qquad m_k = 1 - c_2^k \cdot \mu_k \tag{2.24}$$

Plugging this into equation (2.23) and solving for α_{k+1} and μ_{k+1} leads to consistent equations only for $c_1 = c_2 = 1/2$:

$$\alpha_{k+1} = \frac{2\alpha_k^2}{\mu_k} \qquad \text{and} \qquad \mu_{k+1} = 2\mu_k - \frac{4\alpha_k^2}{\mu}\,. \tag{2.25}$$

This system has only the fixed point $\alpha^* = \mu^*/2$. As discussed below, the Jacobian of the system in equation (2.25) and its eigenvalues contain all the information we need to determine the exponent d_w in equation (2.2). The Jacobian and its eigenvalues at this point read

$$\left.\frac{\partial\left(\alpha_{k+1}, \mu_{k+1}\right)}{\partial\left(\alpha_k, \mu_k\right)}\right|_{\alpha^*,\mu^*} = \begin{bmatrix} 2 & -\frac{1}{2} \\ -4 & 3 \end{bmatrix} \qquad \Longrightarrow \qquad \lambda = \{4, 1\}\,. \tag{2.26}$$

Together with the fact that the decimation removed half of the nodes, this yields the familiar result

$$d_w = \frac{\log(4)}{\log(2)} = 2\,. \tag{2.27}$$

This procedure needs some explanation as to why it works. We will only give a qualitative reasoning here, and a more rigorous derivation can be found in [60, 34]. The scaling assumption in equation (2.2) provides a relation between length and time scales in the argument of the scaling function f. By using the renormalization procedure as outlined above, we relate a change in length (iterating the recursion equations) to a change in time (distance to the fixed point).

[9] This particular choice was motivated by evolving the recursion equations numerically for a few steps and recognizing the exponential decay of a_k and $1 - m_k$.

Every iteration of the recursion equations decimates the system to half the size. In turn that means that the parameters α_k and μ_k entail the information of a larger system, 2^k times larger to be precise, compared to the numbers of nodes left. For the one dimensional line a typical length scale, say L_k, described by the hopping parameters doubles with every iteration, $L_{k+1} = 2L_k$, as every connection represents two connection in the previous iteration.

Whatever quantity we study, the approach $z \to 1$ contains information about the $t \to \infty$ limit as it includes more and more terms in equation (2.15) giving us access to the long time properties. In fact, there exists a so called Tauberian theorem stating that

$$\tilde{p}_m(z) \sim (1-z)^{-\rho} L\left(\frac{1}{1-z}\right) \quad (z \to 1^-) \qquad \Longleftrightarrow \qquad p_{m,t} \sim \frac{t^{\rho-1}}{\Gamma(\rho)} L(t) \quad (t \to \infty) \quad (2.28)$$

for some function $L(x)$ satisfying $L(\lambda x)/L(x) \to 1$ for $\lambda > 0$ and $x \to \infty$. This directly relates the behavior around $z = 1$ with the long time properties.

Close to $z = 1$ small difference in the initial condition of the parameters will grow with the number of iterations. Assuming that the growth of this difference happens close to an unstable fixed point, the change in $\varepsilon = 1 - z$ from one generation to the next can be directly linked to the change in a characteristic time scale [60]. In dynamical system, the growth of the difference is dominated by the larges eigenvalue of the Jacobian [67].

In the next section, we will try to generalize this method to the unitary quantum walk.

2.4 The Renormalization Group for Quantum Walks

Applying this decimation procedure to draw conclusions about the system based on the properties of recursion equations directly transfers to the quantum walk description. There are, though, some differences we explore in this section.

As we already hinted, the key difference between random and quantum walks is the meaning of the equations (2.1) and (2.5). In the former case it describes the probabilities

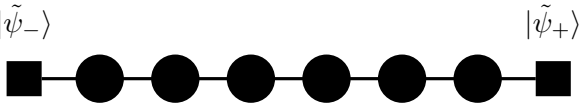

Figure 2.6: A finite line segment with absorbing boundaries (squares) on both sides.

directly, while we have to use equation (2.6) for the quantum walk to obtain them. This may sound like a technicality at first, but it has profound implications on our method. The relation between quantities in z space and their time dependent counterparts still holds, but in quantum mechanics the wave function itself has little meaning. Only observables, e.g. probabilities, are physical reality. This means we have to find a way to access properties of $\tilde{p}_m(z)$ given knowledge about $|\tilde{\psi}_m(z)\rangle$.

From general properties of the z-transform, it can be shown that

$$\begin{aligned}
\tilde{p}_m(z) &= \sum_{t=0}^{\infty} p_{m,t} \cdot z^t = \sum_{t=0}^{\infty} \langle \psi_{m,t}|\ \psi_{m,t}\rangle \cdot z^t \\
&= \sum_{t=0}^{\infty}\sum_{s=0}^{\infty} \langle \psi_{m,t}|\ \psi_{m,s}\rangle \cdot z^t \delta_{s,t} \\
&= \sum_{t=0}^{\infty}\sum_{s=0}^{\infty} \langle \psi_{m,t}|\ \psi_{m,s}\rangle \cdot z^t \left[\frac{1}{2\pi \mathrm{i}} \oint\limits_{|\nu|=1} \nu^{s-t-1}\,\mathrm{d}\nu\right] \\
&= \frac{1}{2\pi \mathrm{i}} \oint\limits_{|\nu|=1} \left[\sum_{t=0}^{\infty} \langle \psi_{m,t}| \cdot \left(\frac{z}{\nu}\right)^t\right] \cdot \left[\sum_{s=0}^{\infty} |\psi_{m,s}\rangle \cdot \nu^s\right] \frac{\mathrm{d}\nu}{\nu} \\
\tilde{p}_m(z) &= \frac{1}{2\pi \mathrm{i}} \oint\limits_{|\nu|=1} \left\langle \tilde{\psi}_m\left(\frac{z}{\nu}\right)\middle|\ \tilde{\psi}_m(\nu)\right\rangle \frac{\mathrm{d}\nu}{\nu}\,. \qquad (2.29)
\end{aligned}$$

The consequence is obvious: everything that can be learned from local properties, say around $z = 1$, in the classical case, is now encoded in an integral around the unit circle.

Let us focus on a very simple observable to explore the implications in more detail. Consider the one dimensional line with absorbing boundaries, where the quantum walk can enter, but not escape. A small system is depicted in figure 2.6. The observable we

want to study is the probability of ever getting absorbed at, say, the right end:

$$F_0 = \sum_{t=0}^{\infty} \langle \psi_{+,t} |\, \psi_{+,t} \rangle = \frac{1}{2\pi \mathrm{i}} \oint_{|z|=1} \left\langle \tilde{\psi}_+(1/z) \right| \left. \tilde{\psi}_+(z) \right\rangle \frac{\mathrm{d}z}{z} \,. \tag{2.30}$$

This kind of integrals is in general highly oscillatory for quantum walks, so there is little chance to calculate this quantity exactly[10]. But under certain circumstances, the integral could be dominated by a domain around a fixed point z^*, where a simple change of variables between generations preserves the structure of the integrand locally. This is, of course, not a necessity, but we shall see later in chapter 3 that it seems to be true for a particular coin on all networks we consider here. The substitution that allows reasoning similarly to section 2.3 would be $\varepsilon = z - z^* \to \lambda \cdot \varepsilon$ when going from one generation to the next.

Let us investigate the renormalization group for the one dimensional line. It is know that all coins lead to the same asymptotic scaling, so we can choose one without loss of generality. A common choice here is the so called Hadamard coin [6, 2]

$$\mathcal{C}_H = \frac{1}{\sqrt{2}} \begin{bmatrix} 1 & 1 \\ 1 & -1 \end{bmatrix} . \tag{2.31}$$

By choosing the particular parametrization

$$A = \begin{bmatrix} a & 0 \\ 0 & 0 \end{bmatrix} \cdot \mathcal{C}_H \qquad B = \begin{bmatrix} 0 & 0 \\ 0 & -a \end{bmatrix} \cdot \mathcal{C}_H \qquad M = \begin{bmatrix} b & 0 \\ 0 & b \end{bmatrix} \cdot \mathcal{C}_H \tag{2.32}$$

for the hopping parameters in equation 2.18, which are now two dimensional matrices, we find a closed set of recursion equations from the system in equation (2.22) for the complex

[10] To our knowledge, nobody has tried to calculate the absorption for the random walk this way either. This is because it is impractical to extract finite numbers like this from the renormalization group. Instead one usually studies the scaling of quantities as the system size changes.

parameters a and b:

$$a_{k+1} = \frac{a_k^2}{\sqrt{2}\left(1 - \sqrt{2}b_k + b_k^2\right)} \qquad b_{k+1} = b_k + \frac{a_k^2(\sqrt{2} - 2b_k)}{-2 + 2\sqrt{2}b_k - 2b_k^2} \tag{2.33}$$

Those equations are immediately more complicated than their random walk counterpart in equation (2.23), but we can still find all the fixed points and the corresponding eigenvalues of the Jacobian

$$\begin{aligned} (a^*, b^*) = (1,1)/\sqrt{2} \quad &\Longrightarrow \quad \lambda = \{2, 2\} \\ a^* = 0 \quad &\Longrightarrow \quad \lambda = \{0, 1\} \end{aligned} \tag{2.34}$$

One might think that the largest eigenvalue is still of relevance here, but as it turns out, this notion does not hold on the networks considered in chapter 3. Instead we can use a_k and b_k to calculate $|\tilde{\psi}_+^{(k)}(z)\rangle$ with 2^k sites between the two absorbing sites, starting adjacent to the left absorbing site. The numerical value for the absorption for this case in the infinite system size limit has been calculated by Bach *et al.* [9]. We do not want to calculate this number, but want to draw conclusions from its approach towards its limit.

The left panel in figure 2.7 shows the integrand that yields F_0 for different iterations/system sizes. We can identify that the first fixed point is part of a oscillatory regime. If we look in an neighborhood around it, we find that a rescaling with $\lambda = 2$ matches the integrand well for large enough system sizes in a finite region around $\theta = \arg(z) = 0$, shown in the right panel.

This type rescaling is at the heart of our renormalization approach for quantum walks. In the next chapter, we encounter cases where it works and we can use a numerical evolution of the recursion equations to confirm analytic values for d_w. But we also find coin operators that show no unstable fixed point and this approach simply does not apply. This highlights another difference between random and quantum walks. The stochastic nature of the former guaranties that there is a fixed point describing the infinite system size limit. For the unitary quantum walk, there is no guarantee that the recursions have a fixed point,

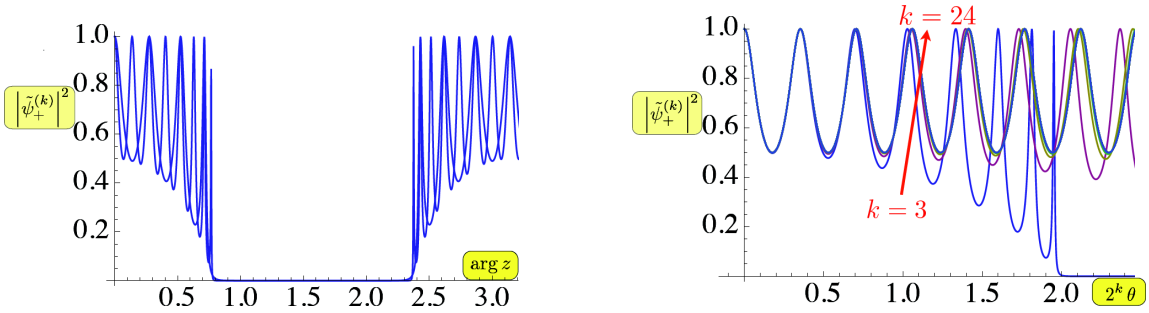

Figure 2.7: The integrand in equation (2.30) at different iterations k of the recursions of one dimensional line (left panel). There is an unstable fixed point for $\theta = \arg(z) = 0$. The rescaling that leaves the integrand locally invariant is shown in the right panel. Here, $\lambda = 2$ reproduces the known value $d_w^{QW} = 1$ as $L_{k+1} = 2L_k$ [13].

especially an unstable one.

3 Quantum walks on self-similar networks

> To understand recursion, you must first understand recursion.
>
> *Unknown*

For the regular lattices, the Fourier transform provides an indispensable tool for analytic insights for both random and quantum walk, and we use it in chapter 4 extensively. And while quantum walks offer a broader spectrum of possible behaviors , the asymptotic scaling remains the same for all of them, i.e. $d_w = 1$ [29]. The same is true for random walks where $d_w = 2$ holds for all unbiased variants.

Random walks have been successfully studied on a much broader variety of networks [59, 34, 60], including self-similar networks and fractals. We follow this path and study the asymptotics of quantum walks on them.

We begin by defining the networks considered here in section 3.1 where we first study the random walk to gain familiarity. Following in section 3.2, we introduce a numerical method to estimate d_w from direct simulations. We apply this and the renormalization group ideas from section 2.4 in 3.3 to explore the rich phenomenology of quantum walks on self-similar networks.

3.1 Self-similar networks

Self-similar networks are graphs where parts of it are similar/identical to the whole. This property lends them to recursive methods such as the renormalization group to study them.

Important examples are fractals and hierarchical networks.

The idea for all networks considered here is to apply simple substitution rules to a given graph to construct a new one. Following this *recipe to grow the network*, one finds a sequence of different networks, called generations, based on how often this iterative scheme has been applied. This procedure is intimately related to the renormalization group ideas we use to solve the random walk on them.

We will outline the calculations for one of the networks here in some detail. The methods directly apply to all of them, and all results are summarized in table 3.1.

The network we study in depth is based on work by Migdall and Kadanoff[11, 57], which we will refer to as MK3. The concept here is to replace every edge with a more complicated connection between the nodes introducing new ones. The specific recipe for this network, and the first two generations are depicted in figure 3.1. One important aspect when studying quantum walks is the type of edges adjacent to each node. Those are represented by different colors and letters in the figure. The different types of connections introduce a concept of *local directionality* meaning that the walker can distinguish between different *directions*. For the classical random walk with no memory, this distinction is not necessary, but it becomes indispensable for their quantum counterpart. To ensure self-similarity, the edge types for every node have to be preserved when iterating the recursive scheme. For MK3 this is achieved by conserving the type/color adjacent to node 1 and 2 in figure 3.1.

Before we can apply our method from section 2.3 to MK3, we need to calculate the fractal dimension. Here, we use the Hausdorf dimensions [59, 67] defined by

$$N \sim L^{d_f} \qquad (L \to \infty)\,. \tag{3.1}$$

The relation states that the number of nodes, N, within L steps from a (random) node scales like a power law with d_f as the exponent. This generalizes the concept of dimension to non-integer values while coinciding with the results for d-dimensional Euclidean spaces. To calculate the number, note that the number of edges satisfies, $E_{k+1} = 7E_k$, where k

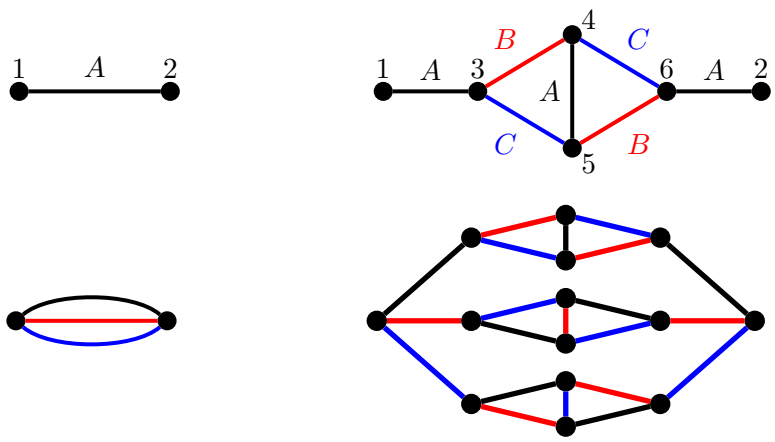

Figure 3.1: Illustration of the decimation procedure for the Migdal Kadanoff graph. For growing the network, each bond (top left) is replaced by a graphlet (top right). The colors encode the different hopping operators required for quantum walks. Note that edge type for node 1 and 2 do not change between generations. This ensures that the iterative scheme preserves the local hopping operators. The lower two panels show the first (left) and second (right) iteration.

is the generation. With the initial condition $E_0 = 3$, the solution is $E_k = 3 \cdot 7^k$. From this, we can find the number of sites: every edge is connected to two sites, but every node has degree 3. Therefore, $N_k = 2/3E_k = 2 \cdot 7^k$. By looking at the scheme in figure 3.1, we see that the distance between node 1 and 2 quadruples between iterations. This holds for any distances if we go from k to $k+1$, yielding $L_k \sim 4^k$. For large k, we hence find $d_f = \log(E_k)/\log(L_k) = \log_4(7)$.

To find the walk dimension, d_w, consider the top right graphlet in figure 3.1. For the

sites $3, \ldots, 6$, it represents the system of equations in Laplace space[1]

$$\begin{pmatrix} \tilde{p}_3 \\ \tilde{p}_4 \\ \tilde{p}_5 \\ \tilde{p}_6 \end{pmatrix} = \begin{bmatrix} A & 0 & M & B & C & 0 \\ 0 & 0 & B & M & A & C \\ 0 & 0 & C & A & M & B \\ 0 & A & 0 & C & B & R \end{bmatrix} \cdot \begin{pmatrix} \tilde{p}_1 \\ \tilde{p}_2 \\ \tilde{p}_3 \\ \tilde{p}_4 \\ \tilde{p}_5 \\ \tilde{p}_6 \end{pmatrix} \tag{3.2}$$

where M allows for self-interaction at each site. In the original graph $M = 0$. The system can be solved for $\tilde{p}_3, \ldots \tilde{p}_6$ in term of $\tilde{p}_1$ and $\tilde{p}_2$. Plugging the result into the equations for the remaining site amplitudes

$$\begin{aligned} \tilde{p}_1 &= M\tilde{p}_1 + A\tilde{p}_3 + B\tilde{p}_{\bar{3}} + C\tilde{p}_{\bar{\bar{3}}} \\ \tilde{p}_2 &= M\tilde{p}_2 + A\tilde{p}_6 + B\tilde{p}_{\bar{6}} + C\tilde{p}_{\bar{\bar{6}}} \end{aligned} \tag{3.3}$$

where the indices with bars on top represent the other neighbors of 1 and 2 analogous to 3 and 6 but connected by a different edge type. The equation for those are cyclic permutations ($A \to B \to C \to A$) of (3.2). Rearranging the terms, we find recursion equations relating the hopping parameters A, B, C, and M of the original system and the one with six seventh of the sides removed (the previous generation):

$$(A_{k+1}, B_{k+1}, C_{k+1}, M_{k+1}) = \mathcal{RG}\,(A_k, B_k, C_k, M_k) \tag{3.4}$$

Here k counts the number of decimation steps performed, i.e. effectively the system size. This is again the renormalization group flow [57, 60] containing all the information by representing different system sizes by different values of the hopping parameters. In the case of the unbiased random walk, all the hopping parameters are simple scalars which we

[1] For the random walk, the hopping parameters are all identical scalars, but the distinction becomes mandatory for the quantum walk. For clarity, we will treat the random walk more complicated than needed.

parametrize[2] by $A = B = C =: a$, and $M =: 1 - b$. We describe the random walk with these two parameters, a and b, for which the above outlined method produces the recursion equations

$$\begin{aligned} a_{k+1} &= \frac{2a_k^4}{b_k^3 - 4a_k^2 b_k - a_k b_k^2} \\ b_{k+1} &= b_k + \frac{3a_k^2(2a_k - b_k)(a_k + b_k)}{b_k^3 - 4a_k^2 b_k - a_k b_k^2} \end{aligned} \tag{3.5}$$

with the initial conditions $a_0 = z/3$ and $b_0 = 1$.

Again, the long time asymptotic is contained in the properties of a fixed point describing the infinite system. For this set of recursions, $a = 0$ is the only reachable fixed point for the specific initial conditions. As for the one dimensional example in section 2.3, this does not mean that nothing spreads, it is solely due to the fact that the decimation procedure outgrows the diffusion dynamics such that $M \to 1$. By studying the analogous system for $\alpha_k = 3^k a_k$ and $\beta_k = 3^k b_k$, we can investigate the system in this boundary layer, and find the line of fixed point $\beta_k = 3\alpha_k$. The Jacobian for this system at this point has the largest eigenvalue $\lambda = 21$. This eigenvalue directly relates to rescaling of z and hence t between iterations[60]. Together with the notion that distances quadruple between iterations, this results in $d_w^{RW} = \log_4(21)$.

This procedure can be directly applied to the following networks that follow different substitution rules. The second one we investigate, titled MK4, is in the very same spirit as MK3.The only difference is the inserted graphlet is four-regular, meaning that every node has exactly four neighbors. An illustration can be found in figure 3.2.

The third network is called Hanoi network (HN3) [12]. Here, from one generation to the next, new nodes are inserted along certain edges (A and B), and connections between pairs of the new nodes are established preserving the hierarchical structure. Other edges types (C and D) are not affected by the procedure. A peculiarity for HN3 is the fourth kind of connection, D, that is not part of the network itself, but emerges necessarily when

[2]The ansatz already anticipates that $M \to 1$ and parametrizes the difference to one. This simplifies the following recursions, and was purely chosen for convenience.

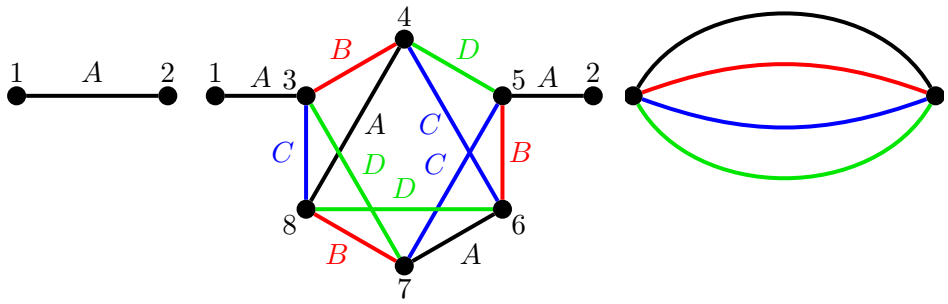

Figure 3.2: The decimation scheme for MK4. Every edge (left panel) at a certain generation is replaced by a graphlet of 6 nodes and 13 edges (middle panel). The corresponding graphs for the three other edge types can be found be cyclic permutation $A \to B \to C \to D \to A$. The right panel shows the zeroth generation.

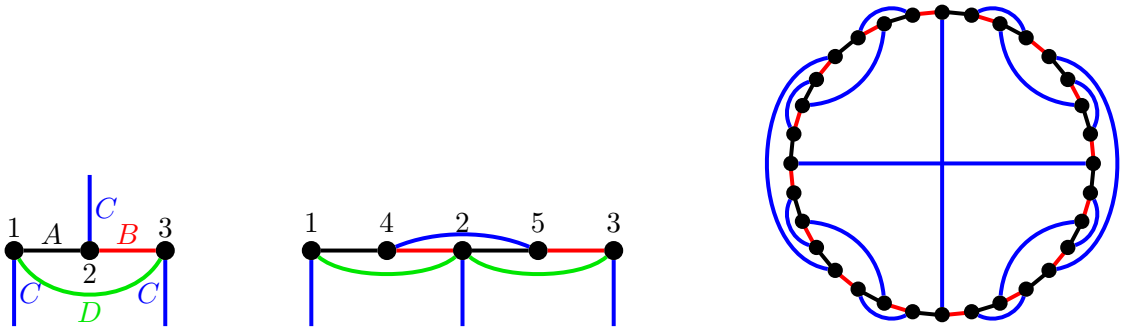

Figure 3.3: Illustration of the decimation procedure for HN3. The network is grown by inserting new nodes between an even and odd index and the appropriate connections(left to middle panel). Note that D is not present in the original graph, but emerges in order to close the renormalization group equations. The right panel shows the network of generation four with 32 nodes.

we reverse the recursive scheme to find the renormalization group flow.

The last network is the well-known Dual Sierpinski Gasket (DSG) [32, 34] depicted in figure 3.4. Here the self-similarity of the different edges between nodes proves to be harder to satisfy. We solve this problem by introducing asymmetric hopping along the connections. For those without an arrow (i.e. C in the figure) the hopping is symmetric between the connected nodes, meaning the hopping matrix C describes the transition from node 4 to 9, as well as the transition from 9 to 4. For the operators A and B, see figure 3.4, we choose to break this symmetry. For example B describes the transition from site 4 to 5 while 5 to

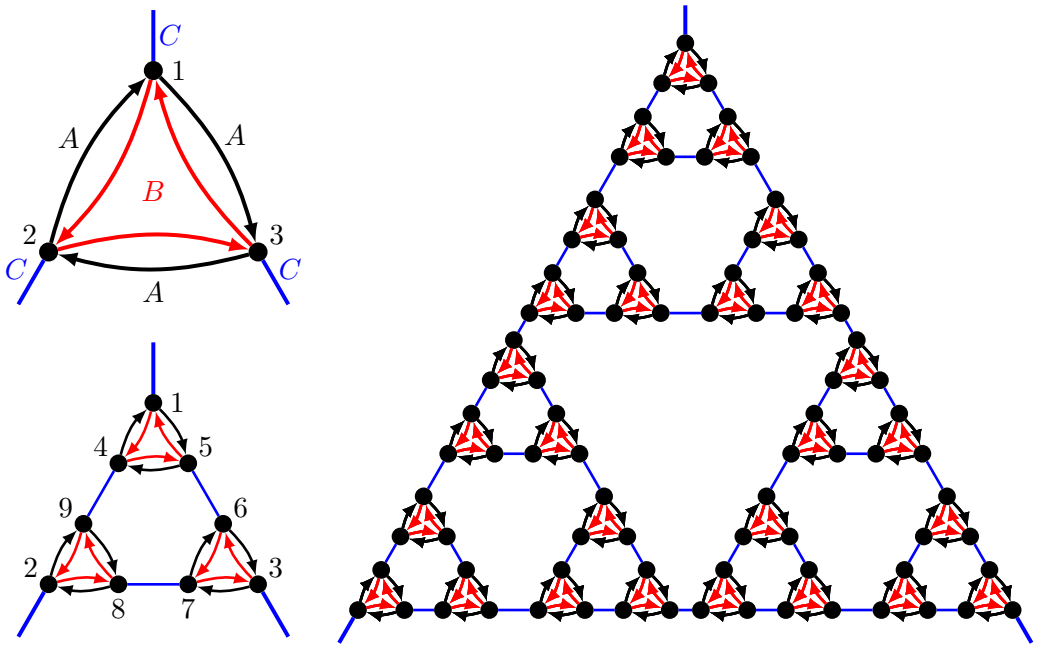

Figure 3.4: Illustration of the recursive scheme for the dual Sierpinsky gasket (DSG). To ensure self-similarity, we have to introduce asymmetric hopping operators (directed black and red edges) together with symmetric one (blue edges). The left panels show how the next generation is optained by inserting the nodes $4, \ldots, 9$ (bottom) into every triangle (top). The right panel depicts the network at the third generation.

4 is mediated by A. This allows us to consistently insert six new sites into every triangle to find the next generation.

By applying the procedure, outlined above for MK3, to the other three networks, the values for d_f and d_w for the unbiased random walk can be analytically obtained. The specific values can be found in table 3.1.

Table 3.1: Overview over the fractal and classical walk dimension for the networks.

Network	d_f	d_w^{RW}
MK3	$\log_4(7) \approx 1.404$	$\log_4(21) \approx 2.196$
MK4	$\log_4(13) \approx 1.850$	$\log_4(247/7) \approx 2.571$
HN3[12]	2	$\log_2\left(24 - 8\sqrt{5}\right) \approx 2.612$
DSG[32]	$\log_2(3) \approx 1.585$	$\log_2(5) \approx 2.322$

3.2 Direct numerical simulations

The numerical simulation of the quantum walk consists of iterating equation (2.5) on large system sizes for long times, and recording $p_{l,t}$ along the way. In this section we introduce a method to estimate d_w given the probabilities at different points in time.

The common method often found for numerical investigations [45, 58, 44] uses the second moment σ_t^2 as a function of time, and its scaling relation in equation (2.4), to fit a power-law to estimate d_w. While this undoubtedly works for small values of d_w, where everything spreads fast, and the random walk, where $p_{l,t}$ is smooth, there are some problems when applying this to quantum walks on self-similar networks. The main problem is caused by the interplay between localization and the oscillations found in the probability density function. Together they cause the second moment to be dominated by the behavior around the initial conditions. The spreading part just does not carry enough weight to be the dominant factor, at least not for numerically accessible system sizes and times. Therefore, we will use the scaling relation in (2.2) directly and try to collapse the whole probability density function for different times.

A scaling collapse like this is not uncommon in statistical physics in the context of finite size scaling [43]. Usually the scaling is limited to a small region around a critical point, and the analytic form of the scaling function is known. Here, we want to collapse over a large region without making any assumptions about the scaling function f, because, as we will see in the next section, it can vary drastically across networks.

Our method works in the following way. For a given estimate for d_w, we use a non-parametric fit [31] to estimate the scaling function. Based on this, we define an error of this collapse, we use the residual sum of squares (RSS). Starting from an initial guess, we apply the Nelder-Mead algorithm [52] to find an d_w that minimizes this error. The next paragraphs explain those steps in more detail.

The scaling in equation (2.2) can be rewritten as

$$p_{l,t} \cdot t^{d_f/d_w} \sim f\left(\frac{l}{t^{1/d_w}}\right) \tag{3.6}$$

which means that the quantity on the left hand side should be a universal function, with $l/t^{1/d_w}$ as the only argument. We know the fractal dimension d_f for our networks, and so d_w and f are the only parameters for collapsing the data. For our procedure, we first note that the points

$$(X_i, Y_i) := \left(l/t^{1/d_w}, p_{l,t} \cdot t^{d_f/d_w}\right) . \tag{3.7}$$

approximate f for the right value of d_w. A comparison between these points and a local estimation $\hat{f}$ based on them can be used to find a d_w which collapses the data well.

We use a non-parametric fitting [31] where the data is fitted locally by a degree 3 polynomial, which we call P_3. The locality of the fit is realized by weighing points with a kernel K. We decided to use the Gaussian kernel with zero mean and a variance $\sim N^{-1/5}$ where N is the number of data points. This is a very common choice and the default kernel in many software packages for nonparametric fitting. To deemphasize the large probabilities around the initial site, and to better fit the spreading part of the probability density function, we estimate not the probabilities themselves, but work with their logarithms. Formally, we define our estimate of the scaling function f to be

$$\hat{f}(x) = \underset{P_3}{\operatorname{argmin}} \sum_i K\left(x - X_i\right) \Big[\log(Y_i) - \log\Big(P_3(x - X_i)\Big)\Big]^2 , \tag{3.8}$$

Fitting the logarithm of f is ad hoc and has no analytic background. We merely postulate this, and the results will justify our choice later on.

The error of the collapse is then measured by

$$RSS(d_w) = \sum_i \Big[\log\left(Y_i\right) - \log\Big(\hat{f}(X_i)\Big)\Big]^2 , \tag{3.9}$$

which we minimize to find our estimate for d_w. Note that our procedure automatically puts more weight to larger times, as there are more points from later probabilities.

To estimate the error of our approach, we fit different subsets of the data, and use the statistical error of these estimates. While there are many ways to do this, we decided to introduce a lower cutoff to the fitting procedure as we cannot simulate enough different initial conditions (see below). It limits the range for which $\log(\hat{f})$ is estimated, and excludes points with probabilities too small. By decreasing the value, we expect to see the following behavior. Above a certain value, the cutoff excludes too many points resulting in a poor fit. Below a certain value, we expect our procedure to become inaccurate due to the finite simulated time. By examining quantum walks on all considered networks, we find the range $10^{-50} \ldots 10^{-10}$ to yield consistent results. This type of error analysis does not include any systematic error that could result from the finite simulations or the fitting method itself, a common problem for nonparametric fitting.

It is no surprise that we find best results for very long times. This restricts the number of initial conditions we can simulate as the system sizes are very large. Here, we generate networks with $\sim 10^7$ nodes and simulate up to $t = 8192 \ldots 65536$ (depending on the network) time steps. Compared to other recent simulations these are unprecedented combinations of system size and simulated time. For example, Lara *et al.* [44] performed simulations on the DSG with ~ 20000 nodes allowing them to average over many initial conditions. In another recent publication by Vieira *et al.* [71], quantum walks with $N \leq 2000$ were simulated for $t \leq 1000$ steps, averaging over ~ 20000 initial conditions. Counting the total number of multiplications, this equals any single run presented here in section 3.3. Similar system sizes ($\sim 7 \cdot 10^6$ nodes) have been simulated by Patel *et al.*[53], but they provide neither the longest simulated time for this system size, nor the number of initial conditions.

To validate that the value of d_w does not depend we run always at least two random initial conditions. While we show only the results of one of them, the values always agreed within our estimated error. This also serves as evidence that the scaling relation in equation (2.2) holds for quantum walks regardless of the specific initial state.

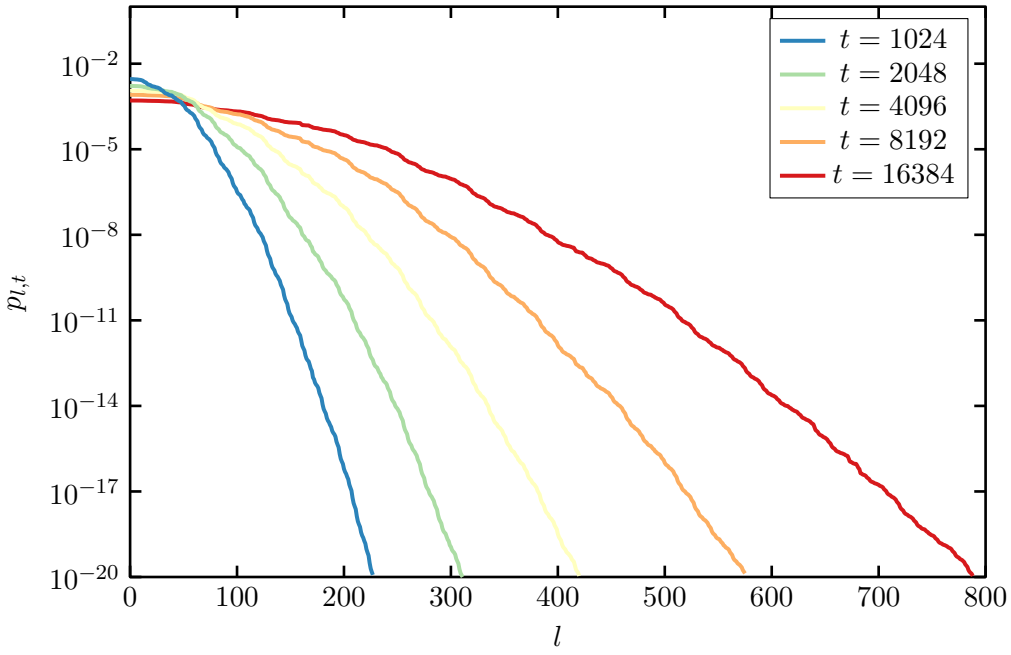

Figure 3.5: The probability $p_{l,t}$ of the random walk on MK3 at different times.

Let us illustrate the procedure for the random walk on MK3. In figure 3.5, we show probability density function at five different times. Again, our goal is to scale the x and y axis such that these curves collapse. In this case, we already know that $d_w = \log_4(21)$ is the asymptotically correct value.

The left panel in figure 3.6 shows the scaling of the very same probabilities for $d_w = 1$, which is obviously not correct, but it gives us an impression of $\hat{f}$. The right panel shows the best fit found by minimizing equation (3.9).

In figure 3.7, we investigate the robustness of our method. The left panel shows the estimated value of d_w a function of the lower cutoff. The range for the lower cutoff is small because for a larger d_w the simulations have to be much longer for the probability density function to spread as far. But we can see how our procedure becomes inaccurate for too small and too large values. For a specific cutoff of 10^{-15}, the right panel depicts the quadratic minimum of $RSS(d_w)$ around the estimated value.

In comparison, the figures 3.8, 3.9, and 3.10 show the same procedure for a quantum

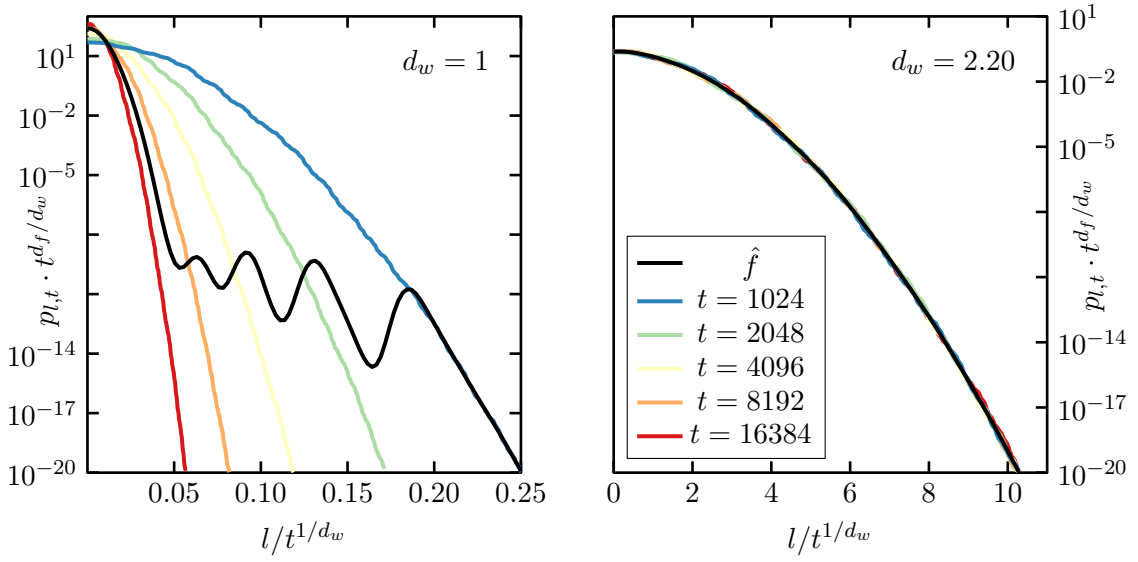

Figure 3.6: The scaled probabilities for $d_w = 1$ (left panel) as an illustration, and for the estimated value $d_w = 2.19(1)$. The error to $\log_4(21)$ is 0.3%.

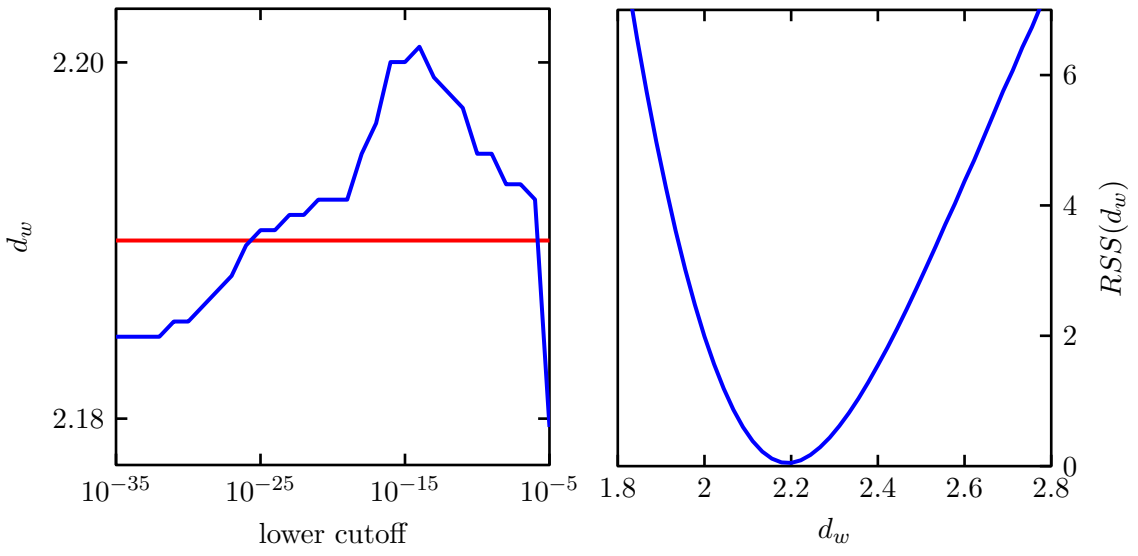

Figure 3.7: Dependency of the estimated value for d_w on the lower cutoff used for $\hat{f}$ (left panel), and the function $RSS(d_w)$ around the best value found to confirm a single minimum (right panel) for the unbiased random walk on MK3. The red line shows the estimated value only minutely below the exact value of $\log_4(21)$.

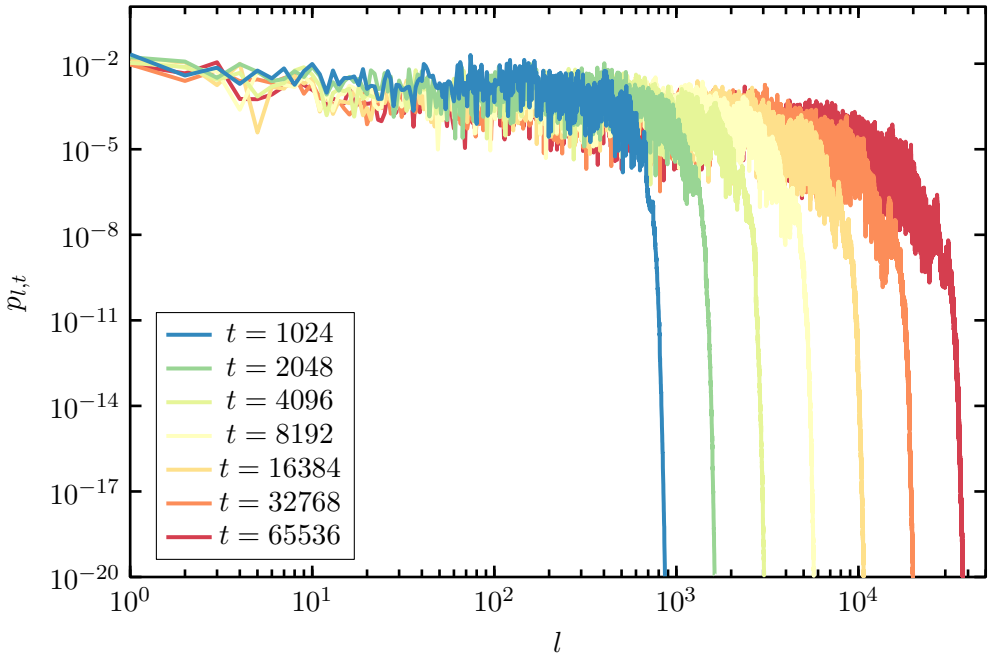

Figure 3.8: The probability $p_{l,t}$ of a quantum walk on MK3 using the Grover coin at different times. See the following section for details.

walk using the so called Grover coin (see section 3.3.1 for details). We can immediately see differences in the probability density function: the overall shape is different, and strong oscillations are visible. But our procedure for $\hat{f}$ works very well in smoothing these rough data sets, and the found value for d_w in the right panel of figure 3.9 collapses the data over the whole shown range. For this case, the simulated time was long enough such that the lower cutoff has almost no influence once it is small enough. The minimum of $RSS(d_w)$ is more pronounced compared to the random walk.

3.3 Exploring different coins

In this section, we use the methods described earlier to determine the value of d_w^{QW} for different coins. We focus on two important and well-known coins: the Grover and the Fourier coin. The former is a highly symmetrical, real coin, while the second one originates from discrete Fourier transforms and is sometimes studied [58]. As a third example, we

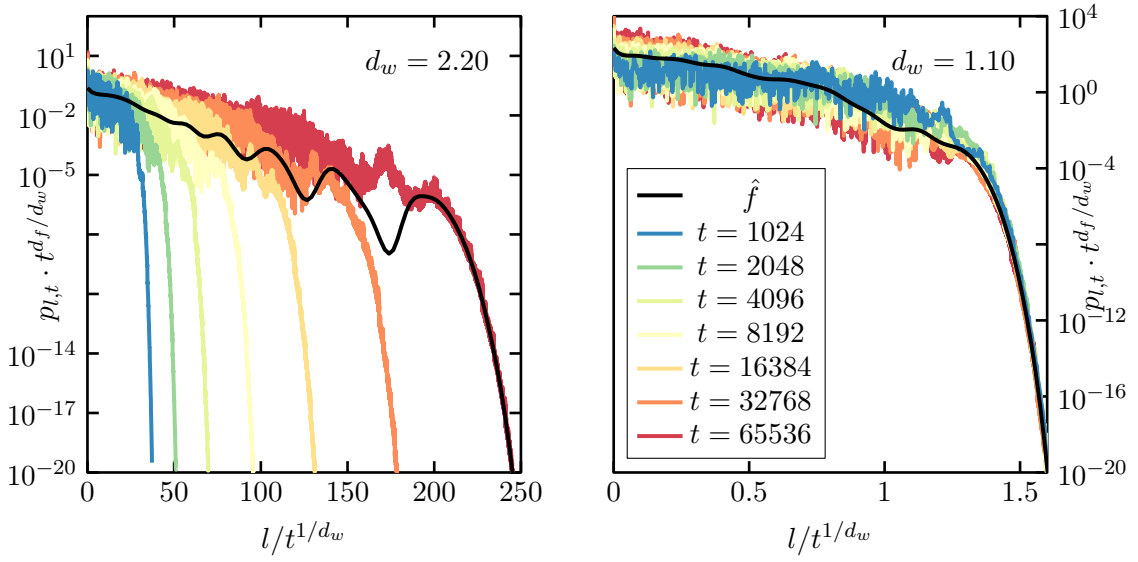

Figure 3.9: The scaled probabilities for the classical value $d_w = 2.20$ (left panel) and the estimated optimal value $d_w = 1.10$ for the quantum walk using the Grover coin on MK3.

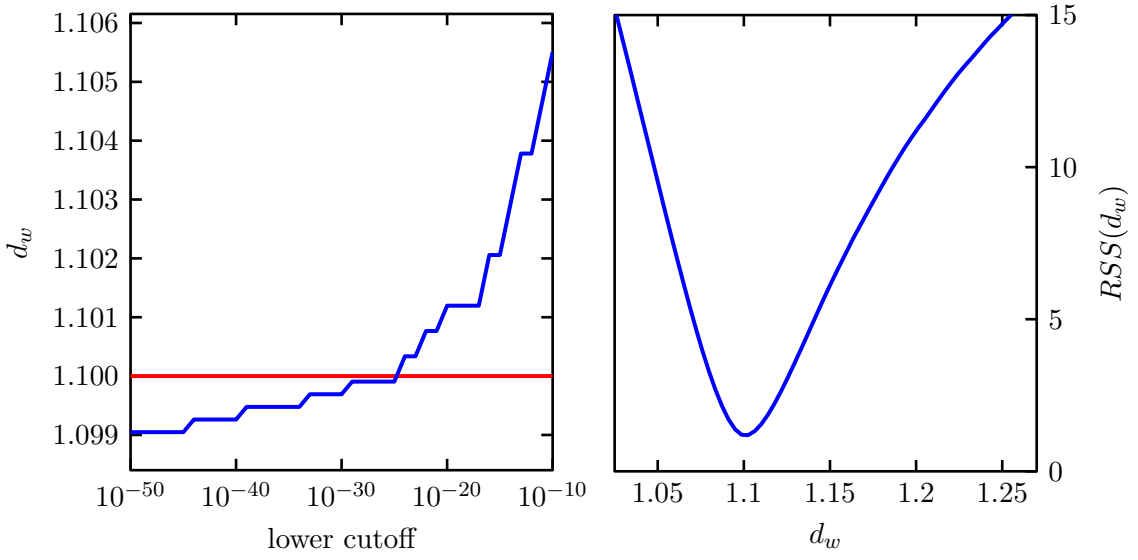

Figure 3.10: Dependency of the estimated value for d_w on the lower cutoff used for $\hat{f}$ (left panel), and the function $RSS(d_w)$ around the best value found to confirm a single minimum (right panel) for a quantum walk on MK3. The red line shows the estimated value.

will look at an orthogonal coin that looks very similar to the Grover coin, but exhibits different behaviors.

3.3.1 The Grover Coin

The Grover coin has taken on a very important role in quantum walks. Inspired by Grover's original work [30], this coin can be defined in all dimensions of the coin space. Only for the two dimensions case does it not lead to interesting behavior as the quantum walker either stays completely localized or moves deterministically into a certain direction.

The general definition of the Grover coin can be written as

$$\mathcal{C}_G = 2\,\frac{|\mathbb{1}\rangle\langle\mathbb{1}|}{\langle\mathbb{1}|\,\mathbb{1}\rangle} - \mathbb{1}\,. \tag{3.10}$$

Here $|\mathbb{1}\rangle$ is the vector with all entries equal to one, and $\mathbb{1}$ being the identity matrix, both with the same dimension as the coin space. On the networks here, the three and four dimensional cases read

$$\mathcal{C}_G = \frac{1}{3}\begin{bmatrix} -1 & 2 & 2 \\ 2 & -1 & 2 \\ 2 & 2 & -1 \end{bmatrix} \qquad \text{and} \qquad \mathcal{C}_G = \frac{1}{2}\begin{bmatrix} -1 & 1 & 1 & 1 \\ 1 & -1 & 1 & 1 \\ 1 & 1 & -1 & 1 \\ 1 & 1 & 1 & -1 \end{bmatrix}. \tag{3.11}$$

By definition, this coin is always hermitian and self inverse. In fact, it is the negative of a Hausholder reflection, a class of linear transformation well know from, e.g., QR decompositions.

Before using renormalization group to determine d_w, we apply the numerical method introduced in section 3.2 to gain insights into the behavior on the different networks. The raw probabilities and the scaling collapses are shown in figure 3.11, and the parameters and results of the simulations in table 3.2.

Note, regardless of the network the scaling function looks similar in all four cases. There

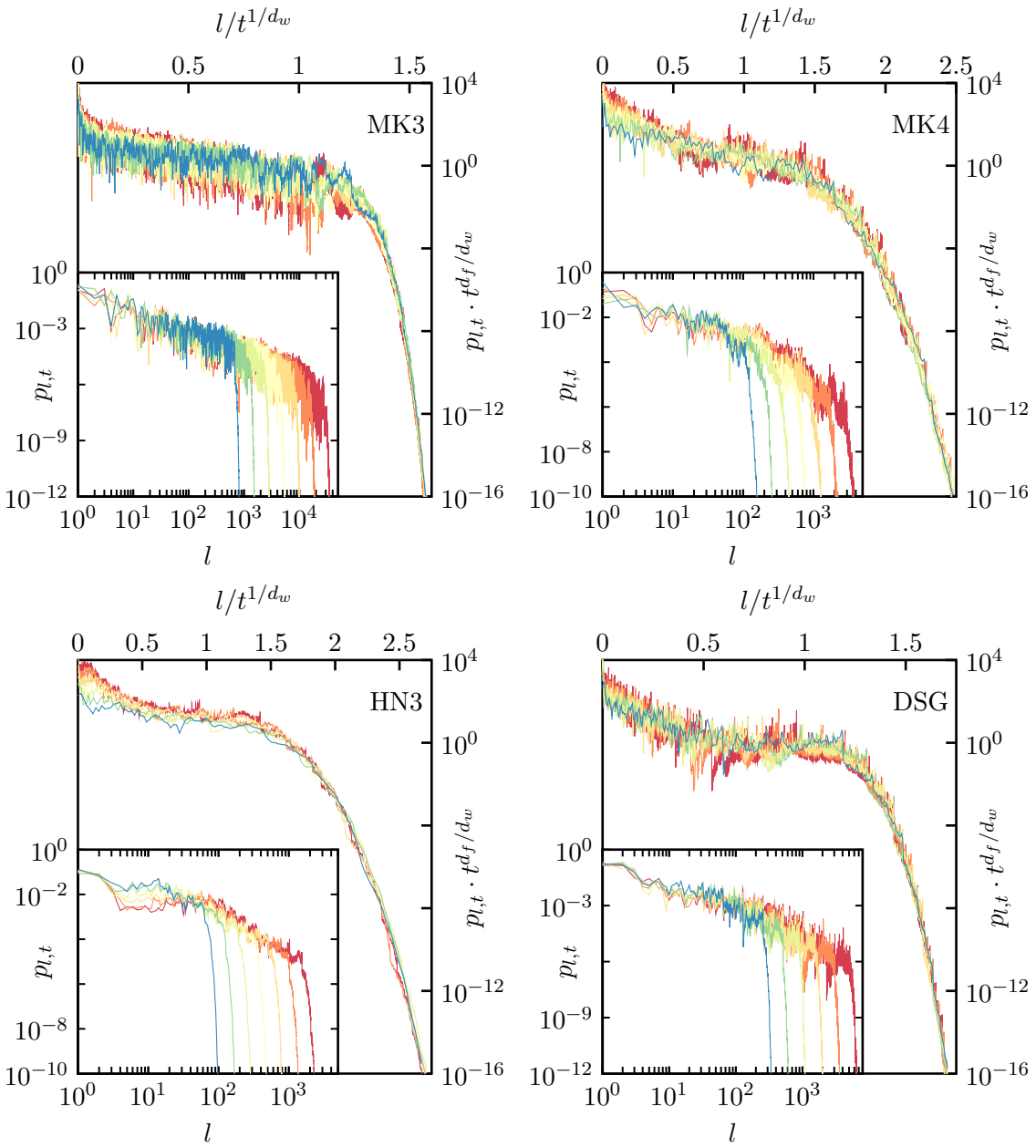

Figure 3.11: Direct simulation of the quantum walk using the Grover coin on all four networks. The insets show the raw PDFs, while the main panel shows the best fit. The parameters of all simulations and the estimated values for d_w can be found in table 3.2.

Table 3.2: Parameters for the simulation shown in figure 3.11 using the Grover coin. The networks with N nodes, and the maximum distance l_{max} from the initial condition where evolved for t_{max} time steps. The colors in the plots correspond to t_{min} (blue) in powers of 2 up to t_{max} (red). See text for discussion.

Network	N	l_{max}	t_{min}	t_{max}	d_w^{est}
MK3	$2 \cdot 7^8 \approx 1.2 \cdot 10^7$	2^{16}	2^{10}	2^{16}	1.100(4)
MK4	$2 \cdot 13^6 \approx 1.0 \cdot 10^7$	2^{12}	2^8	2^{14}	1.283(2)
HN3	$2^{24} \approx 1.7 \cdot 10^7$	2^{12}	2^7	2^{13}	1.299(5)
DSG	$2 \cdot 3^{14} \approx 1.0 \cdot 10^7$	2^{12}	2^8	2^{14}	1.161(1)

is a relatively high *peak* at $l/t^{1/d_w} = 0$ indicating that there could be localization, see chapter 4 for details. Then there is some intermediate range where f is almost constant, followed by an exponential cut-off[3]. We show the results in table 3.2 to three significant digits, which we determined by varying the cut-off for the non-parametric fitting. We want to point out, that all the numbers are very close to half the classical values for the random walk in table 3.1.

For three out of the four networks, we were able to simulate longer than the largest distance of the finite system. This introduces, in principle at least, boundary effects that could corrupt our results. We assure that the probabilities are not noticeably influenced. After all, $d_w > 1$ means that only an exponentially small fraction reaches further out than $l \sim t^{1/d_w}$. This enables us to simulate longer than the system size would allow for ballistic spreading. For MK3, d_w is too small to simulate substantially longer at the given system size.

Based on these findings, we will now use the method outlined in section 2.4 to determine the values for the walk dimension to almost arbitrary accuracy. To do that, we need to find an adequate set of renormalization parameters and derive the recursion equations. We begin with MK3, followed by MK4, HN3 and DSG.

The linear system corresponding to equation (3.2) we need to solve for the quantum

[3]Beware that the main panels of all plots are log-linear.

walk on MK3 reads

$$\begin{aligned}
|\tilde{\psi}_3\rangle &= \mathbf{A}|\tilde{\psi}_1\rangle + \mathbf{M}|\tilde{\psi}_3\rangle + \mathbf{B}|\tilde{\psi}_4\rangle + \mathbf{C}|\tilde{\psi}_5\rangle \\
|\tilde{\psi}_4\rangle &= \mathbf{B}|\tilde{\psi}_3\rangle + \mathbf{M}|\tilde{\psi}_4\rangle + \mathbf{A}|\tilde{\psi}_5\rangle + \mathbf{C}|\tilde{\psi}_6\rangle \\
|\tilde{\psi}_5\rangle &= \mathbf{C}|\tilde{\psi}_3\rangle + \mathbf{A}|\tilde{\psi}_4\rangle + \mathbf{M}|\tilde{\psi}_5\rangle + \mathbf{B}|\tilde{\psi}_6\rangle \\
|\tilde{\psi}_6\rangle &= \mathbf{A}|\tilde{\psi}_2\rangle + \mathbf{C}|\tilde{\psi}_4\rangle + \mathbf{B}|\tilde{\psi}_5\rangle + \mathbf{M}|\tilde{\psi}_6\rangle
\end{aligned} \tag{3.12}$$

Plugging the solution for $|\tilde{\psi}_3\rangle, \ldots, |\tilde{\psi}_6\rangle$ in terms of $\tilde{\psi}_1$ and $\tilde{\psi}_2$. into the equations for nodes that are not decimated,

$$\begin{aligned}
|\tilde{\psi}_1\rangle &= \mathbf{M}|\tilde{\psi}_1\rangle + \mathbf{A}|\tilde{\psi}_3\rangle + \mathbf{B}|\tilde{\psi}_{\bar{3}}\rangle + \mathbf{C}|\tilde{\psi}_{\bar{\bar{3}}}\rangle \\
|\tilde{\psi}_2\rangle &= \mathbf{M}|\tilde{\psi}_2\rangle + \mathbf{A}|\tilde{\psi}_6\rangle + \mathbf{B}|\tilde{\psi}_{\bar{6}}\rangle + \mathbf{C}|\tilde{\psi}_{\bar{\bar{6}}}\rangle
\end{aligned} \tag{3.13}$$

yields a smaller set of equations self-similar to the above ones where the hopping is now represented by the matrices $\mathbf{A}$, $\mathbf{B}$, $\mathbf{C}$, and $\mathbf{M}$. Due to the simplicity/symmetry of the Grover coin, we find that only two parameters are needed to capture the evolution. The parametrization for the matrices is as follows:

$$\mathbf{A} = \frac{a+b}{2}\mathbf{S}_1 \cdot \mathcal{C}_G \quad \mathbf{B} = \frac{a+b}{2}\mathbf{S}_2 \cdot \mathcal{C}_G \quad \mathbf{C} = \frac{a+b}{2}\mathbf{S}_3 \cdot \mathcal{C}_G \quad \mathbf{M} = \frac{a-b}{2}\mathbb{1} \cdot \mathcal{C}_G \tag{3.14}$$

The components of the 3×3-matrices $\mathbf{S}_i$ are defined by $[S_i]_{k,l} = \delta_{i,k} \cdot \delta_{i,l}$. The recursion equations for the two parameters read

$$\begin{aligned}
a_{k+1} &= \frac{-9a_k+5a_k^3+9b_k+3a_kb_k-17a_k^2b_k-3a_k^3b_k+3b_k^2+14a_kb_k^2-3a_k^2b_k^2-18a_k^3b_k^2}{-18-3a_k+14a_k^2+3a_k^3-3b_k-17a_kb_k+3a_k^2b_k+9a_k^3b_k+5b_k^2-9a_k^2b_k^2} \\
b_{k+1} &= \frac{-3a_k - a_k^2 + 3b_k + 4a_kb_k - 3a_k^2b_k - b_k^2 + 3a_kb_k^2 + 6a_k^2b_k^2}{6 + 3a_k - a_k^2 - 3b_k + 4a_kb_k + 3a_k^2b_k - b_k^2 - 3a_kb_k^2}
\end{aligned} \tag{3.15}$$

with $a_0 = b_0 = z$ as the initial conditions. The ansatz has been chosen because we can show that if $|z| = 1$, $|a_k| = |b_k| = 1$ for all k. This means that the evolution of the two complex variables in equation (3.15) condenses to two phase factors. Unfortunately, there is no easier way of writing the recursions in terms of just the phases.

Evidently, the recursions are more complex than for the random walk. It is not obvious, but there are three fixed points for these equations and we can calculate the eigenvalues of the Jacobian:

$$\begin{aligned} a^* = b^* = 1 \quad &\Longrightarrow \quad \lambda = \{3, 7\} \\ b^* = -a^* \quad &\Longrightarrow \quad \lambda = \{0, 1\} \\ b^* = -(3 + a^*)/(1 + 3a^*)) \quad &\Longrightarrow \quad \lambda = \{1, 5\} \end{aligned} \tag{3.16}$$

Two of them have one undetermined parameter, meaning they correspond to whole lines of fixed points. One might suspect that the first one is related to d_w since the determinant of the Jacobian $3 \cdot 7 = 21$ would reproduce the value of the random walk. We will see below, that this is not true for all networks, but it is indeed the one around which our rescaling method works. The second one seems to be the *absorbing state* towards which a_k and b_k evolve everywhere else, because it could be the only stable one[4]. The third one seems to be not realized with the initial conditions here.

If we now study the rescaling of say $\arg(a_k)$ around the first fixed point[5], we can determine d_w. The result is shown in figure 3.12. The analytic value for λ used for the rescaling can be confirmed to an accuracy that depends on the numbers of iterations performed. For $k \leq 40$ here, we confirm at least 10 digits, meaning that if we change the eleventh digit, we would recognize a broadening of the clear intersection shown in the inset. The accuracy could be easily improved, but already suggests the exactness of $d_w = \log_4\left(\sqrt{21}\right)$ beyond reasonable doubt.

[4] Since one eigenvalue equals one, the stability cannot be concluded from the Jacobian. Higher order terms could both stabilize or destabilize it.

[5] Which parameter or observable we study here is irrelevant. They all collapse for the same λ.

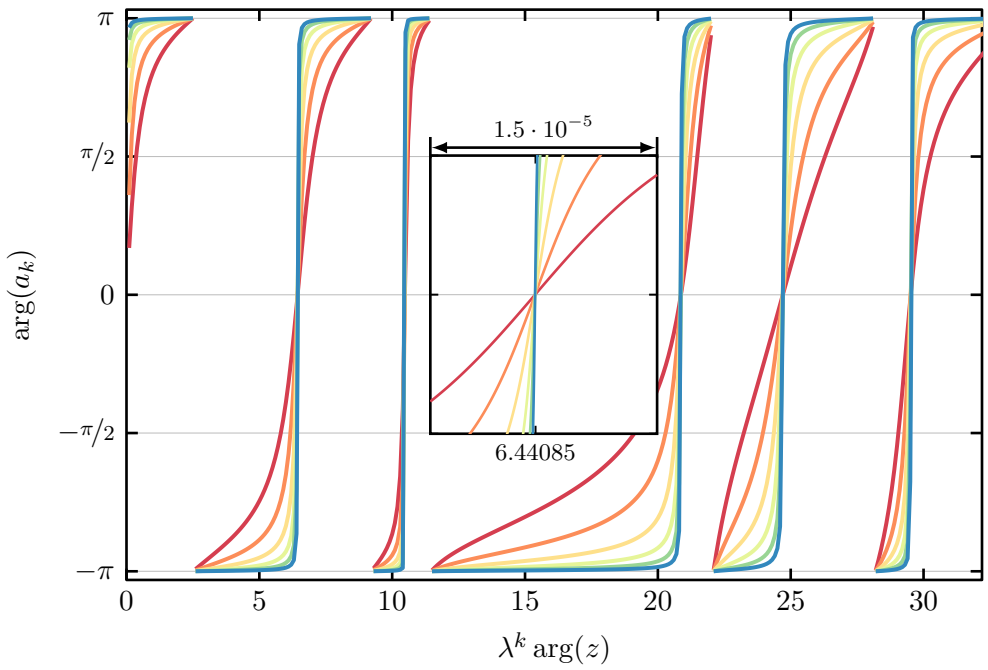

Figure 3.12: Rescaling of the phase of the first parameter a_k around the fixed point $z = 1$ for MK3. The inset shows a magnification around the first intersection. In the main panel, $k = 4, 6, \ldots, 14$ while $k = 30, 32, \ldots 40$ for the inset. This means the largest system size is $N \approx 10^{34}$. $\lambda = \sqrt{21}$ yielding $d_w = \log_4\left(\sqrt{21}\right)$.

For MK4, the linear system for the sites $3, \dots 8$ in figure 3.2 can be written as

$$\begin{aligned}
|\tilde{\psi}_3\rangle &= \mathbf{A}|\tilde{\psi}_1\rangle + \mathbf{M}|\tilde{\psi}_3\rangle + \mathbf{B}|\tilde{\psi}_4\rangle + \mathbf{D}|\tilde{\psi}_7\rangle + \mathbf{C}|\tilde{\psi}_8\rangle \\
|\tilde{\psi}_4\rangle &= \mathbf{B}|\tilde{\psi}_3\rangle + \mathbf{M}|\tilde{\psi}_4\rangle + \mathbf{D}|\tilde{\psi}_5\rangle + \mathbf{C}|\tilde{\psi}_6\rangle + \mathbf{A}|\tilde{\psi}_8\rangle \\
|\tilde{\psi}_5\rangle &= \mathbf{A}|\tilde{\psi}_2\rangle + \mathbf{D}|\tilde{\psi}_4\rangle + \mathbf{M}|\tilde{\psi}_5\rangle + \mathbf{B}|\tilde{\psi}_6\rangle + \mathbf{C}|\tilde{\psi}_7\rangle \\
|\tilde{\psi}_6\rangle &= \mathbf{C}|\tilde{\psi}_4\rangle + \mathbf{B}|\tilde{\psi}_5\rangle + \mathbf{M}|\tilde{\psi}_6\rangle + \mathbf{A}|\tilde{\psi}_7\rangle + \mathbf{D}|\tilde{\psi}_8\rangle \\
|\tilde{\psi}_7\rangle &= \mathbf{D}|\tilde{\psi}_3\rangle + \mathbf{C}|\tilde{\psi}_5\rangle + \mathbf{A}|\tilde{\psi}_6\rangle + \mathbf{M}|\tilde{\psi}_7\rangle + \mathbf{B}|\tilde{\psi}_8\rangle \\
|\tilde{\psi}_8\rangle &= \mathbf{C}|\tilde{\psi}_3\rangle + \mathbf{A}|\tilde{\psi}_4\rangle + \mathbf{D}|\tilde{\psi}_6\rangle + \mathbf{B}|\tilde{\psi}_7\rangle + \mathbf{M}|\tilde{\psi}_8\rangle
\end{aligned} \tag{3.17}$$

Once the solution in terms of $\tilde{\psi}_1$ and $\tilde{\psi}_2$ is found, we can plug it into the equations for, say, $\tilde{\psi}_1$

$$|\tilde{\psi}_1\rangle = \mathbf{A}|\tilde{\psi}_3\rangle + \mathbf{B}|\tilde{\psi}_{\bar{3}}\rangle + \mathbf{C}|\tilde{\psi}_{\bar{\bar{3}}}\rangle + \mathbf{D}|\tilde{\psi}_{\bar{\bar{\bar{3}}}}\rangle \tag{3.18}$$

to find the renormalized system

$$|\tilde{\psi}_1\rangle = \mathbf{A}'|\tilde{\psi}_2\rangle + \mathbf{B}'|\tilde{\psi}_{\bar{2}}\rangle + \mathbf{C}'|\tilde{\psi}_{\bar{\bar{2}}}\rangle + \mathbf{D}'|\tilde{\psi}_{\bar{\bar{\bar{2}}}}\rangle \tag{3.19}$$

Our ansatz for MK4 reads:

$$\begin{aligned}
\mathbf{A}_k &= \frac{a_k + b_k}{2}\mathbf{S}_1 \cdot \mathcal{C}_G \quad \mathbf{B}_k = \frac{a_k + b_k}{2}\mathbf{S}_2 \cdot \mathcal{C}_G \quad \mathbf{C}_k = \frac{a_k + b_k}{2}\mathbf{S}_3 \cdot \mathcal{C}_G \\
\mathbf{D}_k &= \frac{a_k + b_k}{2}\mathbf{S}_4 \cdot \mathcal{C}_G \quad \mathbf{M}_k = \frac{a_k - b_k}{2} \cdot \mathcal{C}_G
\end{aligned} \tag{3.20}$$

Here the $\mathbf{S}_i$ are the four-dimensional matrices defined by $[S_i]_{k,l} = \delta_{i,k} \cdot \delta_{i,l}$. The corresponding recursions for the parameters follow from some algebra:

$$\begin{aligned}
a_{k+1} &= \frac{-8a_k+5a_k^3+a_k^4+(8+4a_k-22a_k^2-a_k^3+5a_k^4)b_k+(4+21a_k+3a_k^2-30a_k^3-4a_k^4)b_k^2+a_k(5+13a_k-4a_k^2-16a_k^3)b_k^3}{-16-4a_k+13a_k^2+5a_k^3+(-4-30a_k+3a_k^2+21a_k^3+4a_k^4)b_k+(5-a_k-22a_k^2+4a_k^3+8a_k^4)b_k^2+(1+5a_k-8a_k^3)b_k^3} \\
b_{k+1} &= \frac{-8b_k+b_k^3+a_k^3b_k(5+4b_k-16b_k^2)+a_k^2(4+13b_k-26b_k^2-12b_k^3)+a_k(8-12b_k-18b_k^2+b_k^3)}{-16-12a_k+a_k^2+a_k^3+2(2-13a_k-9a_k^2)b_k+(5+13a_k-12a_k^2-8a_k^3)b^2+4a_k(1+2a_k)b^3}
\end{aligned} \tag{3.21}$$

with $a_0 = b_0 = z$ as the initial conditions. Again, we crafted the ansatz such that if $|a_k| = |b_k| = 1$ for some k, then it is true for all following iterations.

This system of recursions has the fixed points and corresponding eigenvalues of the Jacobian:

$$\begin{aligned} a^* = b^* = 1 \quad &\Longrightarrow \quad \lambda = \{19/7, 13\} \\ b^* = -1/a^* = 1 \quad &\Longrightarrow \quad \lambda = \{1, 9\} \\ b^* = -\frac{2 + a^*}{1 + 2a^*} \quad &\Longrightarrow \quad \lambda = \{1, 13\} \\ a^* = -b^* \quad &\Longrightarrow \quad \lambda = \{0, 1\} \end{aligned} \tag{3.22}$$

Again, the first one seems to resemble the classical fixed point, and the last one is the *absorbing state*. The other two cannot be reached from the initial conditions. We perform our renormalization procedure again around the unstable fixed point $a^* = b^* = 1$. The rescaling of the phase of the second parameter[6] is shown in figure 3.13. Here we can report confirming $\lambda = \sqrt{247/7}$ and hence $d_w = \log_4\left(\sqrt{247/7}\right)$ to also about 10 digits accuracy.

The decimation for HN3 (see figure 3.3) requires a more complex parametrization. Besides the 3 different hopping parameters **A**, **B** and **C**, we have to account for the necessity to introduce **D** to close the recursion equations. Additionally, there will be two different types of self-interaction terms M_1 and M_2 depending on whether the site index is even or odd. This makes a total of 6 matrices, but for the highly symmetric Grover coin, we only need 3 parameters that can again be shown to be complex variables of modulus one for all

[6] We could also have studied the first parameter, as the behave similarly. The only difference is where the intersections are located, but qualitatively the picture would be the same.

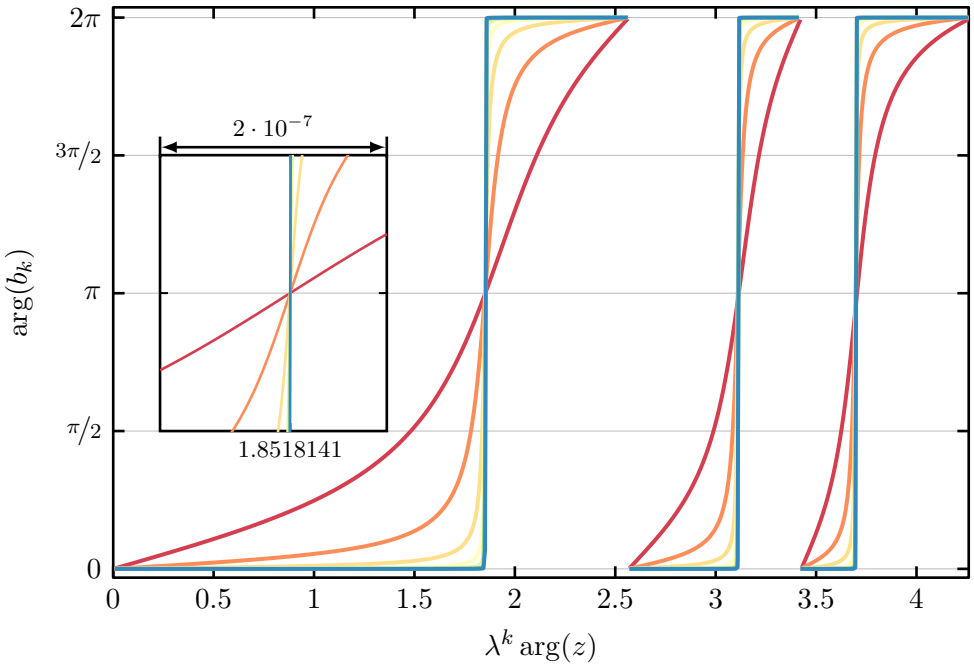

Figure 3.13: Rescaling of the phase of the second RG parameter b_k around the fixed point $z = 1$ for MK4. The inset shows a magnification around the first intersection. In the main panel, $k = 2, 6, \ldots, 14$ while $k = 20, 22, \ldots 30$ for the inset. This means the largest system size is $N = 2 \cdot 13^{30} \approx 5.24 \cdot 10^{33}$. $\lambda = \sqrt{247/7}$ yielding $d_w = \log_{16}(247/7)$.

iterations. We choose the following ansatz for the matrices:

$$\mathbf{A} = \begin{bmatrix} \frac{b-a}{4} & \frac{a+b+2c}{4} & 0 \\ 0 & 0 & 0 \\ 0 & 0 & 0 \end{bmatrix} \cdot \mathcal{C}_G \qquad \mathbf{B} = \begin{bmatrix} 0 & 0 & 0 \\ \frac{a+b+2c}{4} & \frac{b-a}{4} & 0 \\ 0 & 0 & 0 \end{bmatrix} \cdot \mathcal{C}_G$$
$$\mathbf{C} = \begin{bmatrix} 0 & 0 & 0 \\ 0 & 0 & 0 \\ 0 & 0 & z \end{bmatrix} \cdot \mathcal{C}_G \qquad \mathbf{D} = \begin{bmatrix} 0 & \frac{b-a}{4} & 0 \\ 0 & 0 & 0 \\ 0 & 0 & 0 \end{bmatrix} \cdot \mathcal{C}_G \tag{3.23}$$
$$\mathbf{M}_1 = \begin{bmatrix} \frac{a+b-2c}{4} & \frac{b-a}{4} & 0 \\ \frac{b-a}{4} & \frac{a+b-2c}{4} & 0 \\ 0 & 0 & 0 \end{bmatrix} \cdot \mathcal{C}_G \quad \mathbf{M}_2 = \begin{bmatrix} \frac{a+b-2c}{4} & 0 & 0 \\ 0 & \frac{a+b-2c}{4} & 0 \\ 0 & 0 & 0 \end{bmatrix} \cdot \mathcal{C}_G$$

The linear system we need to solve in this case reads

$$\begin{aligned} |\tilde{\psi}_4\rangle &= \mathbf{A}^T|\tilde{\psi}_1\rangle + \mathbf{B}^T|\tilde{\psi}_2\rangle + \mathbf{M}_1|\tilde{\psi}_4\rangle + \mathbf{C}|\tilde{\psi}_5\rangle \\ |\tilde{\psi}_5\rangle &= \mathbf{A}^T|\tilde{\psi}_2\rangle + \mathbf{B}^T|\tilde{\psi}_3\rangle + \mathbf{C}^T|\tilde{\psi}_4\rangle + \mathbf{M}_1|\tilde{\psi}_5\rangle \end{aligned} \tag{3.24}$$

corresponds to the right graphlet in Fig. 3.3. Here $\mathbf{A}^T$ represents the transpose of $\mathbf{A}$. As it turns out, the different bonds can become asymmetric depending which direction (left or right in the figure) the quantum walker takes, and this ansatz automatically accounts for it.

By solving these equations for $|\tilde{\psi}_4\rangle$ and $|\tilde{\psi}_5\rangle$, and inserting this into the equations for the remaining sites,

$$\begin{aligned} |\tilde{\psi}_1\rangle &= \mathbf{M}_2|\tilde{\psi}_1\rangle + \mathbf{D}|\tilde{\psi}_2\rangle + \mathbf{D}^T|\tilde{\psi}_{\bar{2}}\rangle + \mathbf{A}|\tilde{\psi}_4\rangle + \mathbf{B}^T|\tilde{\psi}_{\bar{5}}\rangle + \mathbf{C}|\tilde{\psi}_*\rangle \\ |\tilde{\psi}_2\rangle &= \mathbf{D}|\tilde{\psi}_1\rangle + \mathbf{M}_2|\tilde{\psi}_2\rangle + \mathbf{D}^T|\tilde{\psi}_3\rangle + \mathbf{B}^T|\tilde{\psi}_4\rangle + \mathbf{A}|\tilde{\psi}_5\rangle + \mathbf{C}|\tilde{\psi}_*\rangle \end{aligned} \tag{3.25}$$

we find the following recursion equations for the three RG variables. Note that the equation for $\tilde{\psi}_3$ is identical to the first one, and every node is connected to a node of unknown index,

$\tilde{\psi}_*$, but the corresponding hopping matrix $\mathbf{C}$ does not change. After some algebra, we find

$$\begin{aligned} a_{k+1} &= \frac{c_k(-3+z) - b_k(-3+z+c_k(-2+6z))}{6 - b_k + c_k + (-2+3b_k-3c_k)z}\,, \\ b_{k+1} &= \frac{c_k(3+z) - b_k(3+z+c_k(2+6z))}{-6 + b_k - c_k + (-2+3b_k-3c_k)z}\,, \\ c_{k+1} &= \frac{c_k + a_k(-1+2c_k)}{2 + a_k - c_k}\,, \end{aligned} \tag{3.26}$$

with the initial conditions

$$a_0 = \frac{z^2(1-3z)}{3-z}\,, \quad b_0 = \frac{z^2(1+3z)}{3+z}\,, \quad c_0 = z^2\,. \tag{3.27}$$

The ansatz again leads to variables that stay of modulus one through all iterations, if the initial conditions fulfill this condition. Note that the equations explicitly depend on z because of the unrenormalized matrix $\mathbf{C}$.

The recursions have the following fixed points and corresponding eigenvalues of the Jacobian:

$$\begin{aligned} b^* = c^* = -a^* &\quad\Longrightarrow\quad \lambda = \{0,0,1\} \\ (a^*,b^*,c^*) = \left(\frac{-3+z(6+z)}{-1+3(-2+z)z}, \frac{3+z}{1+3z}, 1\right) &\quad\Longrightarrow\quad \lambda = \{0,2,2\} \\ (a^*,b^*,c^*) = \left(\frac{-3+z}{-1+3z}, \frac{3-z}{-1+3z}, \frac{3+z}{1+3z}\right) &\quad\Longrightarrow\quad \lambda = \left\{\frac{1+\sqrt{17}}{4}, \frac{1-\sqrt{17}}{4}, 2\right\} \end{aligned} \tag{3.28}$$

Remarkably, the last two fixed points depend explicitly on z while the eigenvalues do not.

At this point, it becomes clear that the fixed points for the renormalization of the quantum walk are not necessarily linked to values encountered for the random walk. Here, our rescaling works around the last fixed point. The results for rescaling the phase of the first parameter are presented in figure 3.14. The rescaling here is not quite as nice as for the previous networks. Not all curves intersect at exactly the same point. Therefore, we look at the convergence of the kink towards a step function and how that drifts when the value of λ is changed to estimate the accuracy. Due to the smaller effective system size,

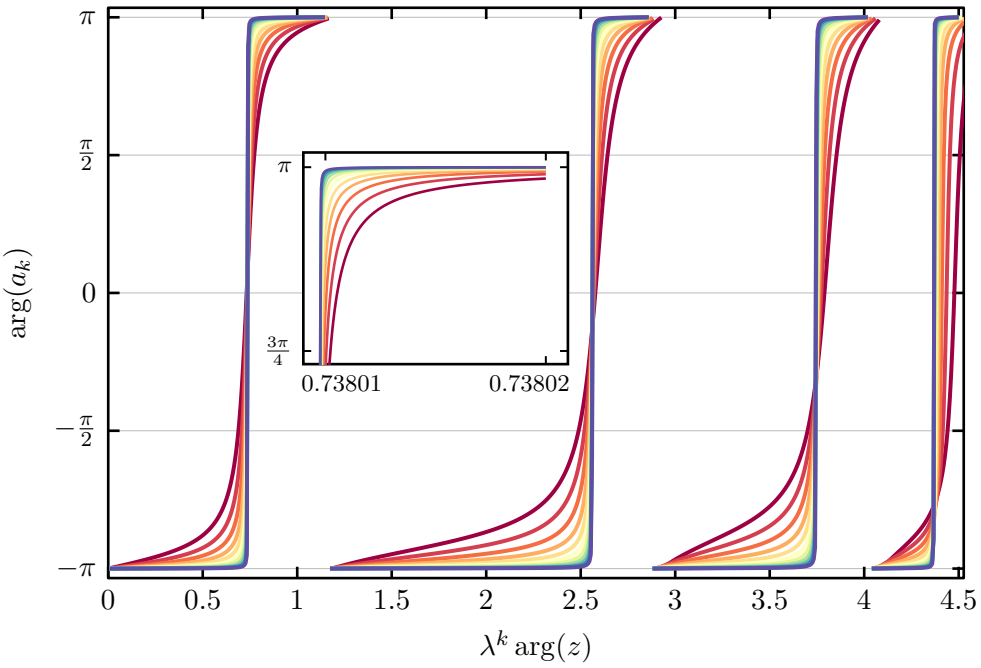

Figure 3.14: Rescaling of the phase of the first RG parameter a_k around the fixed point $z = 1$. The insets show a magnification to illustrate the conversion towards a step function. In the main panel, $k = 10, 12, \ldots, 30$ while $k = 60, 62, \ldots 80$ for the inset. This means the largest system size is $N \approx 10^{24}$. $\lambda = \sqrt{24 - 8\sqrt{5}}$ yielding $d_w = \log_4\left(24 - 8\sqrt{5}\right)$.

we confirm $d_w = \log_2(24 - 8\sqrt{5})/2$ to about 8 digits.

In case of the DSG, the linear system represented by figure 3.4 reads

$$
\begin{aligned}
|\tilde{\psi}_4\rangle &= \mathbf{B}|\tilde{\psi}_1\rangle + \mathbf{M}|\tilde{\psi}_4\rangle + \mathbf{A}|\tilde{\psi}_5\rangle + \mathbf{C}|\tilde{\psi}_9\rangle \\
|\tilde{\psi}_5\rangle &= \mathbf{A}|\tilde{\psi}_1\rangle + \mathbf{B}|\tilde{\psi}_4\rangle + \mathbf{M}|\tilde{\psi}_5\rangle + \mathbf{C}|\tilde{\psi}_6\rangle \\
|\tilde{\psi}_6\rangle &= \mathbf{B}|\tilde{\psi}_3\rangle + \mathbf{C}|\tilde{\psi}_5\rangle + \mathbf{M}|\tilde{\psi}_6\rangle + \mathbf{A}|\tilde{\psi}_7\rangle \\
|\tilde{\psi}_7\rangle &= \mathbf{A}|\tilde{\psi}_3\rangle + \mathbf{B}|\tilde{\psi}_6\rangle + \mathbf{M}|\tilde{\psi}_7\rangle + \mathbf{C}|\tilde{\psi}_8\rangle \\
|\tilde{\psi}_8\rangle &= \mathbf{B}|\tilde{\psi}_2\rangle + \mathbf{C}|\tilde{\psi}_7\rangle + \mathbf{M}|\tilde{\psi}_8\rangle + \mathbf{A}|\tilde{\psi}_9\rangle \\
|\tilde{\psi}_9\rangle &= \mathbf{A}|\tilde{\psi}_2\rangle + \mathbf{C}|\tilde{\psi}_4\rangle + \mathbf{B}|\tilde{\psi}_8\rangle + \mathbf{M}|\tilde{\psi}_9\rangle
\end{aligned}
\tag{3.29}
$$

We solve for the *inner* nodes in terms of the *outer*, and eliminate the former ones from

$$\begin{aligned}
|\tilde{\psi}_1\rangle &= \mathbf{M}|\tilde{\psi}_1\rangle + \mathbf{C}|\tilde{\psi}_{\bar{2}/\bar{3}}\rangle + \mathbf{A}|\tilde{\psi}_4\rangle + \mathbf{B}|\tilde{\psi}_5\rangle \\
|\tilde{\psi}_2\rangle &= \mathbf{C}|\tilde{\psi}_{\bar{1}}\rangle + \mathbf{M}|\tilde{\psi}_3\rangle + \mathbf{A}|\tilde{\psi}_6\rangle + \mathbf{B}|\tilde{\psi}_7\rangle \\
|\tilde{\psi}_2\rangle &= \mathbf{C}|\tilde{\psi}_{\bar{1}}\rangle + \mathbf{M}|\tilde{\psi}_2\rangle + \mathbf{A}|\tilde{\psi}_8\rangle + \mathbf{B}|\tilde{\psi}_9\rangle
\end{aligned} \tag{3.30}$$

The parametrization of the matrices requires five variables:

$$\begin{aligned}
\mathbf{A} &= \begin{bmatrix} a & b & 0 \\ b & c & 0 \\ 0 & 0 & 0 \end{bmatrix} \quad \mathbf{B} = \begin{bmatrix} c & b & 0 \\ b & a & 0 \\ 0 & 0 & 0 \end{bmatrix} \\
\mathbf{C} &= \begin{bmatrix} 0 & 0 & 0 \\ 0 & 0 & 0 \\ 0 & 0 & z \end{bmatrix} \quad \mathbf{M} = \begin{bmatrix} d & e & 0 \\ e & d & 0 \\ 0 & 0 & 0 \end{bmatrix}
\end{aligned} \tag{3.31}$$

At this point, the algebra becomes very complex but still manageable with computer algebra systems. While we can still find symbolic expressions for the recursion equations, each is a rational function with dozens of terms in numerator and denominator. We can only find two fixed points although there might be more.

$$\begin{aligned}
a^* = b^* = c^* = d^* = -e^*/2 = -1/3 \quad &\Longrightarrow \quad \lambda = \{0, 1/3, 1, 5/3, 3\} \\
a^* = b^* = c^* = 0 \quad &\Longrightarrow \quad \lambda = \{0, 0, 0, 1, 1\}
\end{aligned} \tag{3.32}$$

The rescaling is performed around the first one.

The scaling plot in figure 3.15 is different from the ones above. First of all, we show a function of all parameters whose integral around the unit circle corresponds to F_0, the absorption probability when absorbing boundaries are introduced, see section 4.3 for the modified network. This relates back to our arguments in section 2.4, but this should always be equivalent to scaling the parameters directly. Another difference is that $z = -1$ is the

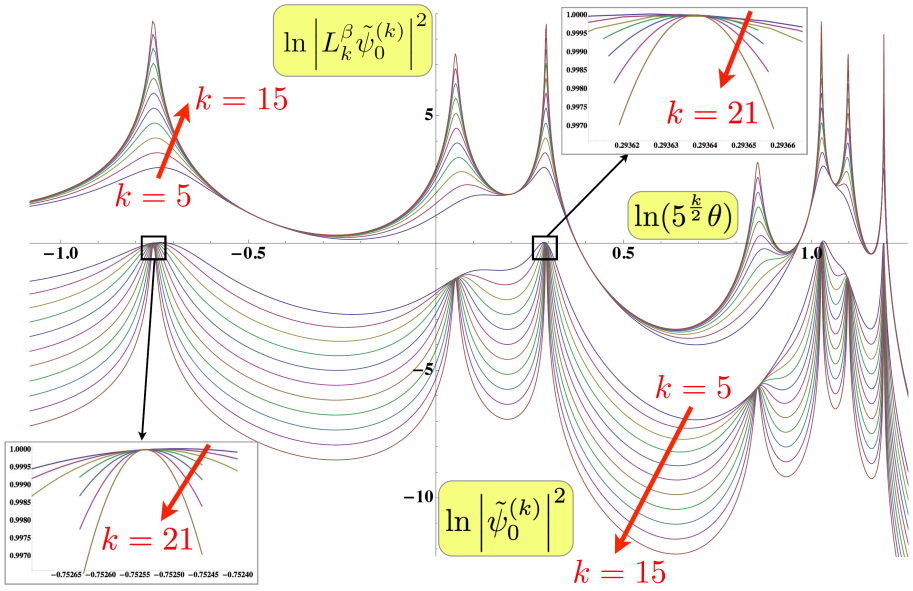

Figure 3.15: Rescaling of $\theta = \pi - \arg(z)$ around the only found fixed point $z = -1$. The lower panel show that the peaks align and converge uniformly (see insets), while the function converges to zero in between. In the upper part, we also rescale the y axis. This makes the peaks diverge, but aligns the regions between them.[13]

fixed point around which the scaling works, for all other networks it is $z = 1$ as in the classical case. Finally, we want to point out the logarithms x axis. The scaling is confined to a very small region for $\theta = \pi - \arg(z)$. We inverstigate that further in the last part of chapter 4. The rescaling is done with $\lambda = \sqrt{5}$ or $d_w = \log_4(5)$ respectively.

All four networks fulfill the remarkable relationship

$$d_w^{QW} = \frac{1}{2} d_w^{RW} \tag{3.33}$$

if the Grover coin $\mathcal{C}_G$ is used. It is also true for every hypercubic lattice where $d_w^{RW} = 2$ and $d_w^{QW} = 1$ as discussed earlier. This leads us to conjecture that this relationship holds universally. Although we only studied self-similar networks using a not completely understood renormalization group scheme, we back up our claim by large numerical simulations with unprecedented system sizes.

Table 3.3: Parameters for the simulation shown in figure 3.16 using the Fourier coin. The networks with N nodes, and the maximum distance l_{max} from the initial condition where evolved for t_{max} time steps. The colors in the plots correspond to t_{min} (blue) in powers of 2 up to t_{max} (red). See text for discussion.

Network	N	l_{max}	t_{min}	t_{max}	d_w^{est}
MK3	$2 \cdot 7^8 \approx 1.2 \cdot 10^7$	2^{16}	2^{10}	2^{16}	1.20(2)
MK4	$2 \cdot 13^6 \approx 1.0 \cdot 10^7$	2^{12}	2^8	2^{14}	1.72(2)
HN3	$2^{24} \approx 1.7 \cdot 10^7$	2^{12}	2^7	2^{13}	1.69(1)
DSG	$2 \cdot 3^{14} \approx 1.0 \cdot 10^7$	2^{12}	2^8	2^{14}	1.61(5)

3.3.2 The Fourier Coin

The Fourier coin is is an easily constructed *balanced* coin for all dimensions. This means that all matrix entries are of the same magnitude. As a result, if one would measure the state of the quantum walker after each time step, this coin would resemble the random walk. As a downside, this coin is less symmetric and inherently complex-valued, which is why the number of parameters increases, and the recursion equations become more complicated. For our three and four regular networks, the coin reads

$$\mathcal{C}_F = \frac{1}{\sqrt{3}} \begin{bmatrix} 1 & 1 & 1 \\ 1 & \mathrm{e}^{2\pi \mathrm{i}/3} & \mathrm{e}^{-2\pi \mathrm{i}/3} \\ 1 & \mathrm{e}^{-2\pi \mathrm{i}/3} & \mathrm{e}^{2\pi \mathrm{i}/3} \end{bmatrix} \qquad \text{and} \qquad \mathcal{C}_F = \frac{1}{2} \begin{bmatrix} 1 & 1 & 1 & 1 \\ 1 & -\mathrm{i} & -1 & \mathrm{i} \\ 1 & -1 & 1 & -1 \\ 1 & \mathrm{i} & -1 & -\mathrm{i} \end{bmatrix}, \tag{3.34}$$

respectively.

We again start with direct simulations and our procedure to estimate d_w numerically. Figure 3.16 shows the best rescaling of the PDFs, and the numbers can be found in table 3.3.

The scaling function exhibits several differences compared to the Grove case. The shape is slightly different from the ones in figure 3.11: There is still a plateau followed by a decrease, but the pronounced peak towards $l/t^{1/d_w} \to 0$ disappeared. This agrees with our observation that there is either less or no localization at all for the Fourier coin, an effect

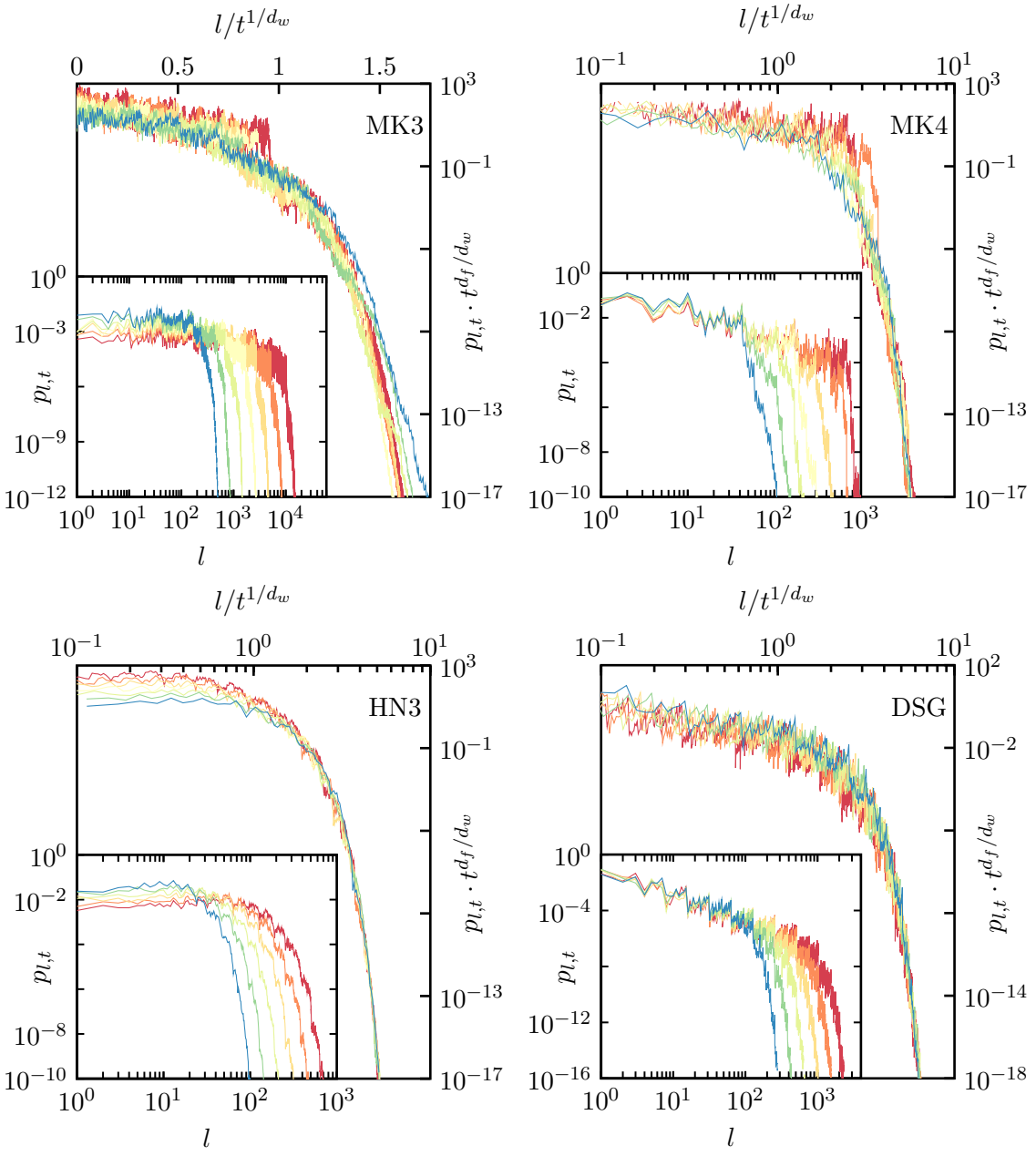

Figure 3.16: Direct simulation of the quantum walk using the Fourier coin on all four networks. The insets show the raw PDFs, while the main panel shows the best fit. The parameters of all simulations and the estimated values for d_w can be found in table 3.3. Note the logarithmic x-axis for 3 of the main panels.

known on the two dimensional square lattice [58]. Furthermore, note the logarithmic x axis for MK4, HN3 and DSG. On these networks, the scaling functions decays slower as a function of $l/t^{1/d_w}$.

The estimated values for the walk dimension are consistently larger compared to the ones in table 3.2, but there is no obvious pattern the numbers follow with respect to the random walk, or the quantum walk using the Grover coin. All we can conclude from the numerics is the fact that $\mathcal{C}_G$ seems to lead to a faster spreading than $\mathcal{C}_F$, but localization is also stronger present in the first case. This seems to hold except for the DSG, where the scaling function still could diverge for $l/t^{1/d_w} \to 0$.

While the renormalization procedure is identical to the one presented for the Grover coin, the complex entries and the asymmetry of the Fourier coin render it impossible to show recursion equations here. The number of parameters is twice that necessary for $\mathcal{C}_G$ on all networks, and the recursions are rational functions with dozens of terms in numerator and denominator. Although we can still study the recursions numerically, we were unable to find an unstable fixed point, only stable ones. This means, that we cannot perform the rescaling of the parameters as we did earlier. To use the renormalization group here, we lack the proper understanding of how to extract the scaling of observables in a case without an unstable fixed point. The numerical rescaling shows at least that the scaling relation (2.2) still holds reasonably well. The long time scaling must be determined by a different property of the recursion equations that is potentially retrievable without an explicit solution.

3.3.3 An orthogonal Coin

The two coins presented above do not represent the full spectrum of possibilities. As a first step in a categorization of all different behaviors, we will study a previously ignored coin. While $\mathcal{C}_G$ belongs to a very special class of self-inverse reflections[7], and the Fourier

[7] Technically, it is also a rotation about 180°, but being self inverse and symmetric sets it apart from general rotations, for example.

coin is a specimen from the special unitary matrices without any particular symmetry or property other than the same magnitude for any element in the matrix, we introduce a rotation that can be defined in every dimension r of the coin space:

$$\mathcal{C}_O = \frac{2}{r}\begin{bmatrix} 1 & 1-\frac{r}{2} & 1 & 1 & \dots & 1 \\ 1 & 1 & 1-\frac{r}{2} & 1 & \dots & 1 \\ \vdots & \ddots & \ddots & \ddots & \ddots & \vdots \\ 1-\frac{2}{r} & 1 & 1 & 1 & \dots & 1 \end{bmatrix} \tag{3.35}$$

Though not obvious, this definition closely resembles the Grover coin, with one major difference: Not the main diagonal, but the one above it, and the last element in the first column are now distinct. We found this coin suitable for our numerical procedure, as well as for our renormalization procedure. The subscript O symbolizes that it is an orthogonal coin[8]. For the three and four dimensional coin spaces, this coin reads

$$\mathcal{C}_O = \frac{1}{3}\begin{bmatrix} 2 & -1 & 2 \\ 2 & 2 & -1 \\ -1 & 2 & 2 \end{bmatrix} \quad \text{and} \quad \mathcal{C}_O = \frac{1}{2}\begin{bmatrix} 1 & -1 & 1 & 1 \\ 1 & 1 & -1 & 1 \\ 1 & 1 & 1 & -1 \\ -1 & 1 & 1 & 1 \end{bmatrix} \tag{3.36}$$

First, we simulate the quantum walk using this coin on our four networks. All parameters and the corresponding rescaling plots can be found in table 3.4 and figure 3.17.

The rescaling for MK4 and DSG is very similar to what we found for the Fourier coin. Note that the values for the DSG are very close, where we see a noticeable difference for MK4. Doing the renormalization procedure, we encounter the same problems as with $\mathcal{C}_F$, namely that the recursion equations are too long to show here, seem to have no unstable fixed point, and hence our procedure does not apply.

More surprising, our findings for MK3 and HN3 suggest a ballistic spreading for this

[8]The Grover coin also belongs to this class, but because of its distinct properties we do not expect it to be representative.

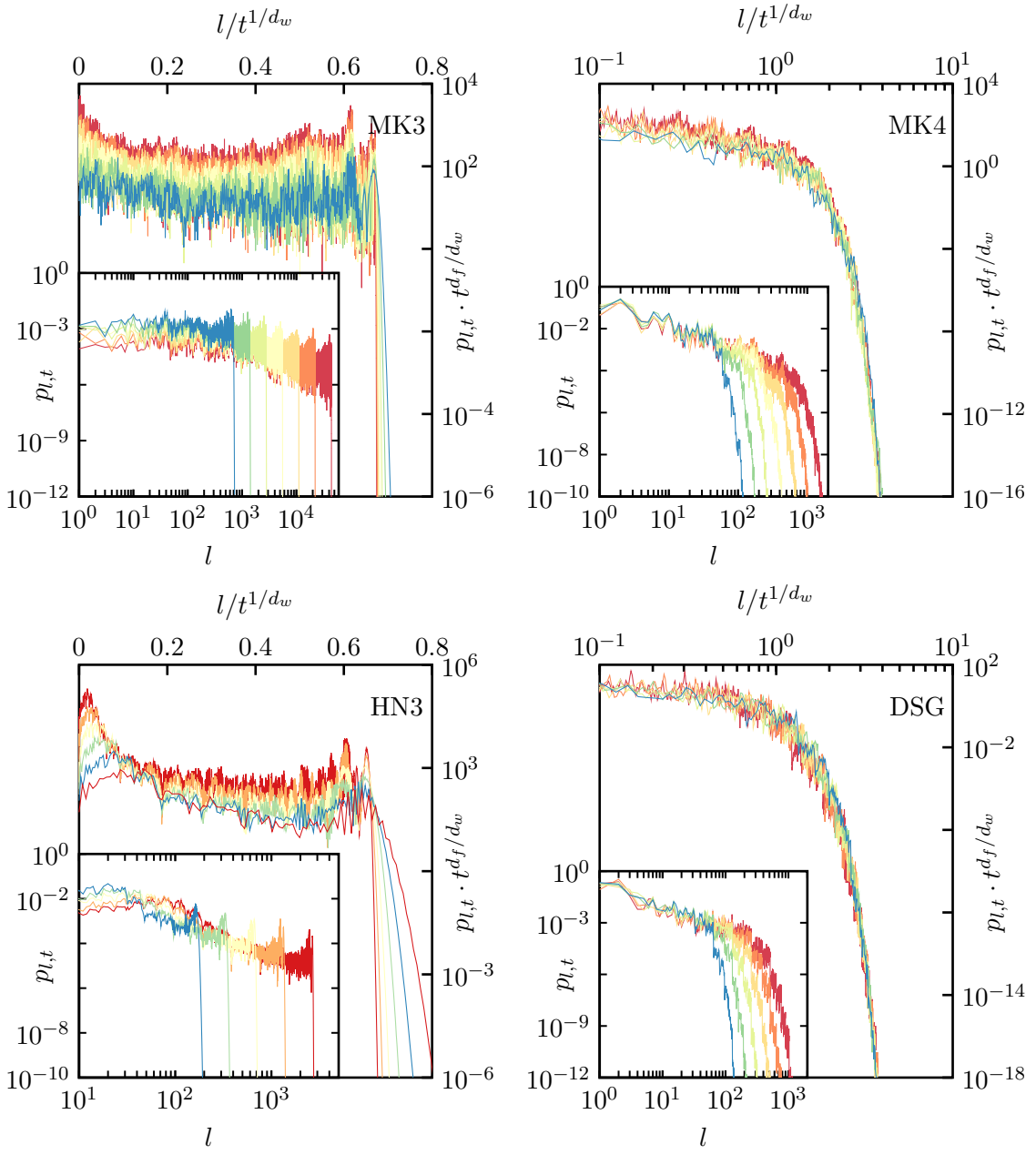

Figure 3.17: Direct simulation of the quantum walk using an orthogonal coin on all four networks. The insets show the raw PDFs, while the main panel shows the best fit. The parameters of all simulations and the estimated values for d_w can be found in table 3.4.

Table 3.4: Parameters for the simulation shown in figure 3.17 using an orthogonal coin. The networks with N nodes, and the maximum distance l_{max} from the initial condition where evolved for t_{max} time steps. The colors in the plots correspond to t_{min} (blue) in powers of 2 up to t_{max} (red). See text for discussion.

Network	N	l_{max}	t_{min}	t_{max}	d_w^{est}
MK3	$2 \cdot 7^8 \approx 1.2 \cdot 10^7$	2^{16}	2^{10}	2^{16}	1.008(4)
MK4	$2 \cdot 13^6 \approx 1.0 \cdot 10^7$	2^{12}	2^8	2^{14}	1.51(1)
HN3	$2^{24} \approx 1.7 \cdot 10^7$	2^{12}	2^7	2^{13}	1.04(2)
DSG	$2 \cdot 3^{14} \approx 1.0 \cdot 10^7$	2^{12}	2^8	2^{14}	1.61(2)

coin. While on lattices the quantum walk spreads quadratically faster, i.e. $d_w^{QW} = d_w^{RW}/2$, for a almost[9] any coin, we find a strong dependence on the coin for networks without translational invariance. Additionally, we seem to have found a coin that spreads at the limit[10] of $d_w = 1$ on some networks. To our knowledge, a non-trivial, ballistic motion[11] for quantum walks on complex networks has not been observed previously.

We now look at the recursion equations on MK3 and see whether the rescaling around a fixed point confirms this observation. The procedure for HN3 requires 6 instead of 3 parameters, and the recursion equations are too complex to be shown here. Furthermore, the rescaling seems not to work around the one fixed point we find. This will require more investigation in the future.

For MK3, we can use the same parametrization as in equation (3.14), but the corre-

[9] Exceptions are coins where the time evolution is trivial, i.e. no spreading whatsoever.

[10] Values $d_w < 1$ are impossible when distances are measured as the shortest path length. The walk cannot hop more than once at each time step.

[11] On some networks one can construct a coin such that the quantum walk will move deterministically increasing the distance to the initial site at each time step. On the DSG, the alternating sequence of **A** and **C**, for example, leads to such a case.

sponding recursions read

$$\begin{aligned} a_{k+1} = &\big[-6b_k(3+4b_k+2b_k^2) - a_k^4(13+44b_k+60b_k^2+36b_k^3) \\ &+ a_k(18+84b_k+104b_k^2+55b_k^3) + a_k^3(32+119b_k+152b_k^2+84b_k^3) \\ &-a_k^2(36+140b_k+173b_k^2+92b_k^3)\big] \,/\, \big[36+60b_k+44b_k^2+13b_k^3 \\ &+ 6a_k^4(2+4b_k+3b_k^2) - a_k^3(55+104b_k+84b_k^2+18b_k^3) \\ &- a_k(84+152b_k+119b_k^2+32b_k^3) + a_k^2(92+173b_k+140b_k^2+36b_k^3)\big] \\ b_{k+1} = &\frac{b_k(3+2b_k) + a_k^2(2+6b_k+6b_k^2) - a_k(3+8b_k+6b_k^2)}{a_k^2(2+3b_k) + 2(3+3b_k+b_k^2) - a_k(6+8b_k+3b_k^2)} \end{aligned} \tag{3.37}$$

Immediately, we notice that they are more complex compared to the Grover coin equations (3.15). We are still able to find all the fixed points and the corresponding eigenvalues

$$\begin{aligned} a^* = \frac{2}{3} \qquad b^* = -\frac{5}{4} \qquad &\Longrightarrow \quad \lambda = \{1,5\} \\ b^* = -a^* \qquad &\Longrightarrow \quad \lambda = \{0,1\} \\ b^* = \frac{2-2a^* \pm \sqrt{5a-2a^2-2}}{3a-2} \qquad &\Longrightarrow \quad \lambda = \{1,5\} \end{aligned} \tag{3.38}$$

Here the second one is the absorbing state, the last one is realized with $a^* = b^* = 1$ for $z = 1$, which is where the scaling in figure 3.18 is performed. Our rescaling of the phase[12] of a_k yields $\lambda = 4$ or $d_w = 1$ correspondingly. To estimate the accuracy we looked at the first root of $\arg(a_k)$ for $\lambda^k \arg(z) > 0$ at different system sizes. For $\lambda \neq 4$ it was easy to see a broadening of this point even for the system sizes shown in the figure. Without going to larger system size we can confirm this value to about 10 digits accuracy.

[12]The two parameters are again of modulus one with the particular ansatz.

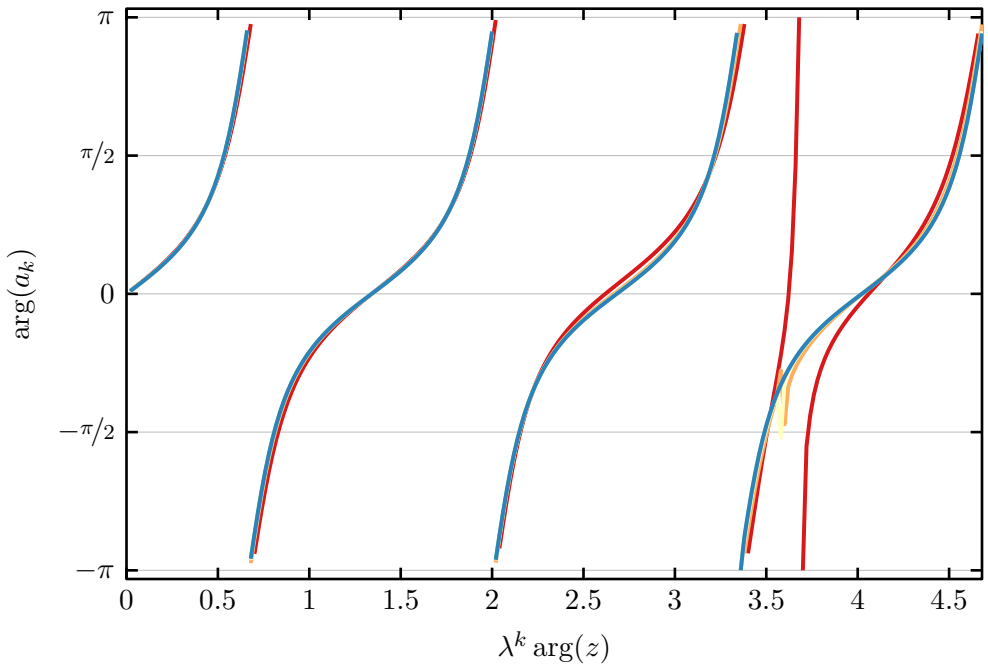

Figure 3.18: Rescaling of the phase of the first parameter a_k around the fixed point $z = 1$ for MK3 using $\mathcal{C}_O$. The different curves correspond to $k = 4, 6, \ldots, 12$ (red to blue), resulting in a system size of $N \approx 10^7$. $\lambda = 4$ yielding $d_w = 1$.

3.4 Remarks

The first two coins presented here constitute the most studied choices for quantum walks. Considering the 8 parameters for the most general $SU(3)$ matrix[13], and 15 for $SU(4)$, the natural questions of universality arises: How does the choice of the coin influence the long time behavior? Are there certain classes of coins that all have the same asymptotic properties? This question has been very well understood for random walks [34, 57]. The newly studied orthogonal coin $\mathcal{C}_O$ merely shows the potential by giving the first known example for ballistic spreading on a network lacking translational invariance. It also demonstrates the direct impact of the network as this is only true for two of our networks. But the parameter space is still vastly unexplored, so that a ballistically spreading coin could potentially be found for every network. While searching for other suitable coins, we also discovered a coin, namely

$$\mathcal{C} = \frac{1}{2}\begin{bmatrix} 1 & \sqrt{2} & 1 \\ -\sqrt{2} & 0 & \sqrt{2} \\ 1 & -\sqrt{2} & 1 \end{bmatrix},$$

where we know that it does not have any unstable fixed points, because we can solve the fixed point equations, but it numerically yields a d_w very close to $\mathcal{C}_G$ on MK3. This example gives at least hope that there is a chance to refine the renormalization group treatment to work for coins without unstable fixed points. It shows that there might be other properties of the recursions that cause a particular walk dimension.

[13] The special unitary group is enough to represent all relevant coins possible. The missing phase factor for $U(3)$ has no influence on observables which are invariant under multiplication by a factor of modulus one.

4 Localization in quantum walks without disorder

"What're quantum mechanics?"
"I don't know. People who repair quantums, I suppose."

Terry Pratchett, Eric

The results in chapter 3 suggest that localization is common in quantum walks. To further investigate this issue, we consider the easiest quantum walk with this property in section 4.2: the one dimensional quantum walk with a three dimensional coin. As a precursor, we solve a similar classical random walk in section 4.1 to gain familiarity with the methods used, and to show that this phenomenon is not possible in random walks without disorder. In the last section 4.3, we show numerical results on the Dual Sierpinski Gasket (DSG) to shed some light on this topic on self-similar networks.

4.1 The one dimensional random walk

As a preparation for the calculations for the three-state quantum walk on the line, we will study a similar random walk first to lay out the basic tools needed. The walk presented here allows the walker to not move and remain at a site during a time step with probability $1/2$. If it moves it will go with equal probability to the left or to the right[1]. For this case,

[1] We choose these particular probabilities for easier expressions in the following calculations. The actual numbers are irrelevant for the asymptotic scaling.

equation 2.1 for any component reads

$$p_{m,t+1} = \frac{1}{4}p_{m-1,t} + \frac{1}{4}p_{m+1,t} + \frac{1}{2}p_{m,t} \qquad \forall m \tag{4.1}$$

The translational invariance suggests a description in Fourier space, by using the discrete Fourier transform and its inverse:

$$\tilde{p}_t(k) = \sum_{m=-\infty}^{\infty} p_{m,t} \cdot \mathrm{e}^{-\mathrm{i}km} \qquad\qquad p_{m,t} = \frac{1}{2\pi}\int_{-\pi}^{\pi} \tilde{p}_t(k) \cdot \mathrm{e}^{\mathrm{i}km}\,\mathrm{d}k \tag{4.2}$$

By multiplying equation (4.1) by $\mathrm{e}^{-\mathrm{i}km}$ and summing over all m, we find the master equation in Fourier space

$$\tilde{p}_{t+1}(k) = \cos^2\left(\frac{k}{2}\right)\tilde{p}_t(k) \qquad\qquad \tilde{p}_{t=0}(k) = 1 \tag{4.3}$$

where we assumed (without loss of generality) $m_0 = 0$ as the initial position. The real space solution then has to be reconstructed from the easily obtained solution

$$\tilde{p}_t(k) = \cos^{2t}\left(\frac{k}{2}\right)\,. \tag{4.4}$$

Although this integral can be solved exactly in terms of hypergeometric functions, we will solve it approximately using the method of steepest descent [10]. This yields not only a very familiar result, it also shows the approximation scheme used for the quantum walk where analytic results might not be obtainable. The method allows us to evaluate the integral in (4.2) approximately for large times. Before we apply any approximation, we rewrite the inverse Fourier transform as

$$p_{m,t} = \frac{1}{2\pi}\int_{-\pi}^{\pi} \mathrm{e}^{\mathrm{i}km} \cdot \cos^{2t}\left(\frac{k}{2}\right)\,\mathrm{d}k = \frac{1}{2\pi}\int_{-\pi}^{\pi} \mathrm{e}^{t[\mathrm{i}km/t + 2\log(\cos(k/2))]}\,\mathrm{d}k\,. \tag{4.5}$$

The idea now is to find the saddle points in the complex k plane of the exponent and bend the path of integration through them. Then, these points will dominate the asymptotic behavior of the integral, and we can find an approximation by expanding the exponent to second order. This yields a solvable Gaussian integral which will reproduce a familiar result. By considering higher orders, one could find systematically better approximation, but for most purposes this is unnecessary.

With the definitions

$$v = \frac{m}{t} \qquad (4.6) \qquad\qquad \varphi(k) = \mathrm{i}kv + 2\log\left(\cos\left(\frac{k}{2}\right)\right) \qquad (4.7)$$

the integral of interest reads

$$p_{1,t} = \frac{1}{2\pi}\int_{-\pi}^{\pi} \mathrm{e}^{t\cdot\varphi(k)}\,\mathrm{d}k\,, \qquad (4.8)$$

and the saddle point is given by

$$\left.\frac{\mathrm{d}\varphi}{\mathrm{d}k}\right|_{k=k^*} = 0 \qquad \Longleftrightarrow \qquad k^* = 2\mathrm{i}\cdot\operatorname{arctanh}(v) \qquad (4.9)$$

At this point

$$\varphi(k^*) = -(1-v)\log(1-v) - (1+v)\log(1+v) \qquad \text{and} \qquad \varphi''(k^*) = -\frac{1-v^2}{2}\,. \qquad (4.10)$$

Note that because the walk could move every time step, $-1 \leq v \leq 1$, and everything is symmetric around $v = 0$ as one would expect in this case. The approximation now becomes

$$\begin{aligned} p_{m,t} &\approx \frac{1}{2\pi}\int_{-\infty}^{\infty} \mathrm{e}^{t\varphi(k^*)+\frac{t\varphi''(k^*)}{2}(k-k^*)^2}\,\mathrm{d}k \\ &= \frac{\mathrm{e}^{t\varphi(k^*)}}{2\pi}\int_{-\infty}^{\infty} \mathrm{e}^{\frac{t\varphi''(k^*)}{2}(k-k^*)^2}\,\mathrm{d}k \\ &= \frac{\mathrm{e}^{t\varphi(k^*)}}{2\pi}\frac{\sqrt{2\pi}}{\sqrt{-t\varphi''(k^*)}} = \frac{1}{\sqrt{2\pi t|\varphi''(k^*)|}}\,\mathrm{e}^{t\varphi(k^*)} \end{aligned} \qquad (4.11)$$

where we deformed the path of integration and extended the integral in the neighborhood of the saddle point out to infinity. We did not have to worry about rotating the path of integration here as φ'' was already negative. This would add a phase factor to the final result, and will become necessary for the quantum walk. A more detailed argument of this can be found in [10].

As it turns out, $\varphi(k^*)$ is negative except for $v = m/t = 0$, which means that $p_{m,t}$ will only be significant larger than zero for $m \ll t$, and exponentially suppressed anywhere else. By expanding even further for $v \ll 1$, we find

$$\varphi(k^*) = -v^2 + \mathcal{O}\left(v^4\right) \qquad \text{and} \qquad \frac{1}{\sqrt{|\varphi''(k^*)|}} = \sqrt{2} + \mathcal{O}\left(v^2\right) ,$$

and finally recover the familiar form

$$p_{m,t} \approx \frac{1}{\sqrt{\pi t}} \, \mathrm{e}^{-\frac{m^2}{t}} . \tag{4.12}$$

This formula has two important implications. First, by comparing this to equation (2.2), we can deduce $d_w = 2$ and $d_f = 1$. This is also true for the unbiased random walk without the possibility to remain at a site, which leads to the second point: for random walks the introduction of hops that remain at a node, corresponds to a rescaling of time. Note that $t \to 2t$ leads to the familiar solution of the *standard* random walk. As we will see in the following section, this is not necessarily true for quantum walks.

By the nature of the Fourier transform, this approach is limited to geometries that are translational invariant (e.g., hypercubic latices) or possess special symmetries (e.g., the hypercube). For quantum walks, we can follow a similar procedure with more technical hurdles, but conceptually the same.

4.2 The three-state one dimensional quantum walk

The one-dimensional quantum walk with the three-dimensional Grover coin was previously studied by Inui *et al.* [36]. In this variation of the walk on the line, the walker can remain on the site during a time step, which leads to a major difference compared to the usual description with a two dimensional coin: there is a finite probability to find the quantum walk very close to the initial site even after long times. This is called localization and was previously found on the square lattice [35]. In fact, this model is the simplest model exhibiting localization, a distinctly quantum effect entirely absent in the corresponding classical random walks, as we have seen in section 4.1. A thorough understanding of localization in this simple context becomes particularly relevant in light of the fact that this phenomenon is commonplace in higher-dimensional systems [58]. Furthermore, in systems without translational invariance, for instance, localization might be asymptotically complete and broadly distributed as we argue in section 4.3.

Here we calculate analytic expressions for the localization, find the so called weak limit[29] of the probability density function which is a smooth approximation to the rugged, actual one. Additionally, in [25], we have studied the convergence towards this smooth description, and compare our analytic predictions with numerical simulations. Here we focus more on the localization. In the end, we will give an intuitive argument why this localization occurs, give a sufficient criterion for it, and show that localization is actually fragile and uncommon for general coins.

4.2.1 Long time approximation

The time evolution for this variant is

$$|\psi_{m,t+1}\rangle = \mathbf{A}|\psi_{m-1,t}\rangle + \mathbf{B}|\psi_{m+1,t}\rangle + \mathbf{M}|\psi_{n,t}\rangle, \tag{4.13}$$

Our convention for the shift operation is the following: the first component is moved to the left, the third component to the right, while the second one remains on the site. The hopping matrices are therefore given by

$$\mathbf{A} = \begin{bmatrix} 0 & 0 & 0 \\ 0 & 0 & 0 \\ 0 & 0 & 1 \end{bmatrix} \cdot \mathcal{C}_G \,, \qquad \mathbf{B} = \begin{bmatrix} 1 & 0 & 0 \\ 0 & 0 & 0 \\ 0 & 0 & 0 \end{bmatrix} \cdot \mathcal{C}_G \,, \qquad \mathbf{M} = \begin{bmatrix} 0 & 0 & 0 \\ 0 & 1 & 0 \\ 0 & 0 & 0 \end{bmatrix} \cdot \mathcal{C}_G \,. \tag{4.14}$$

For simplicity, we assume again initial conditions only on site $m = 0$, i.e.,

$$|\psi_{m,0}\rangle = \delta_{m,0} \cdot |\psi_{0,0}\rangle \,. \tag{4.15}$$

Analogous to the random walk, we apply the Fourier transform to equation (4.13). From here on, a tilde indicates quantities with a k-dependence, which we will not explicitly show.

$$|\tilde{\psi}_{t+1}\rangle = \underbrace{\frac{1}{3} \begin{bmatrix} -\kappa & 2\kappa & 2\kappa \\ 2 & -1 & 2 \\ 2\kappa^{-1} & 2\kappa^{-1} & -\kappa^{-1} \end{bmatrix}}_{:=\tilde{\mathbf{C}}} \cdot |\tilde{\psi}_t\rangle \,, \tag{4.16}$$

where $\kappa = \mathrm{e}^{\mathrm{i} \cdot k}$. Because of the internal degrees of freedom, this is still a matrix equation. Its solution

$$|\tilde{\psi}_t\rangle = \tilde{\mathbf{C}}^t \cdot |\psi_{0,0}\rangle \tag{4.17}$$

can be found by computing the eigenvalue decomposition

$$\mathbf{T}^{-1} \cdot \tilde{\mathbf{C}} \cdot \mathbf{T} = \begin{bmatrix} \tilde{\lambda}_1 & 0 & 0 \\ 0 & \tilde{\lambda}_2 & 0 \\ 0 & 0 & \tilde{\lambda}_3 \end{bmatrix} . \tag{4.18}$$

One eigenvalue is purely real, $\tilde{\lambda}_1 = 1$, whereas the other two obey

$$\tilde{\lambda}_{2,3} = \mathrm{e}^{\pm \mathrm{i}\tilde{\omega}} \quad \text{, and} \quad \cos(\tilde{\omega}) = -\frac{2}{3} - \frac{\cos(k)}{3}\,. \tag{4.19}$$

The t^{th} power of $\tilde{\mathbf{C}}$ can then be expressed as

$$\tilde{\mathbf{C}}^t = \tilde{\mathbf{M}}_1 + \tilde{\lambda}_2^t \cdot \tilde{\mathbf{M}}_2 + \tilde{\lambda}_3^t \cdot \tilde{\mathbf{M}}_3\,. \tag{4.20}$$

Representations of $\mathbf{T}$ and the $\tilde{\mathbf{M}}$ matrices are too large to show here, but can easily be obtained with a computer algebra system, like Mathematica or Maple. In the end, the real space solution is obtained by performing the inverse Fourier transform

$$|\psi_{m,t}\rangle = \frac{1}{2\pi} \int_{-\pi}^{\pi} \mathrm{e}^{\mathrm{i}\cdot m\cdot k} \cdot |\tilde{\psi}_t\rangle \,\mathrm{d}k\,, \tag{4.21}$$

and the probability density function is found via (2.6). We now study the long time properties of equation (4.21).

The Stationary Distribution

One can see from equation (4.20) that a time-independent component of $|\tilde{\psi}^t\rangle$ can exist due to the constant eigenvalue of $\tilde{\mathbf{C}}$. The inverse Fourier transform of this part can be computed exactly by employing the residue theorem. Note that the corresponding integral for this part following from equations (4.20) and (4.21), in terms of κ reads

$$|\psi_{m,\infty}\rangle = \underbrace{\frac{1}{2\pi\mathrm{i}} \oint_{|\kappa|=1} \kappa^{m-1} \tilde{\mathbf{M}}_1 \,\mathrm{d}\kappa}_{:=\,\mathbf{U}_1(m)} \cdot |\psi_{0,0}\rangle\,. \tag{4.22}$$

To evaluate these integrals, we do not have to resort to any approximation, but can solve them analytically. Without showing $\tilde{\mathbf{M}}_1$ here explicitly, every element has the two poles

$$\kappa_\pm = -5 \pm 2\sqrt{6}, \tag{4.23}$$

of which only κ_+ lies inside the unit circle. Depending on m, there is an additional pole at $\kappa = 0$. After some simple algebra, we find

$$\mathbf{U}_1(m) = \kappa_+^m \begin{bmatrix} \frac{1}{\sqrt{6}} & 1-\sqrt{\frac{2}{3}} & 2-\frac{5}{\sqrt{6}} \\ -1-\sqrt{\frac{2}{3}} & -\sqrt{\frac{2}{3}} & 1-\sqrt{\frac{2}{3}} \\ -2-\frac{5}{\sqrt{6}} & -1-\sqrt{\frac{2}{3}} & \frac{1}{\sqrt{6}} \end{bmatrix} + \operatorname*{Res}_{\kappa=0}(\kappa^{m-1}\cdot\tilde{\mathbf{M}}_1) \tag{4.24}$$

The last term is only non-zero if $n \leq 0$ and counteracts the divergence of κ_+^m as $m \to -\infty$. All residues are of the form

$$\operatorname*{Res}_{\kappa=0}\left(\frac{a\kappa^p}{1+10\kappa+\kappa^2}\right),$$

for some integer power p. To calculate the residue, note that with partial fractions

$$\frac{1}{1+10\kappa+\kappa^2} = \frac{1}{4\sqrt{6}}\left[\frac{1}{\kappa_- - \kappa} - \frac{1}{\kappa_+ - \kappa}\right] = \frac{1}{4\sqrt{6}}\left[\sum_{k=0}^{\infty}\frac{\kappa^k}{\kappa_-^{k+1}} - \sum_{k=0}^{\infty}\frac{\kappa^k}{\kappa_+^{k+1}}\right].$$

With this representation, we find

$$\begin{aligned}
\operatorname*{Res}_{\kappa=0}\left(\frac{a\kappa^p}{1+10\kappa+\kappa^2}\right) &= \frac{a}{2\pi\mathrm{i}}\oint \kappa^p \frac{1}{1+10\kappa+\kappa^2}\,\mathrm{d}\kappa \\
&= \frac{a}{4\sqrt{6}}\sum_{k=0}^{\infty}\left(\kappa_-^{-k-1} - \kappa_+^{-k-1}\right)\cdot \underbrace{\frac{1}{2\pi\mathrm{i}}\oint \kappa^{p+k}\mathrm{d}\kappa}_{=\delta_{-1,p+k}} \\
&= \frac{a}{4\sqrt{6}}\left[\kappa_-^p - \kappa_+^p\right].
\end{aligned}$$

Plugging this result into equation (4.24), yields

$$\begin{aligned}
\mathbf{U}_1(m<0) &= \frac{\kappa_-^m}{\sqrt{6}}\begin{bmatrix} 1 & -2-\sqrt{6} & -5-2\sqrt{6} \\ -2+\sqrt{6} & -2 & -2-\sqrt{6} \\ -5+2\sqrt{6} & -2+\sqrt{6} & 1 \end{bmatrix} \\
\mathbf{U}_1(m=0) &= \frac{1}{\sqrt{6}}\begin{bmatrix} 1 & -2+\sqrt{6} & -5+2\sqrt{6} \\ -2+\sqrt{6} & -2+\sqrt{6} & -2+\sqrt{6} \\ -5+2\sqrt{6} & -2+\sqrt{6} & 1 \end{bmatrix} \\
\mathbf{U}_1(m>0) &= \frac{\kappa_+^m}{\sqrt{6}}\begin{bmatrix} 1 & -2+\sqrt{6} & -5+2\sqrt{6} \\ -2-\sqrt{6} & -2 & -2+\sqrt{6} \\ -5-2\sqrt{6} & -2-\sqrt{6} & 1 \end{bmatrix}
\end{aligned} \tag{4.25}$$

At first, the case distinction in the sign of m seems counterintuitive, but the comparison to the numerics in figure 4.1 reveals the possibility of an asymmetric localization around the initial site.

To obtain the stationary probability density function, we calculate

$$p_{m,\infty} = \langle \psi_{m,\infty} | \psi_{m,\infty} \rangle = \langle \psi_{0,0} | U_1^\dagger(m) U_1(m) | \psi_{0,0} \rangle \,. \tag{4.26}$$

We want to point out that the stationary probability density function always decays exponentially away from the initial site as $p_{m,\infty} \sim \kappa_+^{2|m|}$ independent of the initial conditions, even though the proportionality constant might differ for positive and negative m. The initial conditions $|\psi_{0,0}\rangle \propto (1,-2,1)$ is a non-generic case where the localization *completely vanishes*. There exists also a whole family,$|\psi_{0,0}\rangle \propto (-a \cdot (1+\kappa_\pm)/2 - b \cdot \kappa_\pm, a, b)$ with $a, b \in \mathbb{R}$, where the localization vanishes for positive (negative) m while still exponentially decaying for negative (positive) values. This effect cannot be seen in the classical random walk without introducing disorder in form of, e.g., position dependent hopping probabilities [33].

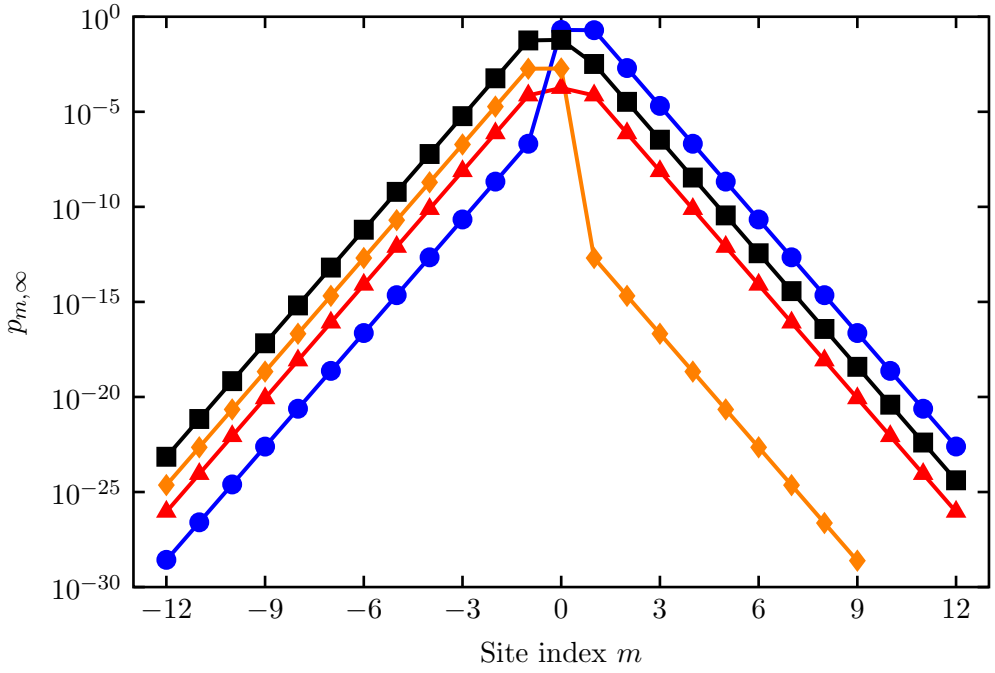

Figure 4.1: Comparison between analytic prediction (lines) and numerical simulation after $T = 2^{20}$ time steps (symbols) for the localization around $n = 0$. The initial conditions are $|\psi_{0,0}\rangle \propto (1, -1.9, 1)$ (red triangles), $|\psi_{0,0}\rangle \propto (10, 0, 1)$ (blue circles), $|\psi_{0,0}\rangle \propto (1, -3, 2 + \mathrm{i})$ (black squares), and $|\psi_{0,0}\rangle \propto (410, -800, 499)$ (orange diamonds). They have been chosen to show the possible asymmetry of $p_{m,\infty}$ [25]

To show that our calculations describe the localized part comprehensively, we compare to a long simulation of a system, where the system is large enough that the finite size has no influence on the probabilities near the initial site at the end of the simulation. The system starts with different initial conditions and evolves for 2^{20} time steps. In the end, the final probabilities at sites around the origin are recorded. Figure 4.1 shows the comparison between evaluating equation (4.26) and the simulation. To demonstrate the asymmetry, we choose 4 particular initial conditions.

The rapid decay renders estimating $p_1(m)$ using simulations for $|m| \gg 10$ difficult. The values range over 30 orders of magnitude, challenging the machine precision used in the simulations. Furthermore, the time to converge to $p_1(m)$ grows exponentially with m [25]. The case of zero localization for either $m > 0$ or $m < 0$ is also hard to resolve numerically due to the limited machine precision, but the blue and orange curves in figure 4.1 demonstrate the asymmetry, and the jump at $m = 0$ can be arbitrarily steep.

Approximating the Time-Dependent Integrals

To show that the part not covered by the calculations above still spreads ballistically, we approximate the remaining integrals with exactly the same method we used in section 4.1.

After solving the time independent part analytically, we have to resort to approximations for the time dependent part of $|\tilde{\psi}^t\rangle$ in the limit $t \to \infty$. In analogy to Eq. (4.22), we define

$$\mathbf{U}_{2,3}(t,n) = \frac{1}{2\pi} \int_{-\pi}^{\pi} \mathrm{e}^{\mathrm{i}\cdot k\cdot n} \tilde{\mathbf{M}}_{2,3} \cdot \tilde{\lambda}_{2,3}^{t} \, \mathrm{d}k \,, \tag{4.27}$$

such that the sum $\mathbf{U}_1 + \mathbf{U}_2 + \mathbf{U}_3 = \tilde{\mathbf{C}}^t$ expresses the full time evolution. By using the equations (4.6) and (4.19), we write the integrals as

$$\frac{1}{2\pi} \int_{-\pi}^{\pi} \tilde{f}(k) \cdot \mathrm{e}^{\mathrm{i}t\cdot(vk \pm \tilde{\omega})} \, \mathrm{d}k \,.$$

where the function $\tilde{f}$ represents the different (slowly-varying) elements of the $\tilde{\mathbf{M}}$ matrices. The integrals can be approximated similarly to equation (4.12) using again the method of steepest descent. The only difference is an additional rotation of the path of integration as the second derivative of the exponent at the saddle point is not negative. A more detailed discussion can be found in [10].

In this approximation, $\tilde{\mathbf{C}}^t$ will contain the constant terms from $\mathbf{U}_1$ and terms proportional to $t^{-1/2}$ that further oscillate both in space and in time. In their full extent, these terms are too complex to write down here, but are easily used to compute numerical values for specific initial conditions. Despite the potential to describe the full probability density function very well for sufficiently large times, one can find a smooth approximation, called weak limit [29] that averages the spatial-temporal oscillations out.

Following Ambainis *et al.* [6], we can separate out the rapidly oscillating part of equation (4.20). If we ignore the localized part for a moment, the corresponding distribution, which we will call $p_{avg}(n,t)$, can be found via

$$p_{m,t}^{avg} = \langle\psi_{0,0}| \left(\mathbf{U}_2^\dagger \cdot \mathbf{U}_2 + \mathbf{U}_3^\dagger \cdot \mathbf{U}_3\right) |\psi_{0,0}\rangle \tag{4.28}$$

This expression seems ad hoc, but contains all non-oscillating terms from the full approximation. This corresponds to a temporal average at a specific site, assuming that the rapidly oscillating phase factors lead to a negligible contribution to the inverse Fourier transform (according to Riemann-Lebesgue). We argue that this also corresponds to a local spatial average at fixed t, because as $t \to \infty$ a small change in n will only lead to a small change in v, such that the non-oscillating contribution should be the same in a neighborhood around a point that is reasonably small compared to t. This average also smoothes out the spatial oscillations of the PDF. In fact, we can use a spatial average to numerically predict p_{avg}.

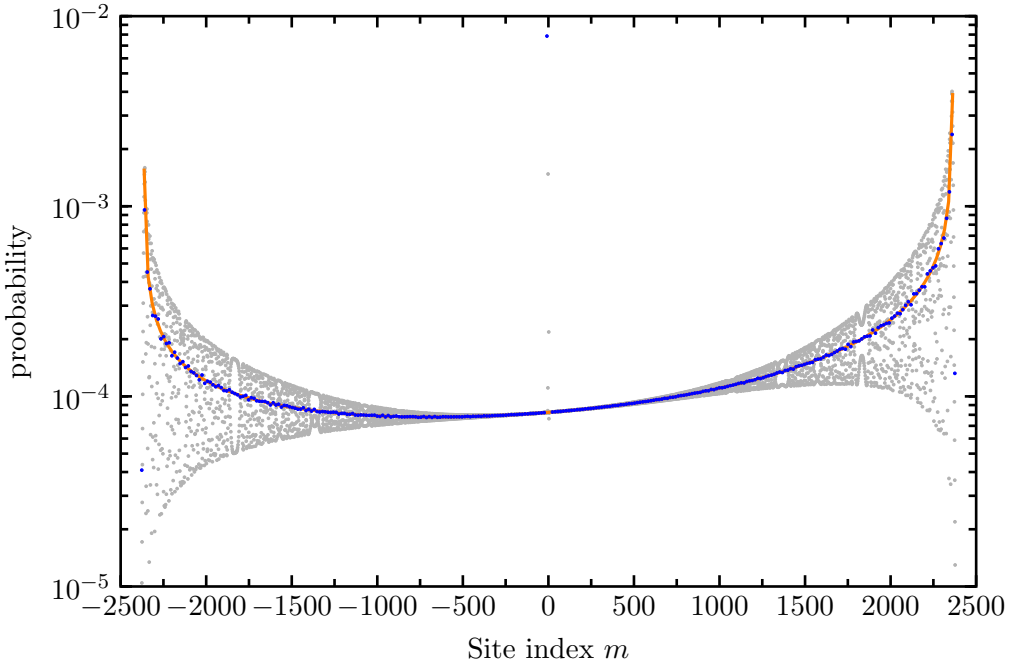

Figure 4.2: The smooth approximation p_{avg} from equation (4.28) (orange line) and the spatial average over 16 sites (blue dots) after 4096 time steps. The initial conditions are $|\psi_0^0\rangle \propto (0, \mathrm{i}, 1)$. They gray dots represent the numerical values for the probabilities. The localized part is not described by p_{avg}, but it is included in the spatial average producing the blue dot at $m = 0$ with the highest probability. [25].

Inserting the expressions for $\mathbf{U}_{2,3}(n,t)$, we find the matrix

$$\mathbf{U}_2^\dagger \cdot \mathbf{U}_2 + \mathbf{U}_3^\dagger \cdot \mathbf{U}_3 = \frac{1}{\pi t\sqrt{2(1-3v^2)}\,(1-v^2)} \cdot \begin{bmatrix} (1-v)^2 & 2v(1-v) & 1-5v^2 \\ 2v(1-v) & 2-2v^2 & -2v(1+v) \\ 1-5v^2 & -2v(1+v) & (1+v)^2 \end{bmatrix} \tag{4.29}$$

valid for all m subjected to $|m|/t < 1/\sqrt{3}$. Outside this interval, $p_{avg}(m,t) \equiv 0$. The dependency on m is implicit through $v = m/t$. For a specific initial condition, a comparison between the numerical simulation and the analytic prediction can be found in figure 4.2.

Note that $p_{m,t}^{avg}/t$ only depends on v which corresponds to the scaling function f in

equation (2.2). Our definition of this averaged probability closely relates to the weak limit proven by Grimmett *et al.* [29]. In their work they show that quantum walks on a regular lattice generically[2] exhibit this convergence with $d_w = 1$.

To show that $p_{m,t}^{avg}$ is a proper probability density function, let us look at the sum of the contributions from all m. In the long-time limit, we can treat $v = m/t$ as a continuous variable. Hence, we approximate probabilities

$$p(m_- \leq m \leq m_+, t) \approx \sum_{m=m_-}^{m_+} p_{m,t}^{avg}$$

by integrals of the form

$$p(a \ \leq v \leq b, t) \approx \int_a^b p_t^{avg}(v \cdot t) \cdot t \, \mathrm{d}v \, .$$

Here $a = m_-/t$ and $b = m_+/t$. By using the convergence of $p_t^{avg}(v \cdot t) \cdot t$ to a stationary distribution solely depending on v, we conclude that the spreading is always ballistic. In this continuous limit, the localized part remains concentrated around the initial site, and

$$p_1(v \cdot t) \cdot t \to \langle \psi_{0,0} | \begin{pmatrix} \frac{1}{\sqrt{6}} & 1 - \sqrt{\frac{2}{3}} & 2 - \frac{5}{\sqrt{6}} \\ 1 - \sqrt{\frac{2}{3}} & 1 - \sqrt{\frac{2}{3}} & 1 - \sqrt{\frac{2}{3}} \\ 2 - \frac{5}{\sqrt{6}} & 1 - \sqrt{\frac{2}{3}} & \frac{1}{\sqrt{6}} \end{pmatrix} | \psi_{0,0} \rangle \, \delta(v) \tag{4.30}$$

characterizing the localization within the weak limit. Some algebra reveals that

$$\sum_{m=-\infty}^{\infty} p_1(m) + \int_{-1/\sqrt{3}}^{1/\sqrt{3}} p_{avg}(v \cdot t, t) \cdot t \ \mathrm{d}v = 1 \, , \tag{4.31}$$

i.e., our approximation actually yields a true probability density function.

As an example, we utilize $p_{m,t}^{avg}$ to approximate the first three moments of the quantum

[2]Their proof uses the same methods applied here. They show that it always leads to the same scaling as long as the eigenvalues of the coin are not all equal, which leads to trivial behavior again.

walk, $\langle m^k \rangle$ for $k = 0, 1, 2$, assuming it is always a good approximation, and the localized part does not contribute to the time dependence of any moment.

$$\langle f(m) \rangle_t = \sum_{m=-\infty}^{\infty} f(m) p(m,t) \approx \int_{-1/\sqrt{3}}^{1/\sqrt{3}} f(v \cdot t) p_{avg}(v \cdot t, t) \cdot t \, \mathrm{d}v$$

Applying this to every matrix entry in equation (4.29) yields:

$$\langle m^0 \rangle = \frac{1}{\sqrt{6}} \langle \psi_{0,0} | \begin{bmatrix} -1+\sqrt{6} & 2-\sqrt{6} & 5-2\sqrt{6} \\ 2-\sqrt{6} & 2 & 2-\sqrt{6} \\ 5-2\sqrt{6} & 2-\sqrt{6} & -1+\sqrt{6} \end{bmatrix} | \psi_{0,0} \rangle \tag{4.32}$$

$$\langle m^1 \rangle_t = \frac{t}{\sqrt{6}} \langle \psi_{0,0} | \begin{bmatrix} 2-\sqrt{6} & -2+\sqrt{6} & 0 \\ -2+\sqrt{6} & 0 & 2-\sqrt{6} \\ 0 & 2-\sqrt{6} & -2+\sqrt{6} \end{bmatrix} | \psi_{0,0} \rangle \tag{4.33}$$

$$\langle m^2 \rangle_t = \frac{t^2}{6\sqrt{6}} \langle \psi_{0,0} | \begin{bmatrix} -13+6\sqrt{6} & 14-6\sqrt{6} & 29-12\sqrt{6} \\ 14-6\sqrt{6} & 2 & 14-6\sqrt{6} \\ 29-12\sqrt{6} & 14-6\sqrt{6} & -13+6\sqrt{6} \end{bmatrix} | \psi_{0,0} \rangle \tag{4.34}$$

We observe that the zeros moment is unity only for the initial conditions that show no localization, $\langle \psi_{0,0} | \propto (1, -2, 1)^T$. The matrix for the first moment has the eigenvector $(1, 1, 1)^T$ with eigenvalue 0. However, this does not cover all symmetric initial conditions that will yield a zero first moment by symmetry. It easily verified that the initial conditions $\sim (1, 0, 1)^T$ also yield a zero first moment. Hence, every linear combination of those two will do so, too, which now covers all symmetric initial conditions. These asymptotic formulas show that any non-zero first moment grows linearly in time while the second moment is proportional to t^2.

Figure 4.3 shows a comparison between the approximation and numerical simulations. The main result is that the second moment always grows $\sim t^2$ regardless of the initial conditions, see equation (4.34). This means, only the shape of the probability density

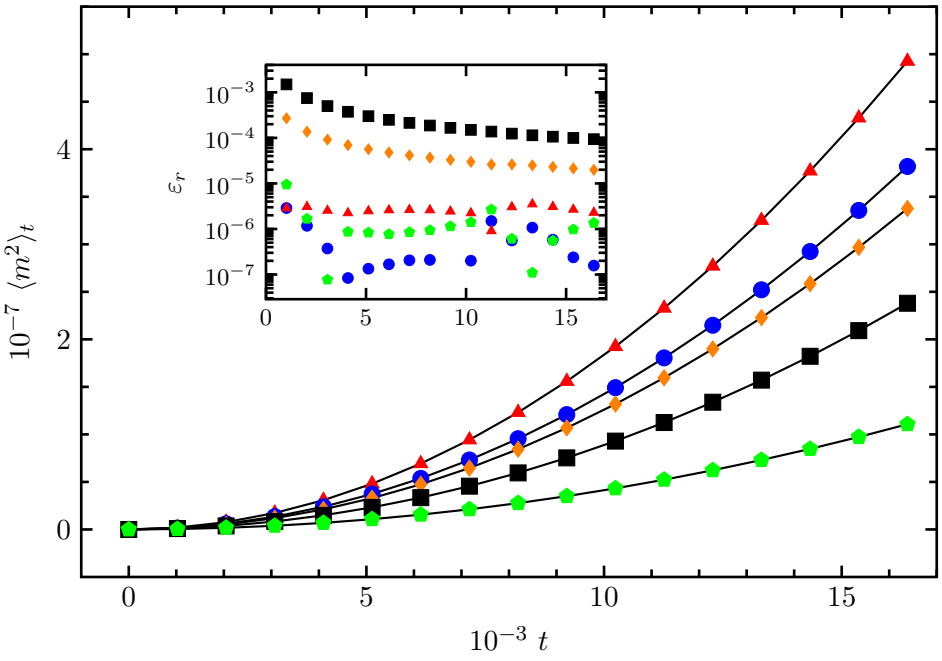

Figure 4.3: Comparison between the numerical values (symbols) and the evaluation of equation (4.34) for the second moment $\langle m^2\rangle$. The inset shows the relative difference ε_r between the two values [25].

function can be influenced by $|\psi_{0,0}\rangle$, but not the asymptotic scaling of its spread.

4.2.2 Intuitive explanation for the localization

The fact that quantum walks can exhibit localization without any disorder is counterintuitive, and this phenomenon cannot be found in a comparable situation for the random walk. After all, the equations are translational invariant, so how can the walker *get stuck*? The important realization here is the initial conditions break the invariance. But the question now is, whether this effect crucially depends on the coin or not.

There have been some studies about the localization effects in quantum walks in one [36, 41, 4] and two [35] dimensions. Especially Štefaňák *et al.* [72] find whole families of coins for the three state quantum walk on the line that show localization, and so they draw the conclusion that localization must be a general feature. We will argue that this is actually not the case, and for a majority of the coins localization effects are not present.

While we used the Fourier transform to describe the system in a very compact manner, and we found localization because of a constant eigenvalue of the Fourier transformed coin operator (see equation (4.16) for its definition), we find a criterion from the real-space description. We start from the assumption that the localization is the result of just two adjacent nodes interacting with each other, but not with their other neighbors. If this is true, then the linear system[3]

$$\begin{aligned} \mathrm{e}^{\mathrm{i}\varphi} \cdot |\psi_m\rangle &= \mathbf{B} \cdot |\psi_{m+1}\rangle + \mathbf{M} \cdot |\psi_m\rangle \qquad & \mathbf{B} \cdot |\psi_m\rangle &= 0 \\ \mathrm{e}^{\mathrm{i}\varphi} \cdot |\psi_{m+1}\rangle &= \mathbf{A} \cdot |\psi_m\rangle + \mathbf{M} \cdot |\psi_{m+1}\rangle \qquad & \mathbf{A} \cdot |\psi_{m+1}\rangle &= 0 \end{aligned} \tag{4.35}$$

should have a non-trivial solution for some real value of φ. For our convention which component moves where, we can also impose

$$|\psi_m\rangle = \begin{pmatrix} a \\ b \\ 0 \end{pmatrix} \qquad \text{and} \qquad |\psi_{m+1}\rangle = \begin{pmatrix} 0 \\ c \\ d \end{pmatrix} . \tag{4.36}$$

The linear system directly transfers to any dimension of the coin space, whereas the ansatz for the two wave vectors needs to be adjusted for the given circumstances.

This criterion can be formulated as the determinant of a matrix composed solely from the elements of any particular coin one wishes to study. If this determinant is zero, the quantum walk shows localization for some initial conditions[4]. In fact, the non-trivial solution of (4.35) enables us to determine which initial conditions show no localization. If one can find a $|\psi_{0,0}\rangle$ that is orthogonal to both $|\psi_m\rangle$ and $|\psi_{m+1}\rangle$, these initial conditions would show no localization whatsoever.

Let us illustrate the method for the Grover coin, where we know the answer from section

[3] We dropped the subscript t here, because we are looking for a time independent solution.
[4] We already saw for the Grover coin that special initial conditions can show no localization, but it was not generically true

4.2.1. With the hopping matrices from equation (4.14), it is straightforward to show that

$$|\psi_m\rangle \propto \begin{pmatrix} 1 \\ 2 \\ 0 \end{pmatrix} \qquad \text{and} \qquad |\psi_{m+1}\rangle \propto \begin{pmatrix} 0 \\ 2 \\ 1 \end{pmatrix} \tag{4.37}$$

satisfies all the equations and is up to normalization actually an eigenvector of the time evolution operator for all m. This is another way of looking at localization as eigenstates of $\mathcal{U}$ with only a finite number of non-zero components. Our ansatz already assumes that only four components are neccessary. As a confirmation that our approach works, we can confirm that the initial conditions $|\psi_{0,0}\rangle \propto (1, -2, 1)^T$ are orthogonal to both $|\psi_m\rangle$ and $|\psi_{m+1}\rangle$.

To answer the question whether a solution can be found generically, let us count the number of equations in (4.35). Each hopping matrix has only one non-zero row, so that the system contains six non-trivial equations, but the number of unknowns in our ansatz is only four! This brings us to the conclusion that localization cannot be a generic feature, but is rather the consequence of the special structure of the Grover coin.

But why do Štefaňák *et al.* find a whole family of coins that show localization? To understand this, we can look at a whole family of coins, defined by

$$\mathcal{C}_{HH} = 2 \cdot |v\rangle\langle v| - \mathbb{1} \qquad \text{with} \quad |v\rangle = (\cos\alpha \sin\beta, \sin\alpha \sin\beta, \cos\beta)^T . \tag{4.38}$$

The subscript stands for Housholder and refers to the well-known transformations from linear algebra[5]. They represent reflections around a certain axis in $\mathbb{R}^3$. For $\alpha = \pi/4$ and $\beta = \arctan\left(\sqrt{2}\right)$, C_G is obtained.

By solving using this parametrization, we can show that equation (4.35) has a non-trivial

[5]In fact, our family is the negative of a Housholder transformation, but this overall phase factor does not affect any observables. Our definition was chosen to contain the Grover coin.

solution, if

$$\cos(2\beta) = \frac{2\cos^2\alpha}{-3+\cos(2\alpha)}\,. \tag{4.39}$$

Note, this condition states that with the whole two dimensional parameter space only a set of measure zero shows localization.

The two families of coins studied in [72] are

$$\begin{aligned}
\mathcal{C}_1(\varphi) &= \frac{1}{6}\begin{bmatrix} -1-\mathrm{e}^{2\mathrm{i}\varphi} & 2+2\mathrm{e}^{2\mathrm{i}\varphi} & 5-\mathrm{e}^{2\mathrm{i}\varphi} \\ 2+2\mathrm{e}^{2\mathrm{i}\varphi} & 2-4\mathrm{e}^{2\mathrm{i}\varphi} & 2+2\mathrm{e}^{2\mathrm{i}\varphi} \\ 5-\mathrm{e}^{2\mathrm{i}\varphi} & 2+2\mathrm{e}^{2\mathrm{i}\varphi} & -1-\mathrm{e}^{2\mathrm{i}\varphi} \end{bmatrix}, \text{ and} \\
\mathcal{C}_2(\rho) &= \begin{bmatrix} -\rho^2 & \rho\sqrt{2-2\rho^2} & 1-\rho^2 \\ \rho\sqrt{2-2\rho^2} & 2\rho^2-1 & \rho\sqrt{2-2\rho^2} \\ 1-\rho^2 & \rho\sqrt{2-2\rho^2} & -\rho^2 \end{bmatrix}.
\end{aligned} \tag{4.40}$$

They are constructed by manipulating one eigenvalue for $\mathcal{C}_1$ and two eigenvectors for $\mathcal{C}_2$ in the eigenvalue decomposition of $\mathcal{C}_G$. They call it a continuous deformation of the Grover coin.

While our parametrization does not contain $\mathcal{C}_1$, the second one is reproduced by $\alpha = \arccos\left(\frac{\sqrt{2}\rho}{\sqrt{1+\rho^2}}\right)$ and $\beta = \arccos(-\rho^2)/2$. This parametrization obeys equation (4.39) which is why they find localization.

Additionally to these analytic results, we also generated random unitary matrices [75] and checked whether condition (4.35) was fulfilled within numerical accuracy. We did not find a single coin out of one million trials using 50 digits accuracy. We thus conclude that localization only occurs for very special families of coins and should not be considered a generic feature of three-state, one dimensional quantum walks.

Our method could be applied to higher dimensional, regular lattices. One would only have to identify the minimum number of sites, and the corresponding ansatz in each case, but the idea would still be that sparse eigenvectors with only a few non-zero entries exsist. This could be used to inverstigate the localization on the square lattice [58].

4.3 Localization on the Dual Sierpinsky Gasket

We now try to set the localization found in one dimensional quantum walks in relation to the effects we see on the Dual Sierpinski Gasket (DSG). We already studied the different coins on this fractal in chapter 3, where we noticed some signs for localization. With long time simulations, we try to gain some insights into the nature of this phenomenon on this network, which is know to lead to very strong localization for the continuous time quantum walk [19].

The nature of these simulations is different from the ones in chapter 3 as we are here interested in the properties of the non-moving parts of the walk rather than the out moving front. For this reason, the simulations have to run far longer, beyond the size of the system. To adjust to this requirement, we modify the graph slightly at the boundaries, see figure 4.4. We connect the two nodes at the base, where the initial conditions are placed either symmetrically or asymmetrically. The node at the top is connected to an absorbing site, where the walk can enter, but not escape. This will breaks the unitarity of the time evolution and gives the quantum walk the chance to converge. Important is that it can absorb the spreading part while (hopefully) not interfering with the localization around the initial conditions. The absorption as a function of time is simulated.

The simulations were performed with a parallel C++ program using MPI. The program was specifically developed for this kind of simulations with large graphs and local observables allowing for parallelism. We simulated different system sizes of generation $4, 5, \ldots 12$ ($N \lesssim 1.6 \cdot 10^6$) for up to 2^{28} time steps to ensure that *most* of the absorption already occurred. At this point the numerical inaccuracy was comparable to what was absorbed over a certain period of time. Due to the smaller system size we were able to run these simulations on our cluster computer, which is why these simulations are, counting the total number of multiplications, significant larger than the one in chapter 3.

The simulations show the same behavior for all initial conditions: the total absorption

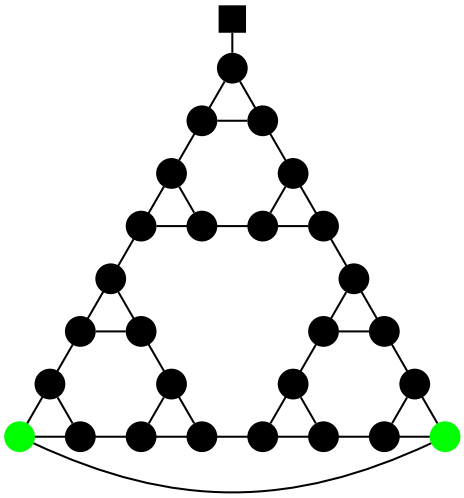

Figure 4.4: The modified graph used to study the localization of the quantum walk using the Grover coin on the DSG. The initial conditions reside on the green nodes, and the square represents an absorbing boundary. We only show a simplified graph. The different types of edges are still present.

F_0 tends to zero as the system size grows. More specifically, we observe

$$F_0(k) \simeq c \cdot L_k^{-\alpha} \tag{4.41}$$

for some exponent α and a constant c that depends on the initial conditions. One way of extracting the exponent from the data is to write the scaling in the form

$$-\frac{\log\left(F_0(k)\right)}{\log\left(L_k\right)} \simeq \alpha - \frac{c}{\log\left(L_k\right)}\,. \tag{4.42}$$

This rewrite justifies the plot in figure 4.5. The left hand site is the y axis, and $1/\log(L_k)$ is the x variable. In this plot, the scaling should be a straight line for $x \to 0$ (meaning $L_k \to \infty$), and the exponent α will be the intersection at $x = 0$. As we can see from the figure, all different initial conditions seem to accumulate around the same value of $\alpha = 1.23(1)$ which we estimate by using the most linear extrapolation found.

The curvature of most of the data shows that the system sizes simulated are not big enough to conclusively distinguish between one universal exponent independent of the

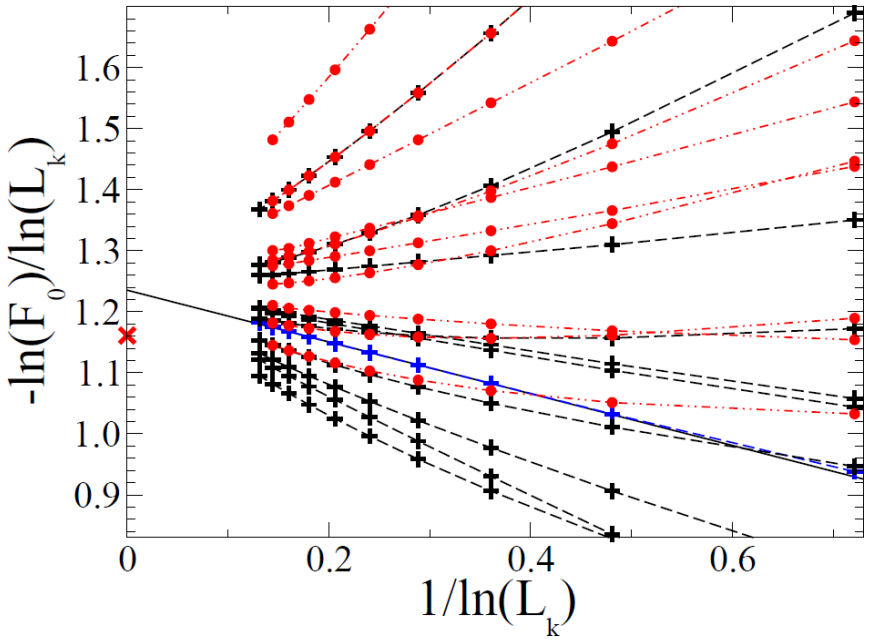

Figure 4.5: Extrapolation for the scaling exponent in the decay of the simulated absorption F_0 with system Length $L_k = 2^k$, $k \leq 12$, based on a power-law, for many different symmetric (+) and asymmetric (•) initial conditions. All data appears to extrapolate to the same intercept ($L_k \to \infty$) at about 1.23(1), with the most linear fit (extended line) provided by the symmetric initial conditions $\propto (1, 2, 1)$. This exponent is closely bounded below by $d_w = \log_2(\sqrt{5})$ (×) [13].

initial conditions or a (continuous or discrete) spectrum of exponents. At point we can only speculate, and bound its value to be $d_w \leq \alpha \leq d_w + 2\beta$ with $\beta = 0.424(3)$ from the two different scaling collapses in figure 3.15. To definitely solve this, we need a better understanding of the renormalization group approach developed here. At this point, we do not know how to extract this quantity from the recursion equations.

5 Conclusions

> I may not have gone where I intended to go, but I think I have ended up where I needed to be.
>
> Douglas Adams, *The Long Dark Tea-Time of the Soul*

In this thesis, we have studied the discrete time quantum walks on four self-similar networks using the renormalization group and large scale numerical simulations. We found that the postulated scaling relation even holds for quantum walks, and collected evidence to conjecture a remarkable relationship between the walk dimensions of the generic random walk and the quantum walk using the Grover coin. We discovered a strong influence of both the coin and the underlying geometry on the long term asymptotic spreading and localization effects.

This work represents a first step towards a better understanding of the rich phenomenology found in quantum walks beyond regular lattices. We started this work with the ambitious goal of categorizing possible behaviors, and identifying universality classes, i.e., families of coins that all are asymptotically similar. And in some sense, we succeeded. We showed how the Grover coin always seems to spread quadratically faster than the random walk. The Fourier coin appears to be always slower than the Grover coin. We even constructed a coin that spreads ballistically on some networks, which has never been observed before.

On the other hand, we also discovered several phenomena we do not fully understand,

and still have open questions: Can we always construct a coin spreading with $d_w = 1$ for any network? Is localization on some (self-similar) network generically present, like our findings on the DSG suggest, or are there always coins that will spread through the whole network without getting completely immobilized, or moving deterministically? The answers to these questions could have a huge impact on the applicability of quantum algorithms to certain problems.

While the above questions concern the nature of quantum walks and deserve future attention, we also have an incomplete picture of the renormalization group grounded in technical hurdles as well as conceptual problems. Those might seem less relevant for the quantum computing aspects, but are another incarnation of the longstanding problem of applying the renormalization group to certain quantum mechanical problems.

Bibliography

[1] E. Agliari, A. Blumen, and O. Mülken. Quantum-walk approach to searching on fractal structures. *Physical Review A*, 82:012305+, July 2010.

[2] Dorit Aharonov, Andris Ambainis, Julia Kempe, and Umesh Vazirani. Quantum walks on graphs. In *ACM Symposium on Theory of Computation (STOC'01)*, pages 50–59, July 2001.

[3] Y. Aharonov, L. Davidovich, and N. Zagury. Quantum random walks. *Physical Review A*, 48(2):1687–1690, August 1993.

[4] Andre Ahlbrecht, Christopher Cedzich, Robert Matjeschk, VolkherB Scholz, AlbertH Werner, and ReinhardF Werner. Asymptotic behavior of quantum walks with spatio-temporal coin fluctuations. *Quantum Information Processing*, 11(5):1219–1249, March 2012.

[5] Andre Ahlbrecht, Volkher B. Scholz, and Albert H. Werner. Disordered quantum walks in one lattice dimension. *Journal of Mathematical Physics*, 52(10):102201+, October 2011.

[6] Andris Ambainis, Eric Bach, Ashwin Nayak, Ashvin Vishwanath, and John Watrous. One-dimensional quantum walks. In *Proceedings of the thirty-third annual ACM symposium on Theory of computing*, STOC '01, pages 37–49, New York, NY, USA, 2001. ACM.

[7] Clement Ampadu. Limit theorems for quantum walks associated with hadamard matrices. *Physical Review A*, 84(1), July 2011.

[8] Alán Aspuru-Guzik and Philip Walther. Photonic quantum simulators. *Nature Physics*, 8(4):285–291, April 2012.

[9] Eric Bach, Susan Coppersmith, Marcel P. Goldschen, Robert Joynt, and John Watrous. One-dimensional quantum walks with absorbing boundaries. *Journal of Computer and System Sciences*, 69(4):562–592, December 2004.

[10] Carl M. Bender. *Advanced mathematical methods for scientists and engineers I : asymptotic methods and perturbation theory*. Springer, 1999 edition, December 1999.

[11] A N Berker and S Ostlund. Renormalisation-group calculations of finite systems: order parameter and specific heat for epitaxial ordering. *Journal of Physics C: Solid State Physics*, 12(22):4961–4975, 1979.

[12] S. Boettcher and B. Goncalves. Anomalous diffusion on the Hanoi networks. *Europhysics Letters*, 84:30002, 2008.

[13] Stefan Boettcher, Stefan Falkner, and Renato Portugal. Renormalization and scaling in quantum walks. *Physical Review A*, 90(3), September 2014.

[14] Andrew Childs. Universal computation by quantum walk. *Physical Review Letters*, 102(18):180501+, May 2009.

[15] Andrew M. Childs. On the relationship between continuous- and discrete-time quantum walk. *Communications in Mathematical Physics*, 294(2):581–603, October 2010.

[16] Andrew M. Childs, Edward Farhi, and Sam Gutmann. An example of the difference between quantum and classical random walks. *Quantum Information Processing*, 1(1/2):35–43, March 2001.

[17] Andrew M. Childs and Yimin Ge. Spatial search by continuous-time quantum walks on crystal lattices. *Physical Review A*, 89(5), May 2014.

[18] A. Crespi, R. Osellame, R. Ramponi, V. Giovannetti, R. Fazio, L. Sansoni, F. De Nicola, F. Sciarrino, and P. Mataloni. Anderson localization of entangled photons in an integrated quantum walk. *Nature Photonics*, 7:322, 2013.

[19] Zoltán Darázs, Anastasiia Anishchenko, Tamás Kiss, Alexander Blumen, and Oliver Mülken. Transport properties of continuous-time quantum walks on sierpinski fractals. *Physical Review E*, 90(3), September 2014.

[20] D. Deutsch. Quantum theory, the church-turing principle and the universal quantum computer. *Proceedings of the Royal Society of London. A. Mathematical and Physical Sciences*, 400(1818):97–117, July 1985.

[21] David Deutsch and Richard Jozsa. Rapid solution of problems by quantum computation. *Proceedings of the Royal Society of London. Series A: Mathematical and Physical Sciences*, 439(1907):553–558, December 1992.

[22] C. Di Franco, M. Mc Gettrick, and Th Busch. Mimicking the probability distribution of a two-dimensional grover walk with a single-qubit coin. *Physical review letters*, 106(8), February 2011.

[23] C. Di Franco, M. Mc Gettrick, T. Machida, and Th Busch. Alternate two-dimensional quantum walk with a single-qubit coin. *Physical Review A*, 84(4), October 2011.

[24] Matthew Falk. Quantum search on the spatial grid. *arXiv:1303.4127*, March 2013.

[25] Stefan Falkner and Stefan Boettcher. Weak limit of the three-state quantum walk on the line. *Physical Review A*, 90(1), July 2014.

[26] Edward Farhi and Sam Gutmann. Quantum computation and decision trees. *Physical Review A*, 58(2):915–928, August 1998.

[27] Richard P. Feynman. Simulating physics with computers. *International journal of theoretical physics*, 21(6):467–488, 1982.

[28] David J. Griffiths. *Introduction to quantum mechanics*. Pearson Prentice Hall, 2nd edition, April 2005.

[29] Geoffrey Grimmett, Svante Janson, and Petra F. Scudo. Weak limits for quantum random walks. *Physical Review E*, 69:026119+, February 2004.

[30] Lov K. Grover. A fast quantum mechanical algorithm for database search. In *Proceedings of the Twenty-eighth Annual ACM Symposium on Theory of Computing*, STOC '96, pages 212–219, New York, NY, USA, 1996. ACM.

[31] Trevor Hastie. The elements of statistical learning : data mining, inference, and prediction. Hardcover, April 2009.

[32] S. Havlin and D. Ben-Avraham. Diffusion in disordered media. *Adv. Phys.*, 36:695–798, 1987.

[33] B. D. Hughes. *Random walks and random environments*, volume 2: Random Environments. Clarendon Press ; Oxford University Press, August 1995.

[34] B. D. Hughes. *Random walks and random environments*, volume 1: Random Walks. Clarendon Press ; Oxford University Press, March 1995.

[35] Norio Inui, Yoshinao Konishi, and Norio Konno. Localization of two-dimensional quantum walks. *Physical Review A*, 69:052323+, May 2004.

[36] Norio Inui and Norio Konno. Localization of multi-state quantum walk in one dimension. *Physica A: Statistical Mechanics and its Applications*, 353:133–144, August 2005.

[37] Norio Inui, Norio Konno, and Etsuo Segawa. One-dimensional three-state quantum walk. *Physical Review E*, 72:056112+, November 2005.

[38] Walter G. Kelley. *Difference equations : an introduction with applications*. Academic Press, 1991.

[39] Viv Kendon and Ben Tregenna. Decoherence in a quantum walk on a line. In Jeffrey H. Shapiro and Osamu Hirota, editors, *Quantum Communication, Measurement & Computing (QCMC'02)*, page 463. Rinton Press, 2002.

[40] S. Kirkpatrick, C. D. Gelatt, and M. P. Vecchi. Optimization by simulated annealing. *Science*, 220(4598):671–680, May 1983.

[41] Norio Konno. One-dimensional discrete-time quantum walks on random environments. *Quantum Information Processing*, 8(5):387–399, 2009.

[42] T. D. Ladd, F. Jelezko, R. Laflamme, Y. Nakamura, C. Monroe, and J. L. O/'Brien. Quantum computers. *Nature*, 464(7285):45–53, March 2010.

[43] David P. Landau. *A guide to Monte Carlo simulations in statistical physics*. Cambridge University Press, 2000.

[44] Pedro C. Lara, Renato Portugal, and Stefan Boettcher. Quantum walks on sierpinski gaskets. *Int. J. Quantum Inform.*, 11(08):1350069+, December 2013.

[45] Godfrey Leung, Paul Knott, Joe Bailey, and Viv Kendon. Coined quantum walks on percolation graphs. *New Journal of Physics*, 12(12):123018+, December 2010.

[46] Neil B. Lovett, Sally Cooper, Matthew Everitt, Matthew Trevers, and Viv Kendon. Universal quantum computation using the discrete-time quantum walk. *Physical Review A*, 81:042330+, April 2010.

[47] Yuri Manin. *Computable and Uncomputable*. Sovetskoye Radio, 1980.

[48] Lane Martin, Giovanni Di Giuseppe, Armando Perez-Leija, Robert Keil, Felix Dreisow, Matthias Heinrich, Stefan Nolte, Alexander Szameit, Ayman F. Abouraddy, Demetrios N. Christodoulides, and Bahaa E. A. Saleh. Anderson localization in optical

waveguide arrays with off-diagonal coupling disorder. *Opt. Express*, 19:13636–13646, 2011.

[49] R. Matjeschk, Ch Schneider, M. Enderlein, T. Huber, H. Schmitz, J. Glueckert, and T. Schaetz. Experimental simulation and limitations of quantum walks with trapped ions. *New Journal of Physics*, 14(3):035012+, March 2012.

[50] DavidA Meyer. From quantum cellular automata to quantum lattice gases. *Journal of Statistical Physics*, 85(5-6):551–574, December 1996.

[51] Christopher Moore and Alexander Russell. Quantum walks on the hypercube. In J. D. P. Rolim and S. Vadhan, editors, *Proc.˜6th Intl.˜Workshop on Randomization and Approximation Techniques in Computer Science (RANDOM '02)*, pages 164–178. Springer, 2002.

[52] J. A. Nelder and R. Mead. A simplex method for function minimization. *The Computer Journal*, 7(4):308–313, January 1965.

[53] A. Patel and K. S. Raghunathan. Search on a fractal lattice using a quantum random walk. *Phys. Rev. A*, 86:012332, 2012.

[54] Apoorva Patel, K. Raghunathan, and Pranaw Rungta. Quantum random walks do not need a coin toss. *Physical Review A*, 71(3):032347+, March 2005.

[55] Apoorva Patel and K. S. Raghunathan. Search on a fractal lattice using a quantum random walk. *Physical Review A*, 86:012332+, July 2012.

[56] Hagai B. Perets, Yoav Lahini, Francesca Pozzi, Marc Sorel, Roberto Morandotti, and Yaron Silberberg. Realization of quantum walks with negligible decoherence in waveguide lattices. *Phys. Rev. Lett.*, 100:170506, May 2008.

[57] M. Plischke and B. Bergersen. *Equilibrium Statistical Physics, 2nd edition.* World Scientifc, Singapore, 1994.

[58] Renato Portugal. *Quantum walks and search algorithms*. Springer, March 2013.

[59] R. Rammal and G. Toulouse. Random walks on fractal structures and percolation clusters. *Journal de Physique Lettres*, 44(1):13–22, 1983.

[60] Sidney Redner. *A guide to first-passage processes*. Cambridge University Press, 2001.

[61] L. Sansoni, F. Sciarrino, G. Vallone, P. Mataloni, A. Crespi, R. Ramponi, and R. Osellame. Two-particle bosonic-fermionic quantum walk via integrated photonics. *Phys. Rev. Lett.*, 108:010502, 2012.

[62] Tobias Schaetz, Chris R. Monroe, and Tilman Esslinger. Focus on quantum simulation. *New Journal of Physics*, 15(8):085009+, August 2013.

[63] Bart Selman, Henry Kautz, and Bram Cohen. Local search strategies for satisfiability testing. In *DIMACS Series in Discrete Mathematics and Theoretical Computer Science*, pages 521–532, 1995.

[64] Neil Shenvi, Julia Kempe, and K. Birgitta Whaley. A quantum random walk search algorithm. *Physical Review A*, 67(5):052307+, May 2003.

[65] P. W. Shor. Algorithms for quantum computation: discrete logarithms and factoring. In *Foundations of Computer Science, 1994 Proceedings., 35th Annual Symposium on*, volume 0, pages 124–134, Los Alamitos, CA, USA, November 1994. IEEE.

[66] Frederick Strauch. Connecting the discrete- and continuous-time quantum walks. *Physical Review A*, 74(3):030301+, September 2006.

[67] Steven H. Strogatz. *Nonlinear dynamics and chaos with applications to physics, biology, chemistry, and engineering*. Studies in nonlinearity. Westview Press, 1 edition, January 2000.

[68] Avatar Tulsi. Faster quantum-walk algorithm for the two-dimensional spatial search. *Physical Review A (Atomic, Molecular, and Optical Physics)*, 78(1):012310+, 2008.

[69] N. G. van Kampen. *Stochastic Processes in Physics and Chemistry*. Elsevier, 3 edition, May 2007.

[70] SalvadorElías Venegas-Andraca. Quantum walks: a comprehensive review. *Quantum Information Processing*, 11(5):1015–1106, July 2012.

[71] Rafael Vieira, Edgard P. M. Amorim, and Gustavo Rigolin. Dynamically disordered quantum walk as a maximal entanglement generator. *Physical Review Letters*, 111(18), October 2013.

[72] M. Štefaňák, I. Bezděková, and I. Jex. Continuous deformations of the grover walk preserving localization. *The European Physical Journal D*, 66(5):1–7, 2012.

[73] Kyohei Watabe, Naoki Kobayashi, Makoto Katori, and Norio Konno. Limit distributions of two-dimensional quantum walks. *Physical Review A*, 77(6), June 2008.

[74] Christof Weitenberg, Manuel Endres, Jacob F. Sherson, Marc Cheneau, Peter Schauss, Takeshi Fukuhara, Immanuel Bloch, and Stefan Kuhr. Single-spin addressing in an atomic mott insulator. *Nature*, 471:319–324, 2011.

[75] K. Zyczkowski and M. Kus. Random unitary matrices. *Journal of Physics A: Mathematical and General*, 27(12):4235+, June 1994.